Università degli Studi di Udine

Corso di Dottorato di Ricerca in Matematica e Fisica
ciclo XXVI

Tesi di Dottorato di Ricerca

Search for supersymmetric partners of the top quark in events with two leptons in the final state with the ATLAS experiment at the LHC

Candidato:
Simone Federico Brazzale

Relatore:
Prof.ssa Marina Cobal

Tutors:
Prof. Giovanni Pauletta
Prof. Lorenzo Santi

Anno Accademico 2013/2014

Dipartimento di Chimica Fisica e Ambiente
Università degli Studi di Udine
Via del Cotonificio, 108
33100 Udine
Italia

Abstract

The search for Supersymmetric extensions of the Standard Model (SUSY) remains a hot topic in high energy physics in the light of the discovery of the Higgs boson with mass of 125 GeV. Supersymmetric particles can cancel out the quadratically-divergent loop corrections to the Higgs boson mass and can explain presence of Dark Matter in the Universe. Moreover, SUSY can unify the gauge couplings of the Standard Model (SM) at high energy scales. Under certain theoretical assumptions, the supersymmetric partner of the top quark, i.e. the top squark, is preferred to be lighter than one TeV and its discovery can thus be accessible at the LHC.

This thesis describes a search for pair production of top squarks in final states with two leptons with the ATLAS experiment, using 4.7 fb^{-1} and 20.3 fb^{-1} of proton-proton collisions at a center of mass energy of 7 TeV and 8 TeV, respectively.

The case with 7 TeV data is optimized for a simplified SUSY model which considers the top squark decay mode $\tilde{t}_1 \to t\tilde{\chi}_1^0$ to happen in the 100% of the cases. No excess over the SM predictions has been observed and results of the search exclude a top squark mass of 300 GeV at 95% Confidence Level for a nearly massless neutralino.

The case with 8 TeV data is optimized for two decay modes: $\tilde{t}_1 \to b\tilde{\chi}_1^{\pm}$ and $\tilde{t}_1 \to bW\tilde{\chi}_1^0$. Exclusion limits are obtained in two-dimensional projections of the $(\tilde{t}_1, \tilde{\chi}_1^{\pm}, \tilde{\chi}_1^0)$ parameters space for the first mode, or in the $\tilde{t}_1 - \tilde{\chi}_1^0$ plane for the second mode. In the latter scenario, a top squark with mass of 240 GeV is excluded at 95% Confidence Level for $m(\tilde{\chi}_1^0) = 100$ GeV.

Introduction

The Standard Model (SM) is the theory which describes matter and fundamental interactions in the Universe. It has been so far a successful theory, continuously proved by experiments during the last decades and tested further with the discovery of the Higgs boson by the Large Hadron Collider (LHC) in July 2012. However the SM does not answer some problems which are left unsolved: why only 4% of the Universe is formed of matter? What is Dark Matter composed of? Do the fundamental forces match in a unique Grand Unification Theory at high energy scales?

Supersymmetry (SUSY) is one of the most known extension of the SM which has been postulated to solve some of the above questions. It is a generalization of the space-time symmetries of quantum field theory which transforms fermions into bosons and viceversa. It duplicates the SM spectrum by introducing superpartners of the SM particles, which thus differ by half a unit of spin. The Minimal Supersymmetric Standard Model (MSSM) is the minimal model that realizes SUSY. The MSSM has 105 free parameters, but it is possible to constrain the parameters space and give rise to simplified scenarios. For example, "natural" MSSM models require the superpartners of 3^{rd} generation quarks (squarks) to be relatively light (< 1 TeV) in order to explain the observed Higgs boson mass. Moreover, $R-$parity conservation forces the superpartners to be produced in pairs and the lightest supersymmetric particle (LSP) to be stable and neutral. This last could be a good candidate for Dark Matter (DM) and should explain a missing part of the Universe. If SUSY exists it is however broken at a certain energy scale, since no evidence of superpartners has been found so far.

The LHC, the biggest particle collider in the world, has been built to test the last pieces of the SM and to probe new physics beyond the SM, such as SUSY. It has been designed to reach energies well above the electroweak scale (10^2 GeV), with a maximum center of mass energy of 14 TeV in proton-proton (pp) collisions. With such high energies, hints of SUSY could be detected. LHC started up in November 2009 and worked remarkably well during Run I (2009-2013), although at sub-optimal configuration, breaking many new records.

At ATLAS, a general purpose experiment which collects data from the pp collisions delivered by the LHC, numerous searches for natural SUSY production have already been performed and the results led to several publications. In this framework, particular efforts have been devoted for searching direct pair production of third generation squarks, whose masses could lie below the TeV threshold.

The main part of this thesis presents a search for direct pair production of top squarks decaying in final states with two leptons, performed with the ATLAS experiment. The search utilizes 4.7 fb^{-1} of LHC collisions at 7 TeV and 20.3 fb^{-1} of LHC collisions at 8 TeV, collected by ATLAS in 2011 and 2012, respectively. For the 7 TeV case, the results are interpreted in a SUSY model in which each of the top squark

decays in a top quark and the lightest neutralino: $\tilde{t}_1 \to t\tilde{\chi}_1^0$. For the case with 8 TeV data, the results are interpreted in terms of two different decay modes: a top squark decaying into a $b-$quark and the lightest chargino ($\tilde{t}_1 \to b\tilde{\chi}_1^{\pm}$) and a scenario with a three-body decay to a $b-$quark, a W boson and the lightest neutralino ($\tilde{t}_1 \to bW\tilde{\chi}_1^0$). In both cases, results are used to constrain the parameters of the models, since no significant excess over the SM predictions have been observed.

It has to be said that hints of SUSY have not been detected by any of the LHC SUSY searches, at the time of writing. In particular natural SUSY is under pressure, although some corners of the phase space are not yet excluded. It is still soon, however, to infer any conclusion, and the scientific community is waiting the LHC Run II, which is expected to start in 2015 at almost maximum energy and luminosity, to drive any conclusion.

The rest of this thesis is organized as follows. Some details of the SUSY theory and the most important models are provided in Chapter 1. The ATLAS experiment and its performances are presented in Chapter 2. Chapter 3 introduces the general strategy of the search, while Chapters 4 and 5 illustrate the results of the cases with 7 TeV and 8 TeV, respectively, with a detailed descriptions of the techniques used for estimating the background.

A last comment has to be said regarding the content of this thesis. Although the search is the result of a collaboration among several italian institutes, included the University of Udine, this thesis emphasizes the parts of the analyses which I performed by my own or on which I cooperated. For the 7 TeV case, this includes the development of a strategy for the estimate of background arising from fake leptons, described in Chapter 4, which is an essential ingredient to the final results, and whose measurement depends on the event topology and the detector response. For the 8 TeV case, beside the fakes estimate, I also collaborated in the optimization of the event selections, in the estimate of the SM background sources, and in the interpretation of the results. All these parts are described in full details in Chapter 5.

A convention with $c = 1$ is used throughout this document, where c is the speed of light in vacuum.

Contents

1

The Standard Model and beyond

This Chapter gives an introduction to the Standard Model of Particle Physics, the theory which describes the constituents of matter and the forces which act in between them, and of Supersymmetry, the most known extension of the Standard Model which was developed to solve some open problems.

1.1 The Standard Model of Particle Physics

The Standard Model (SM) is the quantum-relativistic theory which describes all known matter components and three of the four forces determining the interactions among these fundamental constituents: the strong nuclear force, the electromagnetism and the weak nuclear force. The SM theory is based on a set of fields which describes elementary particles with half-integer spin (fermions) and on the gauge symmetry $SU(3) \times SU(2) \times U(1)$, revealing force-carrying particles with integer spin (bosons). The SM has allowed to predict and explain all the experimental results obtained in the field of Particle Physics in the last 60 years, culminated in the discovery of the Higgs boson, observed for the first time at the Large Hadron Collider (LHC) [1] on July 4, 2012 [2, 3]. It is thus considered a model of remarkable success, even if it is not able to include the gravitational force[1].

Fig. 1.1 illustrates the particle content of the SM, with all the fermions and gauge bosons, and their main properties. The fermions consist of six types of quarks and leptons, grouped in three families: $[(u, d), (c, s), (t, b)]$, and $[(e, \nu_e), (\mu, \nu_\mu), (\tau, \nu_\tau)]$, respectively. Similar particles with opposite charge, called anti-particles, are included in the model. The bosons consist of the photon, the electromagnetic force-carrier, the $W^{\pm}$ and Z bosons, that mediate the weak interaction, the gluons, which act as the exchange particles for the strong force between quarks, and the Higgs boson, which is responsible of the mechanism that gives mass to all particles.

According to Quantum Chromodynamics (QCD) [4,5], the gauge field theory based on the gauge group $SU(3)$ of $SU(3) \times SU(2) \times U(1)$, all of the quarks possess a color charge, which causes them to engage in the strong interaction. QCD manifests two peculiar properties. The first of these is "confinement", which forces the quarks to combine in states called hadrons consisting of either a quark and an antiquark (mesons) or three quarks (baryons). The combination process of quarks into hadrons is called hadronization. The second is "asymptotic freedom", which means that in very high-energy reactions quarks and gluons interact very weakly creating a quark-gluon plasma. Due to confinement, quarks cannot exist as free particles in nature. Therefore they

[1] Gravity however turns out to be negligible in the description of the subatomic world.

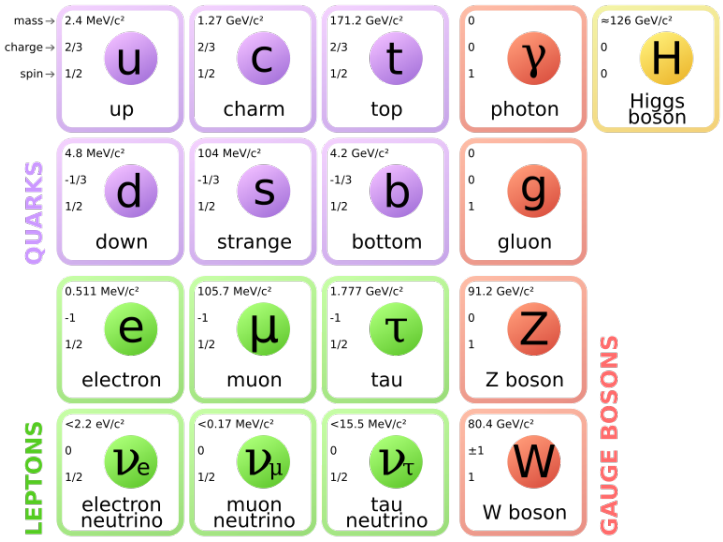

Figure 1.1: Standard Model of elementary particles: the 12 fundamental fermions and the bosons which carry the interactions. All the particle properties are under periodic reevaluation by the scientific community [6].

fragment into hadrons before they can be directly detected, resulting in collimated bursts of particles called jets. These jets must be measured in a particle detector and studied in order to determine the properties of the original quark. The top quark t is the most massive quark of the six and is, due to its huge mass, the only quark which decays before it has time to hadronize. It could be identified in particle detectors only by its decay products.

The SM of electromagnetic and weak interactions, developed by Glashow, Salam and Weinberg [7–10] is based on the gauge group $SU(2) \times U(1)$, with gauge bosons W^i_μ, $i = 1, 2, 3$ and B_μ for the $SU(2)$ and $U(1)$ factors, respectively, and the corresponding gauge coupling constants g and g'. The theory predicts that above the unification energy, of the order of 100 GeV, the two forces unify in a single electroweak (EW) interaction. In the EW theory, the fermion fields ψ are split up into left-handed (ψ_L) and right-handed (ψ_R) fields, arranged in doublets and singlets:

$$\begin{pmatrix} u \\ d \end{pmatrix}_L \begin{pmatrix} c \\ s \end{pmatrix}_L \begin{pmatrix} t \\ b \end{pmatrix}_L \quad \begin{matrix} u_R & c_R & t_R \\ d_R & d_R & b_R \end{matrix} \tag{1.1}$$

$$\begin{pmatrix} \nu_e \\ e \end{pmatrix}_L \begin{pmatrix} \nu_\mu \\ \mu \end{pmatrix}_L \begin{pmatrix} \nu_\tau \\ \tau \end{pmatrix}_L \quad e_R \quad \mu_R \quad \tau_R \ . \tag{1.2}$$

They include neutrinos (ν_i) and up-type quarks (u, c, t), which carry the weak isospin $T_3 = +\frac{1}{2}$, and charged leptons (e, μ, τ) and down-type quarks (d, s, b), with $T_3 = -\frac{1}{2}$. The weak interaction only couples to left-handed particles.

Most of the SM fermions and bosons have a mass, which has been measured in experiments, but the $SU(2) \times U(1)$ gauge group does not accommodate mass terms for fermions and bosons without violating the gauge invariance. A complex scalar Higgs doublet

$$\phi = \begin{pmatrix} \phi^+ \\ \phi^0 \end{pmatrix} \tag{1.3}$$

must be introduced to generate the masses through spontaneous electroweak symmetry breaking (EWSB) [11–13]. The $SU(2) \times U(1)$ symmetry is then broken into $U(1)_{QED}$, and the gauge bosons W^i_μ and B_μ interact with the Higgs doublet to give raise to two physical charged massive fields, $W^\pm$, and two neutral gauge bosons Z and γ, the last of which remains massless. Only one neutral Higgs scalar H, moreover, is left in the physical spectrum.

Once the gauge symmetries and the fields with their quantum numbers are specified, the Lagrangian of the SM can be defined by assembling different terms:

$$\mathcal{L}_{SM} = \mathcal{L}_{Gauge} + \mathcal{L}_{Matter} + \mathcal{L}_{Yukawa} + \mathcal{L}_{Higgs}. \tag{1.4}$$

The first piece contains the kinetic energy of the gauge fields and their self interactions, while the second piece contains the kinetic energy of the fermions and their interactions with the gauge fields. $\mathcal{L}_{Yukawa}$ is the Yukawa interaction of the Higgs field with the fermions. The last term is the Higgs Lagrangian, given by:

$$\mathcal{L}_{Higgs} = (D^\mu \phi)^\dagger D_\mu \phi + \mu^2 \phi^\dagger \phi - \lambda (\phi^\dagger \phi)^2, \tag{1.5}$$

where D_μ is the covariant derivative, ϕ is the Higgs field, λ is the Higgs self-coupling parameter and the sign of the quadratic term is chosen such that the Higgs field has a non-zero vacuum-expectation value $v = (\sqrt{2} G_F)^{-\frac{1}{2}} \approx 246$ GeV, fixed by the Fermi constant G_F. This last piece contains the kinetic energy of the Higgs field, its gauge interactions, and the Higgs potential. The Higgs boson mass is given by $m_H = \sqrt{\frac{\lambda}{2}} v$, but since λ is a free parameter of the theory, the value of m_H remains unpredictable.

1.2 History of the Standard Model

The first step towards the SM was placed in the 1960's by Glashow's discovery of a way to unify the electromagnetic and weak interactions. In 1967, Weinberg and Salam incorporated the Higgs mechanism which gives rise to the fermions and bosons masses into Glashow's EW theory. The theory of the strong interaction acquired its modern form only around 1973−74, upon experimental confirmation that the hadrons were composed of quarks.

The history of the Particle Physics era starts however earlier in the 1930's, when only the proton, electron and photon were known. In those years Dirac developed the "Quantum theory of the electron" [14], which predicted the existence of a particle with the same mass of the electron but with opposite charge (the positron). Some years later, Anderson observed for the first time the positron by means of a cloud chamber immersed in a magnetic field which curved the trajectory of charged particles [15]. Thanks to this discovery, Dirac was awarded with the Nobel prize in 1933 and Anderson in 1936. It was the beginning of the 20th-century explorations of Particle Physics.

Another important step was placed in 1934, when James Chadwick (Nobel in 1935) identified in laboratory a particle with a mass similar to that of the proton but with neutral charge: the neutron [16]. In the same years, Anderson and Neddermeyer identified another particle with a mass between the electron and the proton (the muon) [17].

The interplay between theory and experiments was however, at that time, rather weak. A theoretical work by Hideki Yukawa (Nobel in 1949) had predicted the existence of mesons as the carrier particles of the strong nuclear force already in 1935, but the first hints of the existence of quarks, in forms of the pion and kaon hadrons, were

observed only lately in 1947, by Lattes, Occhialini and Powell, in interactions produced by cosmic rays in cloud chambers with magnetic field [18].

Another example is the discovery of the neutrino: in the 30's Pauli had already theorized the existence of an elusive particle without mass and without electric charge, but it took more than 20 years, after the development of nuclear reactors, to observe a neutrino for the first time in laboratory [19].

After the second world war, however, the world of Particle Physics underwent an incredible evolution. From the experimental point of view, there was a rapid increase in the technological progress. The development of accelerators made possible the discovery of many new particles, included the anti-proton, discovered in 1955 [20], the electron− (1956) and muon−neutrinos (1963) [21], the $c-$ and $b-$quarks (1976) [22,23], the $W^{\pm}$ and Z bosons (1983) [24, 25] and the $t-$quark (1995) [26, 27].

Accelerators were needed mainly for two reasons. The first of these is a consequence of the wave-particle duality, which requires high energies to probe small distances and therefore to gain more detailed information on particle properties. The second reason is related to the Einstein's principle $E = mc^2$, which states that energy can be transformed into matter and viceversa. To reproduce massive particles in laboratory, therefore, high-energy accelerators were required to be built.

Two types of accelerators have mainly been used in those decades: fixed-target accelerators, in which a particle is accelerated against a fixed target in the laboratory frame, and colliders, in which two particles are accelerated against each other. Colliders can be sub-divided in linear and circular. In the former, particles are accelerated in straight paths by means of electric fields. In the latter, a magnetic field is added to deflect the path of the particles in order to generate circular orbits. The main advantage of having circular colliders is that, according to special relativity, the energy of an inelastic collision between two particles approaching each other with a given velocity can be orders of magnitude higher if the collision velocity approaches the speed of light, with respect to having one particle at rest. On the other hand, in a circular orbit the particles can travel many times the accelerator pipes before colliding, allowing to reach higher velocities and higher energies within smaller lengths.

Some of the main accelerators which have been used in the last decades are circular colliders: the Large Electron Positron collider (LEP), active in the years 1989-2000 at the CERN laboratory, Geneve, and which reached a maximum center of mass energy of 209 GeV, the proton-antiproton Tevatron collider, active in the years 1983-2011 at the Fermilab laboratory in Chicago, with a maximum center of mass energy of 1.96 TeV, and the operating LHC, developed in the last twenty years to reach a maximum center of mass energy of 14 TeV[2].

From the theoretical point of view, the latter half of the 20^{th} century gave also the chance to set-up and develop the SM as it is known today. The interplay and dialog between theory and experiments grew intensely. After the discovery of the neutrinos and the hadron resonances, the classification scheme based on $SU(3)$ was developed. Weak neutral currents, predicted in 1973 by Salam, Glashow and Weinberg, were confirmed shortly thereafter in 1974, in a neutrino experiment at CERN [28]. The current formulation of the SM, as already said, was then finalized in the mid-1970s after the experimental confirmation of the existence of quarks.

Before the LHC, however, there was a last missing piece to validate the SM theory: the observation of the Higgs boson.

[2]More details about the LHC are provided in Chapter 2.

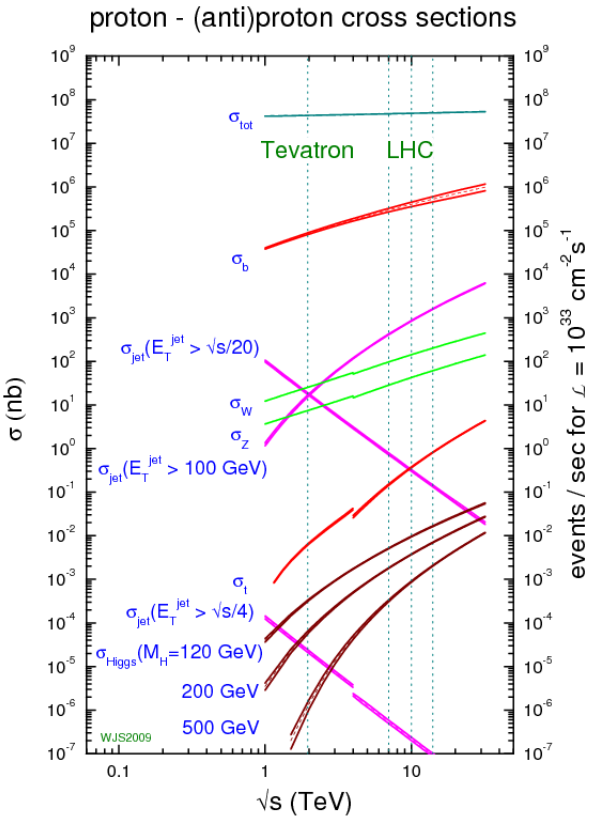

Figure 1.2: Production rates for SM processes at the Tevatron and LHC hadron colliders, as a function of the center of mass energy of the collision. The discontinuity is due to the Tevatron being a proton-antiproton collider while the LHC is a proton-proton collider. The two colliders working points correspond to a center of mass energy of around 2 TeV for the Tevatron and 7, 8 and 14 TeV for the LHC.

1.2.1 First observation of the Higgs boson at the LHC

The Higgs boson was searched for in many experiments since the last 30-40 years, and its observation has been one of the main targets of the LHC physics program, since its start in 2009. After more than two years of effort, in which the two LHC Collaborations ATLAS [29] and CMS [30] looked for the Higgs boson considering a variety of production processes and decay channels, its first observation was communicated to the public in July 2012.

At the LHC the dominant mechanisms for producing the Higgs boson, ordered by their production rate, are gluon fusion ($gg \to H$), vector boson fusion (qqH or $q\bar{q}H$), associated production with a vector boson (WH or ZH) and associated production with a top quark pair ($t\bar{t}H$). The production cross sections of these mechanisms are however order of magnitudes lower compared to the other main SM processes, as can be seen from Fig. 1.2. Fig. 1.3, on the other hand, shows the different impact of the Higgs decay branching ratios (BR) as a function of m_H. The dominant Higgs decay channels are $H \to b\bar{b}$, $H \to W^+W^-$, $H \to ZZ$ and $H \to \tau^+\tau^-$, and they have all been exhaustively covered by the two experiments. The decay mode $H \to ZZ \to l^+l^-l^+l^-$ played a crucial role in the discovery due to its clear signature with four leptons.

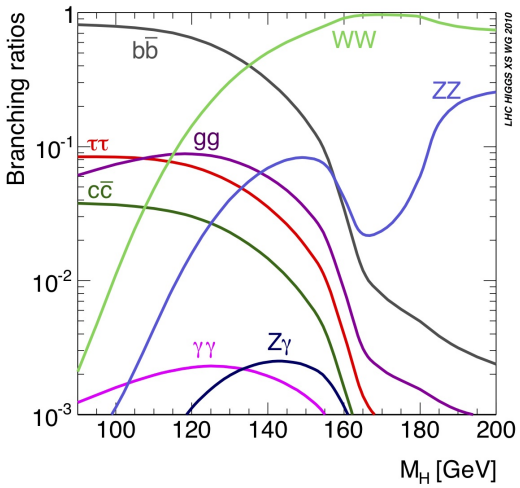

Figure 1.3: Branching ratios for the main decays of the SM Higgs boson, as a function of the Higgs boson mass m_H.

The decay to a pair of photons, induced at leading order by loop corrections, has lower cross section values, but the reconstructed mass resolution provided a good way to discriminate signal from background, and gave also a good chance for a precise measurement of m_H.

On July 4$^{\text{th}}$, 2012, ATLAS and CMS simultaneously announced the observation of a new particle consistent with the SM Higgs boson produced in the LHC pp collisions [2]. The data samples used corresponded to between 4.6 and 5.1 fb^{-1} of collision data at $\sqrt{s} = 7$ TeV in 2011 and $\sqrt{s} = 8$ TeV in 2012. The observed particle has been proved to be a boson and to decay to $\gamma\gamma$ and ZZ with rates consistent to those predicted for the Higgs boson in the SM. There were indications in the results that the observed particle also decayed to W^+W^-, $b\bar{b}$ and $\tau^+\tau^-$. Each experiment separately combined the data to obtain independent results of their searches and the combination was performed with a computation of the significance of the observation and a measurement of the production rate times the decay BR for each analyzed channel. The significance was measured by means of the $p-$value, which is the probability of observing a fluctuation of the background which gives a result at least as signal-like as that observed in the data. A $p-$value of 2.87×10^{-7} corresponds to a five standard deviation excess over the background predictions and determines a discovery. The $p-$values observed by ATLAS and CMS, as a function of the Higgs boson mass, are shown in Fig. 1.4. For the combination of the 7 TeV and 8 TeV data, ATLAS observed an excess with a local significance of 5.9 σ at a mass $m_H = 126.5$ GeV, with an expectation of 4.6 σ for a Higgs boson of such a mass. CMS observed an excess with a local significance of 4.9 σ at a mass 125.5 GeV, with an expected significance of 5.9 σ. Both ATLAS and CMS separately excluded the presence of a SM Higgs boson in a mass range outside the local excess.

Since July 2012, the ATLAS and CMS Collaborations have updated their results in the $H \to \gamma\gamma$, $H \to ZZ$, $H \to W^+W^-$, $H \to b\bar{b}$ and $H \to \tau^+\tau^-$ channels both using data collected at a center of mass energy of 7 and 8 TeV. The new results increased the $p-$value up to 7.0 σ [31, 32].

Less than two years after the announcement from ATLAS and CMS, the worldwide scientific community recognized the importance of this discovery and awarded the two physicists Peter Higgs and Francois Englert with the Nobel Prize in physics, "for the theoretical discovery of a mechanism that contributes to our understanding of the origin of mass of subatomic particles, and which recently was confirmed through the discovery of the predicted fundamental particle, by the ATLAS and CMS experiments at CERN's Large Hadron Collider" [33].

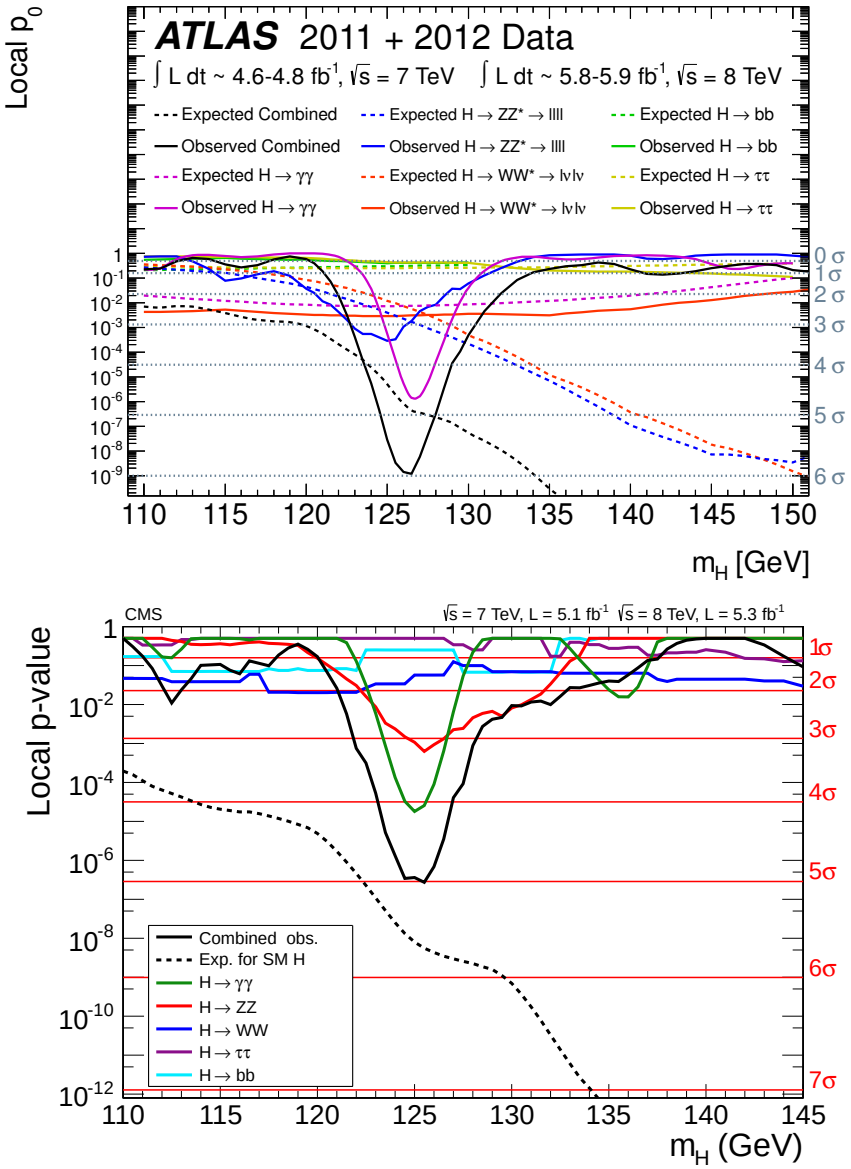

Figure 1.4: Local $p-$values of the ATLAS (top) and CMS (bottom) searches for the SM Higgs boson published in July 2012, reported separately for each decay mode. The solid lines show the observed $p-$values and the dashed lines show the median expected $p-$values, assuming a SM Higgs boson is present, computed for each m_H value [2, 3].

1.3 Physics beyond the Standard Model: SUSY and the MSSM

The SM, despite being a successful theory from the theoretical and experimental point of view, does not provide a full picture of nature. For example, it does not accommodate Gravity, which is 32 order of magnitude weaker than the weakest force described by the SM. This large deviation in the intensity of the forces is known as the hierarchy problem [34–36]. More technically, the hierarchy problem originates from the fact that all the scalar squared masses are quadratically sensitive to a possible new physics scale Λ (often taken to be the Planck scale $M_P \sim 10^{19}$ GeV), above which new physics enters to alter the behavior of the high-energy theory. For example, Fig. 1.5a shows a correction to the observable SM Higgs boson mass from a loop containing a Dirac fermion f with mass m_f. If the Higgs field couples to f with a term in the Lagrangian $-\lambda_f \bar{f} H f$, then from the Feynman diagram of the figure one gets a correction of the form:

$$\Delta m_H^2 = -\frac{|\lambda_f|^2}{8\pi^2}\Lambda^2 + .. \,, \tag{1.6}$$

where λ_f is the Yukawa coupling of the fermion. The problem is that if Λ is of order of M_P, unnatural cancellations must occur to remove the quadratic dependence of m_H to the new scale and to give the observed Higgs mass value. Moreover, also the masses of the quarks, leptons, and the EW gauge bosons of the SM are a function of m_H, thus the entire mass spectrum of the SM is sensitivie to the new physics scale Λ. The SM needs therefore to be enclosed in a more generic framework which stabilizes the hierarchy between the EW scale and the Planck scale in a more natural way.

Supersymmetry (SUSY) [37–45] is the most known extension of the SM that could explain the stability of the EW gauge hierarchy under quantum corrections. It is a generalization of the space-time symmetries of quantum field theory which transform fermions into bosons and viceversa. For each particle of the SM, it introduces supersymmetric partners (SUSY partners or superpartners) which differ by half unit of spin. SUSY is a promising theory which "naturally" solves the hierarchy problem. It cancels the quadratic divergences of the Higgs boson squared mass by means of the complex scalars S superpartners of the SM fermions, and which couple to the Higgs with a lagrangian term $-\lambda_S |H|^2 S^2$. In this case the Feynman diagram of Fig. 1.5b gives a contribution to the Higgs boson squared mass of the form:

$$\Delta m_H^2 = \frac{\lambda_S}{16\pi^2}[\Lambda^2 - 2m_S^2 \ln(\Lambda/m_S) + ..] \,, \tag{1.7}$$

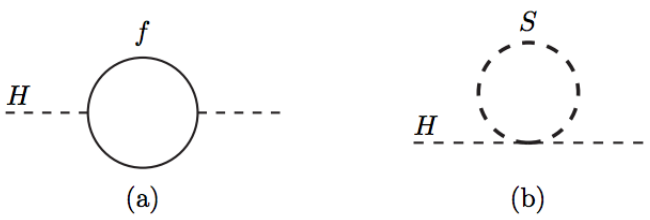

Figure 1.5: One-loop quantum corrections to the Higgs boson squared mass m_H^2, due to a fermion f (a) and a scalar S (b).

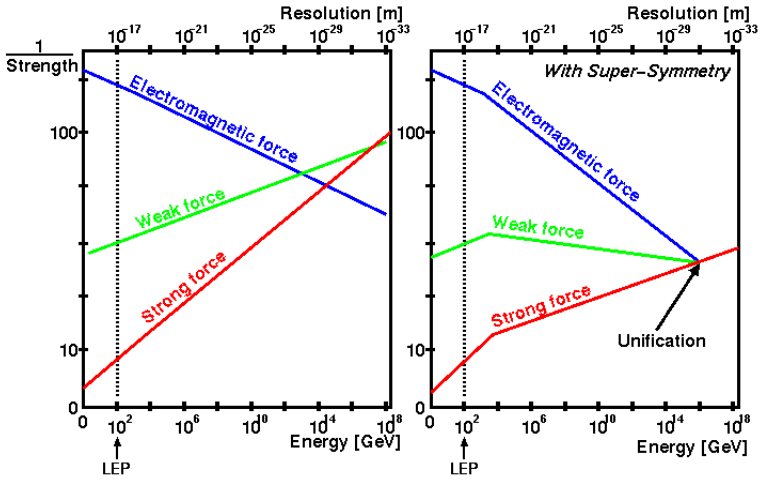

Figure 1.6: Illustration of the running of the three forces coupling constants as a function of the energy scale in the SM (left) and with the SUSY extension (right). In the latter case the three forces unifies at a certain energy scale.

where λ_S is the Yukawa coupling of the scalar S. If $\lambda_S = |\lambda_f|^2$, and one considers two scalar complex fields as superpartners of each SM fermion[3], than the new contribution proportional to Λ^2 cancels out the old contribution from the SM partner (equation 1.6), removing the quadratical divergence to the Higgs boson mass.

SUSY also provides unification of the three SM gauge couplings at high energy scales, modifying the running of the couplings above the EW scale [46], as shown in Fig. 1.6. Moreover, under certain theoretical conditions, the lightest supersymmetric particle (LSP) might be a promising candidate for Dark Matter (DM), whose interaction cross section is about that of the weak nuclear force [47]. The LSP, being a stable weakly-interacting massive particle (WIMP) that interacts through the weak force but not the electromagnetic force, could thus have the right relic density to make up the cosmic DM.

A first SUSY related theory in the context of Quantum Field Theory was proposed independently by three different groups: Golfand and Likhtman in 1971 [39], Gervais and Sakita, also in 1971 [42], and Volkov and Akulov in 1972 [43]. However, SUSY with a consistent Lie-algebric structure, on which the Gervais-Sakita theory was based, arose in the context of a development of an early version of String Theory, proposed by Ramond, Schwarz and Neveu in those years [40, 41]. After some other theoretical adjustments made by Wess and Zumino [44, 45], which also introduced early Particle Physics applications of the theory, the first realistic supersymmetric version of the Standard Model was proposed in 1981 by Georgi and Dimopoulos and is called the Minimal Supersymmetric Standard Model (MSSM) [35]. It was proposed to solve the hierarchy problem.

The MSSM contains a two-Higgs doublet model extension of the SM. The complete particle spectrum is illustrated in Table 1.1. The gauge super-multiplet consists of the gluons with their fermionic superpartners called gluinos, and of the $SU(2)\times U(1)$ gauge bosons with their gaugino SUSY partners. The matter sector includes three generations

[3]This introduces a factor of two in equation 1.7.

Super-multiplets	Boson fields	Fermionic partners
gluon/gluino	g	$\tilde{g}$
gauge/gaugino	$W^{\pm}$, W^0 B	$\tilde{W}^{\pm}$,$\tilde{W}^0$ $\tilde{B}$
slepton/lepton	$(\tilde{\nu}, \tilde{e}^-)_L$ $\tilde{e}_R^-$	$(\nu, e^-)_L$ e_R^-
squark/quark	$\left(\tilde{u}_L, \tilde{d}_L\right)$ $\tilde{u}_R$ $\tilde{d}_R$	$(u, d)_L$ u_R d_R
Higgs/higgsino	(H_d^0, H_d^-) (H_u^+, H_u^0)	$\left(\tilde{H}_d^0, \tilde{H}_d^-\right)$ $\left(\tilde{H}_u^+, \tilde{H}_u^0\right)$

Table 1.1: The particles and force carriers included in the MSSM. Only the first generation of quarks and leptons is listed. For each super-multiplet there is a corresponding anti-particle super-multiplet.

of left-handed and right-handed quarks and leptons with their superpartners, squarks and sleptons. All the corresponding antiparticle fields are also included in the model.

In the MSSM, two Higgs doublets H_u and H_d are needed to allow for EWSB and to provide mass to all quarks and leptons. After the spontaneous breaking of the EW symmetry, five physical Higgs particles are left in the spectrum: one charge Higgs pair, $H^{\pm}$, and three neutral states A, H and h.

The Lagrangian of the MSSM satisfies the $B - L$ conservation, where B is the Baryon number and L is the Lepton number. As a consequence, the MSSM manifests also a $R-$parity invariance, where $R = (-1)^{3(B-L)+2S}$, for a particle of spin S. The results of this is that all the SM particles have even $R-$parity, while SUSY particles have odd $R-$parity[4]. The conservation of $R-$parity has a crucial influence on the SUSY production phenomenology. First, starting from ordinary $R-$even particles it follows that SUSY particles must be produced in pairs. Second, the LSP results stable and must be produced at the end of a decay chain involving heavier unstable SUSY particles at the initial state. Being also a weakly interacting particle, the LSP behaves like a heavy neutrino and escapes the detector without being observed. This is a promising venue for detecting SUSY at colliders, with a signature involving large missing transverse momentum due to the escape of the LSPs.

1.3.1 MSSM parameters and particle spectrum

To describe the total number of independent physical parameters that define the MSSM, it is usually convenient to consider separately a supersymmetry-conserving

[4]There are SUSY models which consider $R-$parity violation, but those are not treated in this thesis.

sector and a supersymmetry-breaking sector, and to consider only the case of one generation of quarks, leptons, and their scalar partners.

According to [48], the parameters of the supersymmetry-conserving sector are: the SM gauge couplings g_s, g and g', a supersymmetry-conserving higgsino mass parameter μ and three Higgs-fermion Yukawa coupling constants λ_f ($f = 1, .., 3$), corresponding to the coupling of the Higgs bosons and higgsinos with one generation of quarks and leptons (u, d and e) and their superpartners.

The supersymmetry-breaking sector contains gaugino masses M_3, M_2 and M_1 (associated with the SU(3), SU(2) and SU(1) SM groups respectively), five scalar squared-masses $M^2_{\tilde{f}}$ ($\tilde{f} = 1, .., 5$) for the squarks and sleptons (corresponding to the five EW gauge multiplets) and three Higgs-squark-squark and Higgs-slepton-slepton trilinear interaction terms, called the "A-parameters" A_f.

Finally, there are two scalar squared-mass parameters m_1^2 and m_2^2 which contribute to the diagonal Higgs squared-masses, given by $m_1^2 + |\mu|^2$ and $m_2^2 + |\mu|^2$, and a third squared-mass parameter m_{12}^2 which contributes to the off-diagonal Higgs squared-mass term.

By introducing the variable $tan\beta = v_d/v_u$, where v_u and v_d are the vacuum expectation values of the neutral components of the Higgs field H_u and H_d respectively, the diagonal and off-diagonal Higgs squared-masses can be expressed in terms of m_Z, the angle β and the CP-odd Higgs mass m_A. In the MSSM $v_u^2 + v_d^2 \approx (246 \text{ GeV})^2$ but the single value of the two parameters is unpredicted, therefore $\tan\beta$ remains a free parameter of the theory.

In the case of three generations of quarks and leptons and superpartners, the parameters are 3×3 matrices. However, not all of the parameters are physical and some of them can be removed by expressing interaction eigenstates in terms of mass eigenstates. It is proven that the most generic form of the MSSM has 124 independent parameters: 18 of these comes from the SM, one corresponds to a Higgs sector parameter and 105 are new parameters of the model [49].

Physical mass eigenstates of the superpartners are formed by mixing the interaction states listed in Table 1.1.

The mixing of the charged gauginos ($\tilde{W}^{\pm}$) and charged higgsinos ($\tilde{H}_u^+$ and $\tilde{H}_d^-$) is described at tree level by a 2×2 complex mass matrix which depends on the three parameters μ, M_2 and $\tan\beta$ [50, 51]. In order to determine the physical masses, one diagonalizes the matrix and finds the physical chargino states denoted as $\tilde{\chi}_i^{\pm}, i = 1, 2$.

The mixing of neutral gauginos ($\tilde{B}$ and $\tilde{W}^0$) with neutral higgsinos ($\tilde{H}_d^0$ and $\tilde{H}_u^0$) is described by a 4×4 complex symmetric matrix, which depends on the four parameters M_1, M_2, μ and $\tan\beta$ [52–54]. After diagonalization one finds the physical neutralino states which are denoted by $\tilde{\chi}_i^0, i = 1, ..4$, where the states are ordered by their mass.

The generation of the mass eigenstates of the spin-0 superpartners of the fermions ($\tilde{f}_L$ and $\tilde{f}_R$) is a consequence of the $\tilde{f}_L - \tilde{f}_R$ mixing. In general, due to the presence of the quark masses in the off-diagonal elements of the mixing matrix, one expects the $\tilde{q}_L - \tilde{q}_R$ mixing to be small with the only exception of the third generation squarks, where the mixing is enhanced by the m_t and $m_b \tan\beta$ factors. For the top squark $\tilde{t}$, the mixing matrix is reduced to a 2×2 matrix. Diagonalizing the matrix gives two mass eigenstates $\tilde{t}_1$ and $\tilde{t}_2$, ordered by mass value [55–58].

Finally, the gluino is the fermion partner of the gluon and has mass $m(\tilde{g}) = |M_3|$.

It is important to notice that the assumptions on the parameters of the model can lead to different level of the mixing and therefore to different phenomenologies. Just

as an example, in a scenario where the $\tilde{\chi}_1^{\pm}$ is wino-like, the $\tilde{\chi}_1^0$ is a pure bino and the $\tilde{t}_1$ is mostly formed by the superpartner of the t_R, than one expects the $\tilde{t}_1 \to t\tilde{\chi}_1^0$ decay to dominate, in the condition $m(\tilde{t}_1) > m(t) + m(\tilde{\chi}_1^0)$, even if other modes are kinematically allowed. In the same condition, but if the $\tilde{t}_1$ is mostly formed by the $\tilde{t}_L$ component, the other decay mode $\tilde{t}_1 \to b\tilde{\chi}_1^{\pm}$ will instead prevail.

1.3.2 Constraining the MSSM parameters

It is possible to reduce the MSSM parameters, while still providing a suitable set consistent with phenomenological constraints. A generic approach is to impose a particular structure before symmetry breaking at a common high-energy scale M_X, typically chosen to be the Planck scale M_P ($\sim 10^{19}$ GeV) or the grand unification scale M_{GUT} ($\sim 10^{16}$ GeV). One can then derive the low-energy (EW scale) MSSM parameters through the renormalization group equations (RGEs). The initial conditions of these equations depend on the mechanism by which supersymmetry breaking is communicated to the low energy theory. For example, there are models with gaugino mass parameters which unifies at tree-level at some high-energy scale M_X:

$$M_1(M_X) = M_2(M_X) = M_3(M_X) = m_{1/2}. \tag{1.8}$$

In the Minimal Supergravity framework (mSUGRA) [59, 60], the SUSY-breaking parameters at high energy scale M_X take a simple form in which the scalar squared masses and the A-parameters are also universal:

$$\begin{gathered} M_{\tilde{f}}^2(M_X) = m_0^2, \\ m_1^2(M_X) = m_2^2(M_X) = m_0^2, \\ A_f(M_X) = A_0. \end{gathered} \tag{1.9}$$

RGEs are then used to derive the values of the supersymmetric partners at the EW scale. The low energy physical states thus depend primarily on m_0^2 and $m_{1/2}^2$. Typical mSUGRA models have $\tilde{b}_L$ and the diagonal masses $\tilde{t}_1$ and $\tilde{t}_2$ reduced with respect to the squark mass of the first two generations and the nearly mass-degenerate sleptons. Consequently, the LSP is typically the lightest neutralino $\tilde{\chi}_1^0$, which is pure-bino. The mSUGRA parameters reduce to the following set:

$$m_0, A_0, m_{1/2}, tan\beta, sgn(\mu). \tag{1.10}$$

With Gauge Mediated Supersymmetry Breaking (GMSB) [61–64], the supersymmetry breaking is communicated to the sector of MSSM fields via gauge interactions. In GMSB models the LSP is the gravitino and the next-to-LSP (NLSP) plays a crucial role in the phenomenology of supersymmetric particle production and decay. The $\tilde{\chi}_1^0$ and $\tilde{\tau}_R^{\pm}$ are the most likely candidates to be the NLSP. The NLSP will then decay to its superpartner and the gravitino ($\tilde{\chi}_1^0 \to \gamma\tilde{G}$, $\tilde{\chi}_1^0 \to Z\tilde{G}$ or $\tilde{\tau}_R^{\pm} \to \tau^{\pm}\tilde{G}$), with BR and lifetimes depending on the models.

Weak-scale "natural" SUSY is also motivated as a solution to the hierarchy problem. The naturalness paradigm is based on equations 1.6 and 1.7 and on the relation

$$m_Z^2 = -2(m_{H_u}^2 + |\mu|^2 + ..) \, . \tag{1.11}$$

It provides an explanation for the origin of the EWSB scale without the need of a significant fine-tuning of the fundamental MSSM parameters. Equation 1.11, in fact,

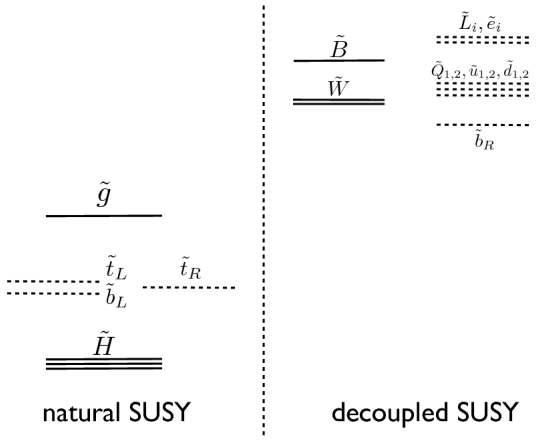

Figure 1.7: A possible natural SUSY spectrum.

imposes the Higgs squared mass and m_Z^2 to be roughly of the same order to avoid fine-tuning. m_H^2, on the other hand, receives from equation 1.6 a one-loop correction which depends on the Yukawa coupling of the fermion which couples to the Higgs. The most significant correction originates from the top quark, which is the heaviest quark and has $\lambda_t \approx 1$. The superpartner of the top quark then cancels out the quadratic divergent correction from the top quark, but the second term of equation 1.7 also imposes m_S not to be very large in order to give the observed Higgs boson mass. The paradigm thus constraints the top squark mass to be lighter than one TeV, and also the gluinos masses to be below a few TeV and the charginos and neutralinos masses to be below few hundreds GeV, since they are related together [65]. All other particles are decoupled and well above the TeV threshold. The precise limits on the superpartner masses are however driven by the amount of fine-tuning. Fig. 1.7 illustrates a possible natural SUSY spectrum of the interaction states, which then mix to form the physical states.

A Phenomenological MSSM (pMSSM) [66,67] has been also introduced to facilitate the exploration of MSSM phenomena in a more model-independent way. The pMSSM is governed by 19 independent real parameters beyond the SM, which include the three gaugino masses M_1, M_2 and M_3, the Higgs sector parameters m_A and $\tan\beta$, the Higgsino mass parameter μ, five squark and slepton squared-mass parameters for the degenerate first and second generations and the five corresponding squark and slepton squared-mass parameters for the third generation. There are finally three third-generation $A-$parameters (A_t, A_b and A_τ), since the first and second generation $A-$parameters can be neglected as their phenomenological consequences are negligible.

Another approach of constraining the MSSM can be found in the so-called simplified models [68–71]. A simplified model focuses narrowly on a specific generic production process and decay chain. It therefore depends on assumptions of the relative masses of the produced particles and decay products and the lack of interference from different processes. It is however advertised as the most model-independent approach for searching for SUSY. The results of the search discussed in this thesis, for example, are interpreted in the frame of simplified models considering a natural SUSY scenario.

1.4 SUSY searches and bounds on the MSSM

As of the time of writing, no signs of the superpartners have been observed. After the discovery of the Higgs particle in 2012, it was expected that SUSY particles would be found at the LHC collider at CERN, which produces the world highest energy collisions, but there has been still no evidence of them. Experiments at the LHC, moreover, made the first definitive observation of a B meson decaying into two muons, confirming a SM prediction and disfavoring SUSY [72, 73]. Although the scientific community is facing a critical situation, there is still the hope that the LHC Run II, planned to start in 2015 and to operate at higher energies with respect to what has been done so far, will give a chance to reveal SUSY. For the moment, LHC searches are constraining the MSSM parameters space.

The history of SUSY searches begins with the electron-positron collider LEP, which delivered up to 235 pb^{-1} of data with center of mass energies around 200 GeV, and its experiments were the firsts to set experimental bounds on the MSSM. Limits on the EW production of gauginos and leptons were placed in GMSB and mSUGRA models, with the most stringent constraint excluding masses of the lightest chargino up to 103.5 GeV [74, 75], except in corners of phase space with low electron sneutrino mass. In case of a small mass difference between $\tilde{\chi}_1^{\pm}$ and $\tilde{\chi}_1^0$, dedicated searches set a lower limit of 92 GeV. These limits remained competitive until the LHC era.

Significant constraints on SUSY have also been placed by the CDF [76, 77] and D0 [78, 79] experiments at the Tevatron. The two experiments collected an integrated luminosity between 10 and 11 fb^{-1} until the end of their physics program in 2011. At the Tevatron, interactions were obtained with higher energies with respect to those available at LEP, and QCD mediated processes were produced with large cross sections. This reflected in an increased sensitivity for color charged SUSY particles, such as squarks and gluinos. However, large backgrounds due to multijets production or production of top quarks and bosons in association with jets, challenged the extrapolation of the SUSY signals with respect to the SM background. The Tevatron experiments managed to place limits on squark and gluino masses assuming a constrained MSSM with $\tan(\beta) = 5$ (CDF) or $\tan(\beta) = 3$ (D0), $A_0 = 0$ and $\mu < 0$. Lower limits of about 310 GeV for all squark masses and 380 GeV for all gluino masses were set, with a limit of 390 GeV for the case $m(\tilde{q}) = m(\tilde{g})$ [80,81]. A recent CDF search with three isolated leptons also excluded a chargino mass below 168 GeV in a constrained MSSM scenario with $\tilde{\chi}_1^{\pm}\tilde{\chi}_2^0$ production, and assuming $m(\tilde{\chi}_1^{\pm}) = 2 \times m(\tilde{\chi}_1^0)$ in order to maximize the three-body leptonic chargino decay $\tilde{\chi}_1^{\pm} \to \tilde{\chi}_1^0 l^{\pm}\nu$ [82].

The program of SUSY searches, however, has significantly changed with the start of the LHC, which delivered around 5 fb^{-1} of pp collisions at $\sqrt{s} = 7$ TeV in 2011 and 20 fb^{-1} at $\sqrt{s} = 8$ TeV in 2012. The first analyses were focused on searches for processes with high cross sections, such as inclusive pair-production of gluinos and squarks. However, with the increasing integrated luminosity and the higher center of mass energy of the LHC with respect to the Tevatron, new rare processes became accessible and the community dedicated a huge effort to search for production of third generation squarks, also motivated by naturalness arguments. Since then, ATLAS and CMS searches have been optimized considering specific theoretical assumptions, and results have mostly been interpreted in terms of simplified models with SUSY-like topologies, where only one particular decay chain is considered. For some analyses, limits have also been set on the parameters of more generic models, such as mSUGRA/CMSSM

and GMSB. On the other hand, most of the analyses have been structured to cover as closely as possible generic $R-$parity conserving SUSY signatures, including jets, missing transverse energy due to the escape of the neutralinos, and eventually leptons.

Searches focused on pair-production of gluinos and squarks generally involve energetic jets, missing momentum and leptons in the final states. The results of most of these analyses have been interpreted by the ATLAS and CMS experiments by using simplified models with pair production of gluinos ($\tilde{g}\tilde{g}$) or squarks ($\tilde{q}\tilde{q}$) and with a neutralino LSP ($\tilde{\chi}_1^0$) at the end of the decay chain. All the squarks have been considered to carry the same mass in these models. Upper limits on SUSY production cross sections have then been derived as a function of the squarks and neutralino masses or gluino and neutralino masses. Results from these searches have also been interpreted in the constrained mSUGRA/CMSSM model, where the parameters of the model have been set to accommodate a lightest neutral scalar Higgs boson mass of 125 GeV. In the latter scenario, gluinos up to 1.35 TeV are excluded for light neutralinos and any squark masses [83, 84] by the ATLAS experiment, as can be seen from Fig. 1.8.

Other ATLAS searches for pair production of top squarks exclude $\tilde{t}_1$ masses below 680 GeV, considering simplified models with the stop decaying through $\tilde{t}_1 \to t\tilde{\chi}_1^0$ [85–87], or $\tilde{t}_1$ masses below 600 GeV considering a simplified model $\tilde{t}_1 \to b\tilde{\chi}_1^{\pm}$ [86, 88, 89].

Searches for EW production of SUSY particles have mostly been focused on direct production of charginos ($\tilde{\chi}_1^+\tilde{\chi}_1^-$) or production of charginos and next-to-lightest neutralino ($\tilde{\chi}_1^{\pm}\tilde{\chi}_2^0$). These two processes may dominate if squarks and gluinos masses are large. $\tilde{\chi}_1^{\pm}$ and $\tilde{\chi}_2^0$ can decay via sleptons ($\tilde{\chi}_1^{\pm} \to \tilde{l}\nu/l\tilde{\nu}$, $\tilde{\chi}_2^0 \to \tilde{l}l/\tilde{\nu}\nu$) or via bosons ($\tilde{\chi}_1^{\pm} \to W\tilde{\chi}_1^0, \tilde{\chi}_2^0 \to Z\tilde{\chi}_1^0$), depending on the region of the parameter space. Final states often include leptons, missing momentum and no jets. ATLAS has derived limits on the masses of the $\tilde{\chi}_1^{\pm}$ and $\tilde{\chi}_2^0$ and the neutralino LSP ($\tilde{\chi}_1^0$), assuming $m(\tilde{\chi}_1^{\pm}) = m(\tilde{\chi}_2^0)$, as shown from the red curve of Fig. 1.9. Chargino and heavy neutralino masses are excluded up to 600 GeV if these particles decay through sleptons and up to 315 GeV in cases where they decay via gauge bosons to a massless lightest neutralino [90].

In summary, no significant excesses over the SM predictions have been observed in all SUSY searches with the ATLAS and CMS experiments. The inclusive searches exclude gluinos with masses below 1.3 TeV at 95% Confidence Level (CL)[5] for the Higgs-aware mSUGRA/CMSSM model. Natural SUSY is also strongly constrained: top squark masses below 600-700 GeV are largely excluded by direct production searches, assuming 100% BR on different decays. Searches for EW production have shown sensitivity to decays via gauge bosons. The full ATLAS mass reach for SUSY is reported in Fig. 1.10, while that of CMS can be found in [91].

[5] A 95% CL means that there is a probability of at least 95% that the result is reliable.

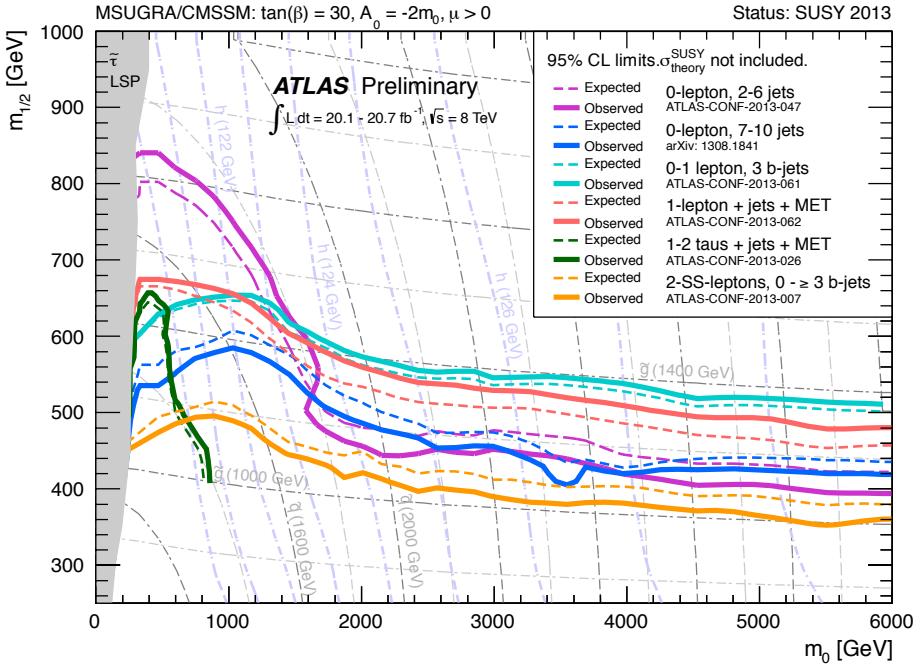

Figure 1.8: Exclusion limits at 95% CL on the m_0 and $m_{1/2}$ parameters of a Higgs aware mSUGRA/CMSSM model from ATLAS inclusive searches for squarks and gluinos [92].

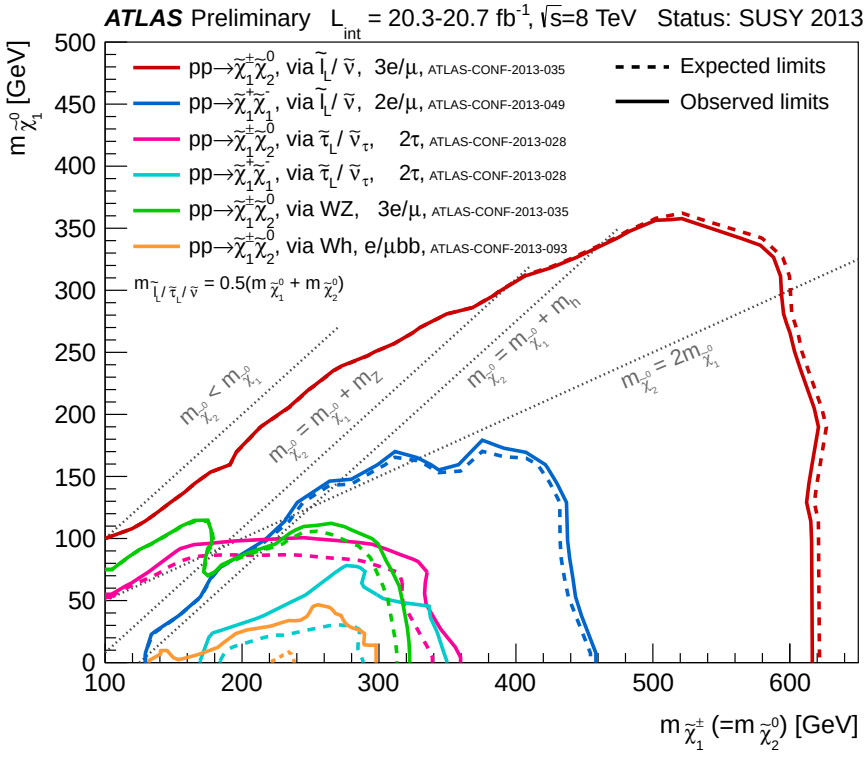

Figure 1.9: Exclusions limits at 95% CL in the chargino-neutralinos mass plane from EW SUSY production [92].

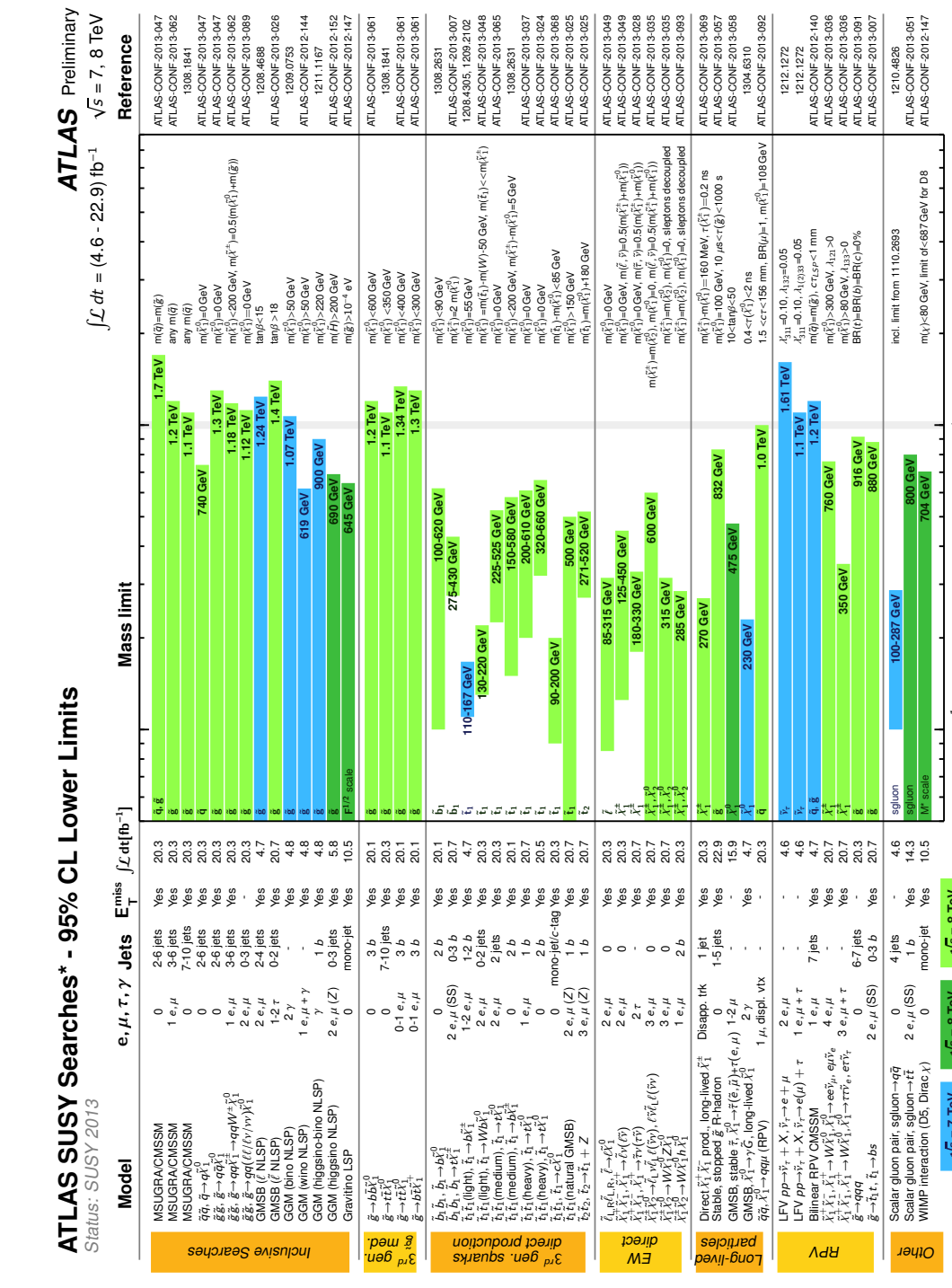

Figure 1.10: Mass reach of ATLAS searches for Supersymmetry [92].

2

CERN, LHC and the ATLAS experiment

This Chapter gives an overview of the CERN laboratory, of the proton-proton LHC collider and of the ATLAS experiment. The LHC is designed to collide proton beams at a maximum center of mass energy of 14 TeV. The particles produced from these collisions are then identified and measured in the ATLAS experiment, which allows to reconstruct and study the initial collision process and the final state produced.

2.1 The CERN laboratory

CERN ("European Organization for Nuclear Research" or "Conseil Europen pour la Recherche Nuclaire" in french) is the largest Particle Physics laboratory in the world. It is situated on the borderline between Switzerland and France, near the city of Geneve, and was established in 1954 by 12 member states. It has now 21 member states, included some non-european countries. The main goal of the CERN laboratory is to provide to the scientific community instruments and facilities in order to support studies in high energy physics. These include high-energy accelerators, which started to be requested from the second half of the 20th-century in order to probe the first pieces of the Standard Model, as discussed in Chapter 1.

The first hadron collider at CERN was the Intersecting Storage Rings, which collided protons at a center of mass energy of about 63 GeV. The energy reached by the collider was however not sufficient to produce real W and Z bosons in the collision. Therefore, the Super Proton Shyncroton (SPS), a circular accelerator with a circumference of 6.9 km, was used to accelerate proton and antiprotons bunches in the same ring. The SPS collider began running in 1981 with a center of mass energy of 540 GeV, and in the following two years it allowed to discover the W and Z bosons.

The main CERN project before the LHC was however the electron-positron accelerator LEP. It was constructed in a circular tunnel with a circumference of 27 km, at about 100 meters underground, in order to accelerate electrons up to the energy of 100 GeV, which means almost at the speed of light. It was used from 1989 until 2000, when it was dismantled to make way for the LHC. The most important LEP results have been: establishing the properties of the Z and W bosons, proving the existence of only 3 types of neutrinos and measuring indirectly the top quark mass, before top quarks were established at the Tevatron and their mass confirmed by direct observation[1] [93].

[1] Although the LEP center of mass energy was not sufficient to produce a top quark in the collisions, its existence was predicted from Z decays to b-quark jets and its mass was measured by means of

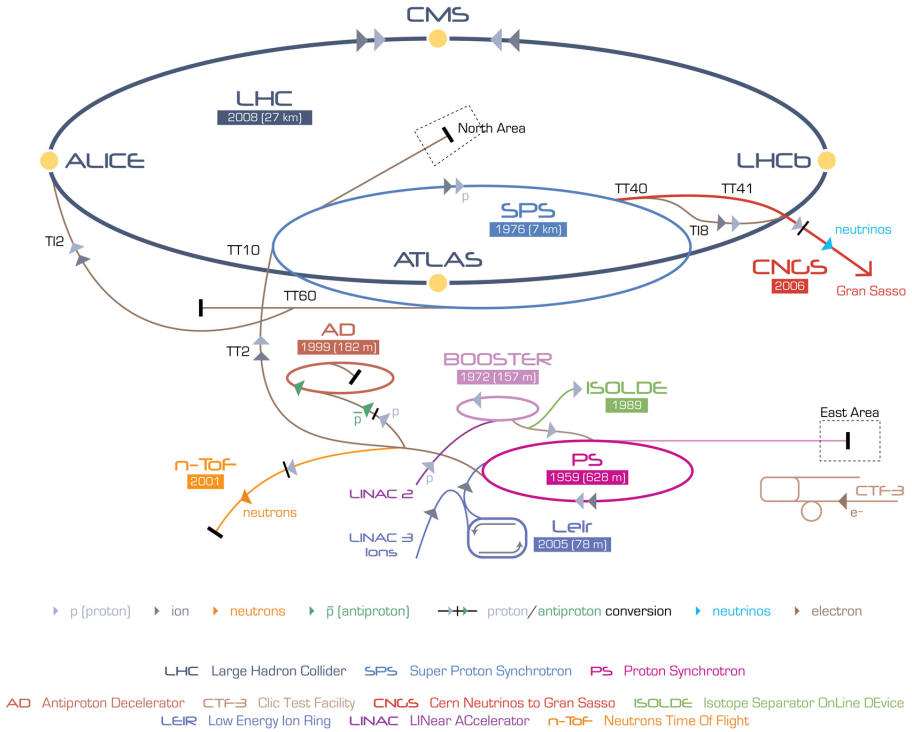

Figure 2.1: The CERN accelerators complex.

2.2 The Large Hadron Collider

The LHC is now the biggest and most powerful particle accelerator around the world. It has been built at CERN to collide protons at a maximum center of mass energy of 14 TeV, and started functioning in November 2009, after more than 20 years of construction and commissioning.

The LHC inherited the 27 km circumference tunnel from the LEP. In the tunnel two vacuum pipes have been built in order to accelerate bunches of protons through a magnetic field up to almost the speed of light. The two beams run in opposite directions in their own vacuum pipe and at a specific moment they collide in one of the four interaction points.

At CERN the LHC receives the protons from a complex of accelerators, as shown in Fig. 2.1. Protons are first injected in a linear accelerator (LINAC2) up to 50 MeV, then they are introduced via the Proton Synchrotron Booster (PSB) into the first circular accelerator, the Proton Synchrotron (PS) which rises the beam energy to 26 GeV. Finally they pass to the Super Proton Synchrotron (SPS), where they reach the energy of 450 GeV. Only at this point, they are sent to the LHC ring to reach 7 TeV of energy. The choice to collide protons instead of electrons, as it was the case for LEP, depends on the fact that protons are easier to keep in a circular orbit with respect to electrons[2], and if collided they can give rise to a wider spectra of reactions and

theoretical high-precision calculations at the quantum level of the SM.

[2]A charged particle radiates through synchrotron radiation with a power proportional to $e^2\gamma^4$, where γ is the Lorentz factor and e the charge of the electron. At the same energy, the Lorentz factor of a proton is lower than that one of an electron and so the power radiated.

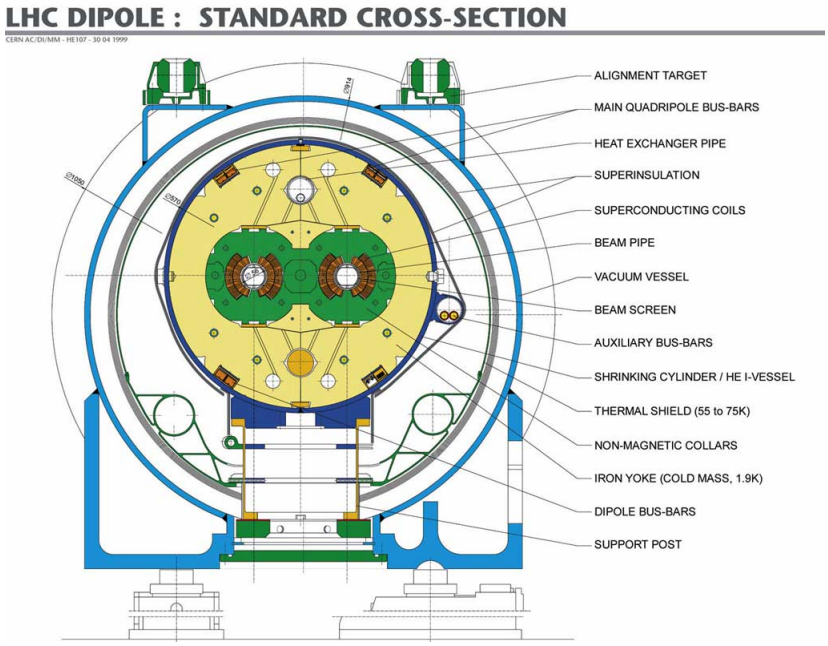

Figure 2.2: Transverse scheme of a LHC dipole, with the vacuum pipe.

energies. The choice to collide protons instead of antiprotons, as for the Tevatron in Chicago, is mainly due to the fact that is more difficult to collect antiprotons to reach the luminosities for which the LHC has been built[3].

Fig. 2.2 shows a transverse section of the LHC. The vacuum beam pipes are positioned in the middle of the section at the same high, and they are surrounded by two superconducting strips which create the vertical magnet field in the beam pipes. The two vacuum pipes are needed in order to run simultaneously two different beams of protons (for a particle-antiparticle accelerator only one pipe was necessary).

The luminosity $\mathcal{L}$ of an accelerator is defined by the relation $R = \mathcal{L} \cdot \sigma$, where R is the rate or frequency of events and σ is the cross section of the process. The luminosity is connected to the machine parameters through the following relation:

$$\mathcal{L} = \frac{n_p^2 f k}{4\pi\rho^2}, \tag{2.1}$$

where k is the number of proton bunches which run simultaneously in the beam pipe, n_p is the number of protons inside a single bunch, f is the bunches revolution frequency and ρ is the average squared radius of the proton spatial distribution along the plane perpendicular to the beam direction.

LHC has been designed to reach a maximum instantaneous luminosity value of $\mathcal{L} = 10^{34} cm^{-2} s^{-1}$ for a center of mass energy $\sqrt{s} = 14$ TeV in pp collisions. Each

[3]At the Tevatron, physics processes primarily generated by $q\bar{q}$ annihilation, such as $t\bar{t}$ and W/Z productions, benefitted from a slightly higher production rate with respect to the LHC due to the presence of valence antiquarks in the antiproton. At the energies of the LHC, however, productions of top quark pairs (as well as Higgs bosons, which is the main reason why the LHC has been built) are dominated by gluon-gluon fusion, which originate from the sea, and therefore there is no gain in using antiprotons.

bunch should contain 10^{11} protons at the moment of the injection and the bunches should be separated every 7.5 meters with a design bunch spacing of 25 ns. The design number of bunches for LHC is 2808. These bunches circumnavigate the ring at nearly the speed of light, traversing the entire ring about 10^4 times per second, and then collide in the interaction points. Not all the collisions are of interest since the majority of them are soft and the partons inside the protons do not interact with each other. Only the inelastic scatterings give rise to particles at sufficient high angles with respect to the beam axis. If considering a center of mass energy $\sqrt{s} = 14$ TeV, than the pp inelastic cross section is estimated to be around 70 mb, and the rate of interaction should be $R = 70 \cdot 10^{-3} \cdot 10^{-24} \cdot 10^{34} \simeq 700$ million collisions per second. The bunches cross at a design rate of 40 MHz, thus one obtains around 25 superimposed inelastic events per crossing (pile-up effect). The particles are kept circulating in the ring and maintained inside the beam pipe, where a vacuum pressure of 10^{-13} atm is reached, thanks to a magnetic field of around 8 T for pp collisions at 14 TeV. This field is generated thanks to superconducting dipole electromagnets operating at a temperature of 1.9 K. In total there are 1232 dipoles, 15 meters long and with a weight of 35 tons, in the LHC ring, cooled by 120 tons of helium. To keep the particles squeezed together in the beam pipe and close to the interaction point, 392 quadrupoles are used.

Despite the planned performances, in Run I (2009-2013) LHC has worked in a non-optimal configuration, reaching a maximum center of mass energy of $\sqrt{s} = 7$ TeV in 2011 and $\sqrt{s} = 8$ TeV in 2012.

At the collision points, four experiments have been built: ATLAS, CMS, LHCb [95] and ALICE [96]. ATLAS and CMS are multi-purpose experiments, designed to study high transverse momentum events for the search of the Higgs boson and other new physics phenomena. LHCb has been designed especially to study $b-$physics, while ALICE studies the formation of a quark-gluon plasma in heavy ion collisions (LHC can collide not only beams of protons but also heavy ions beams).

Figures 2.3 and 2.4 show the integrated and peak luminosity registered by the four

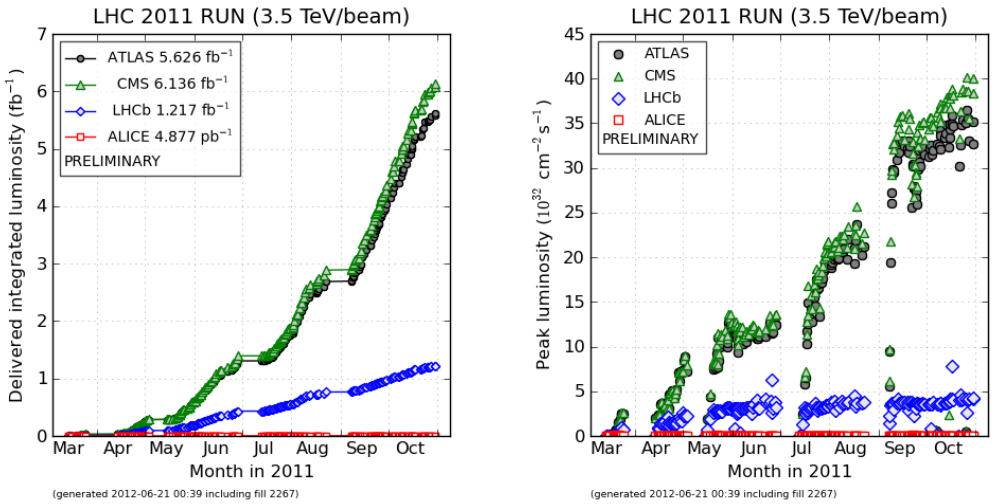

Figure 2.3: Integrated (left) and peak (right) luminosity registered by the four LHC experiments as a function of the $\sqrt{s} = 7$ TeV collision data taking day in 2011 [94].

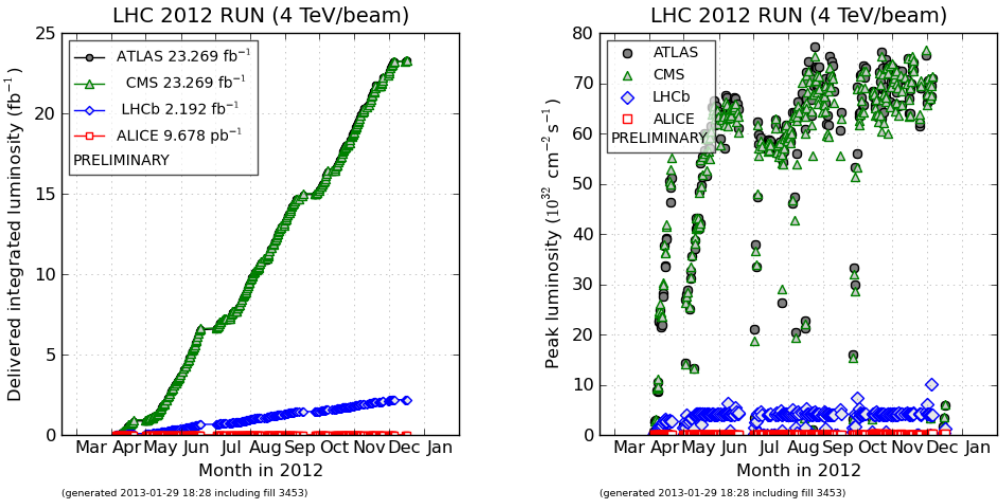

Figure 2.4: Integrated (left) and peak (right) luminosity registered by the four LHC experiments as a function of the $\sqrt{s} = 8$ TeV collision data taking day in 2012 [98].

experiments during the years 2011 and 2012, respectively. As can be seen from the figures, ATLAS accumulated an integrated luminosity of 5.6 fb^{-1} of $\sqrt{s} = 7$ TeV pp collisions, in the year 2011, and 23.3 fb^{-1} of $\sqrt{s} = 8$ pp collisions, at the end of the year 2012. LHC reached its maximum instantaneous luminosity in August 2012, with a value around 8×10^{33}cm^{-2}s^{-1}, and ended its first run in December 2012 with a bunch spacing of 25 ns rather than the 50 ns previously used.

At the beginning of 2013, the LHC collided protons with lead ions and then went into a long maintenance stop which will last until the end of 2014. Run II will resume in 2015, with an increased collision energy around 13 TeV, and with an additional increment foreseen in the luminosity [97].

2.3 The ATLAS experiment

ATLAS (A Toroidal LHC ApparatuS) is one of the four detectors operating at the LHC. It is a general purpose experiment, built with the goal of confirming the existence of the Higgs boson, discovering supersymmetric particles and in general studying all possible new physics beyond the SM. It is also a good experiment for SM precision measurements. ATLAS has been designed to make accurate measurements of electrons, photons, muons, hadronic jets (included jets from $b-$quarks, which are important for many known processes) and the possible missing momentum which results from the collision.

ATLAS is composed of different subdetectors, disposed as several concentric cylinders, as shown in Fig. 2.5. They are here described using a right-handed coordinate system where the interaction point in the centre of the detector (IP) is the origin, and the z-axis is oriented along the beam direction. The x-axis points from the IP to the centre of the LHC ring, and the y-axis points upwards. Cylindrical coordinates (r,ϕ) are used in the transverse plane, ϕ being the azimuthal angle around the beam direction. The pseudorapidity η is defined in terms of the polar angle θ as:

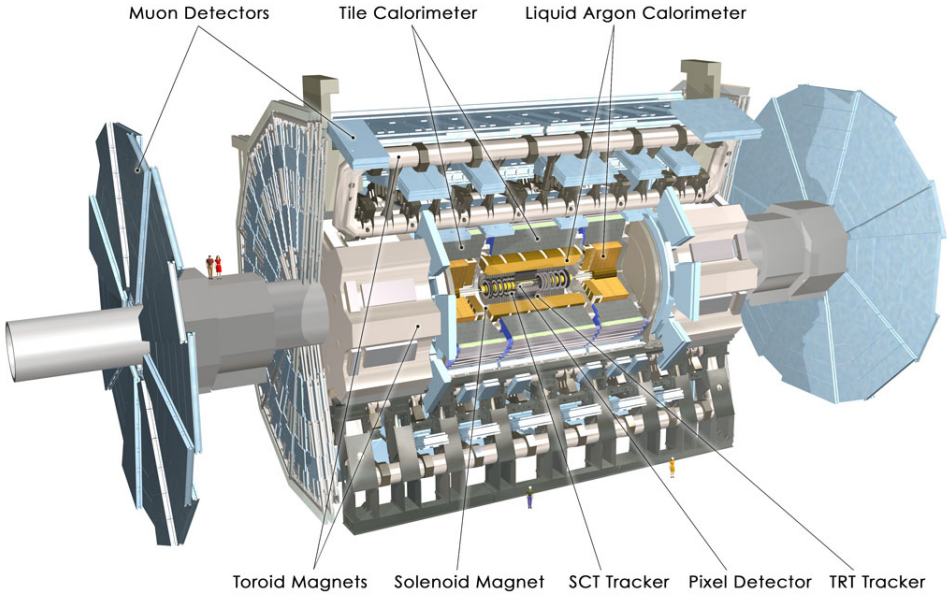

Figure 2.5: A schematic overview of the ATLAS experiment and its sub-detector.

$$\eta = -\ln(\tan\frac{\theta}{2}). \tag{2.2}$$

and the ΔR distance is defined as $\Delta R = \sqrt{\Delta\eta^2 + \Delta\phi^2}$ in the η-ϕ plane.

The ATLAS inner layer is the tracker, called Inner Detector (ID), embedded in a solenoidal magnetic field. The ID is formed itself of three sub-components: the Pixel Detector, the SCT Tracker and the TRT Tracker. Its main goal is to reconstruct the tracks of charged particles. Outside the inner tracker there is a section which measures the energy of electrons, photons and hadronic jets thanks to their interactions with the material contained inside an ElectroMagnetic Calorimeter (EM Calorimeter) and an HADronic Calorimeter (HAD Calorimeter). The outest layer of the detector is devoted to the identification and measurement of muons. The ATLAS experiment is 45 m high in total, has a 22 m diameter and weights 7000 tons.

The expected performances of the components, studied during commissioning phase and based on simulations of the detector and physics processes, are shown in Table 2.1.

ATLAS component	**Expected Resolution**	**η coverage**
Tracking	$\sigma_{p_T}/p_T \approx 0.05\% p_T \oplus 1\%$	$\lvert\eta\rvert < 2.5$
EM Cal. barrel	$\sigma_E/E \approx 10\%/\sqrt{E} \oplus 0.7\%$	$\lvert\eta\rvert < 1.4$
end-cap	$\sigma_E/E \approx 15\%/\sqrt{E} \oplus 0.7\%$	$1.4 < \lvert\eta\rvert < 3.2$
HAD Cal. barrel	$\sigma_E/E \approx 65\%/\sqrt{E} \oplus 3\%$	$\lvert\eta\rvert < 1.7$
end-cap	$\sigma_E/E \approx 110\%/\sqrt{E} \oplus 1\%$	$1.7 < \lvert\eta\rvert < 3.2$
Muon spectrometer	$\sigma_{p_T}/p_T < 4\%$, $10 < p_T < 500$ GeV $\sigma_{p_T}/p_T < 10\%$, $p_T = 1$ TeV	$\lvert\eta\rvert < 2.7$

Table 2.1: Expected ATLAS detector performances and coverage [99].

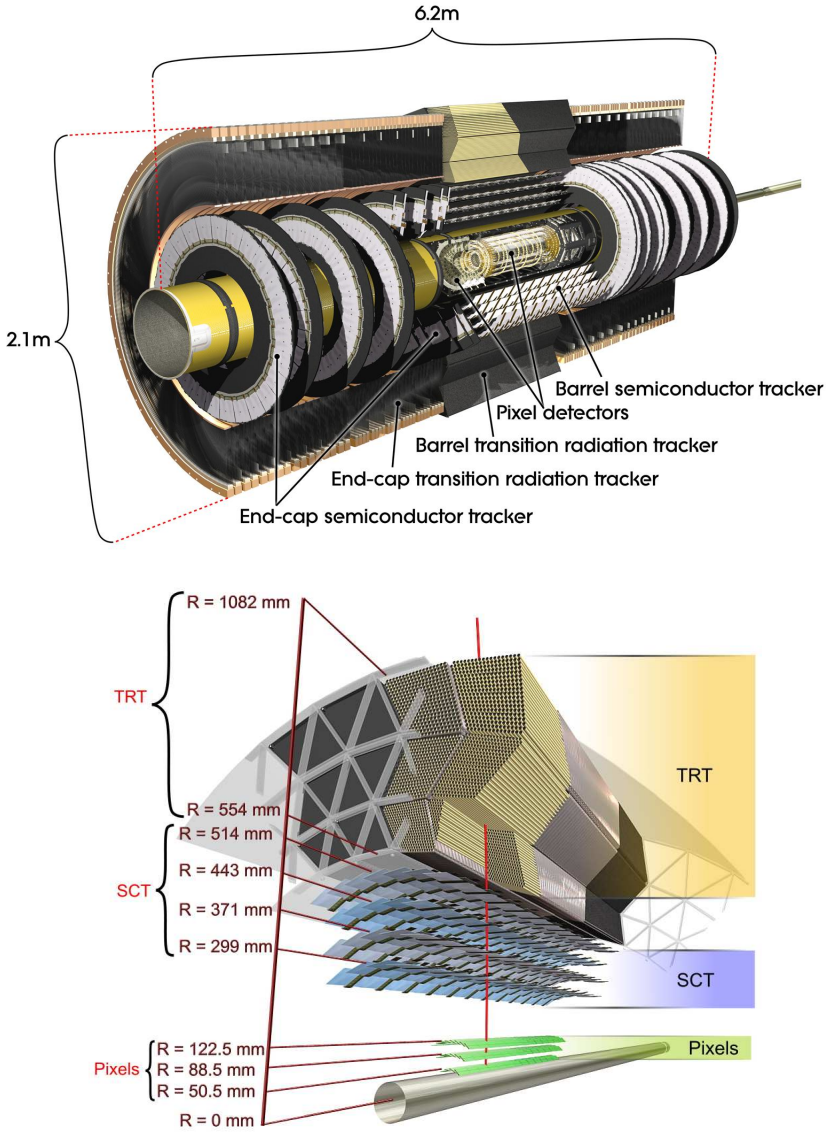

Figure 2.6: Top: schematic view of the Inner Detector with its sub-detectors and the barrel and end-caps components. Bottom: section view of the Pixel Detector, and of the SCT and TRT trackers perpendicular to the beam axis.

2.3.1 Inner Detector

The ID [100] measures with high precision the tracks of those charged particles which originate from the collision, up to $|\eta| = 2.5$, using the minimum possible material to avoid multiple scattering[4]. It is a cylinder of 115 cm radius and 7 m length, embedded in a 2 T magnetic field (see Fig. 2.6), with a volume delimited by the EM calorimeter and the cryostat of the solenoidal magnets.

To obtain a precise measurement of the particle track and at the same time avoid multiple interactions, the ID is formed of three layers constructed using different tech-

[4]Multiple scattering happens when the particles originated in the collision travel through the detector and interact with its material.

nologies. In the inner part, the first 60 cm closest to the interaction vertex, there is a Pixel Detector which provides a very high resolution and granularity, but counting for a limited distance. In the outer layers, there are two heavier trackers (SCT and TRT Trackers) which give more information for the track reconstruction, but have less precision. The combination of the information from the Pixel and the SCT trackers, in conjunction with the TRT, offers high precision measurements made to achieve the momentum and vertex resolution requirements imposed by the physics program, with fine detector granularity. To provide also a wide covering in the η plane, the outer detectors are disposed both in concentric cylinders around the beam axis (barrel) and in discs perpendicular to the beam direction (end-caps).

Pixel Detector

The Pixel Detector is formed of layers of modules containing pixel sensors disposed into a lattice-type structure. It is the sub-detector closest to the collision point, built around the beam pipe, and thus provides the best resolution for primary and secondary vertex reconstruction. There are three barrel layers (located at 50.5 mm, 85.5 mm and 122.5 mm from the beam axis) consisting of 1456 rectangular modules and two end-caps made of three disks each containing a total of 288 modules. Each 250 μm thick module is made of 50 μm wide and 400 μm long silicon pixels, for a total of 47232 pixels per module. The total number of readout channels in the Pixel Detector is of around 80×10^6.

The charged particles produced in the collisions interact with these layers of material and a precise measurement of their paths is made by the detector. The optimal resolution is achieved for tracks with $|\eta| < 2.5$ and for any value of ϕ. The detector operates at a temperature of $-20°$C to reduce radiation damage and integrates a cooling system. The Pixel Detector has been designed to withstand over 300 kGy of ionizing radiation over ten years of operation.

SCT Tracker

The SCT Tracker (SemiConductor Tracker) is a silicon microstrip tracker consisting of modules of silicon detector strips. It is composed of four cylinders in the barrel region covering the $|\eta|$ range $1.1 < |\eta| < 1.4$ and disposed between 299 mm and 514 mm from the beam axis, and two end-caps made of nine disks covering the pseudorapidity range $1.1 - 1.4 < |\eta| < 2.5$ and with radii extending to 56 cm. It usually provides four space-points measurements (eight strips) for particles originating at the interaction vertex. The strips are disposed in such a way to give the coordinates of the impact point and to guarantee a high granularity, with a constant pitch of 80 μm. They consist of 61 m^2 of silicon sensors with 6.3 millions readout channels.

The SCT tracker has been designed to ensure an efficiency greater than 99%. After the first run, the barrels had an average efficiency of 99.9% over all layers and the end-caps hit efficiency was around 99.8%. The detector is cooled down at a temperature of $-7°$C by the cooling system.

TRT Tracker

The TRT Tracker (Transition Radiation Tracker) is made up of layers of drift tubes. The volume of the tracker covers radial distances from 563 mm to 1066 mm from the

beam axis. The 4 mm diameter drift tubes are made of straw tubes and reinforced with thin carbon fibers. Inside each tube there is a gold-plated tungsten wire of 31 μm diameter. The tubes are then filled with a gas mixture of Xe, CO_2 and O_2. Each tube acts as a small proportional chamber: when a charged particle passes through the TRT, it ionizes the gas and generates free electrons which drift towards the wire where they are amplified and read out. The front-end electronics then sample the incoming signal and compare it with a default threshold to identify the particle.

The TRT region consists of 52544 straw tubes of 1.5 m length, which are parallel to the beam axis. The tubes are arranged in three cylindrical layers and 32 sectors in ϕ. The η coverage is $|\eta| < 1$. The end-caps instead contain straw tubes disposed perpendicular to the beam axis, each side consisting of 122880 straws and covering the pseudorapidity range $1 < |\eta| < 2$.

The TRT is complementary to the SCT tracker: the single-point resolution is larger (120 μm) but has a higher number of hits per tracks which is typically more than 30. It has been designed especially for the identification of electrons by means of the X-rays emitted by the particles when they are passing through the detector and which are captured in the tubes.

2.3.2 Calorimeters

The ATLAS calorimeters have been designed to work at high luminosities for at least ten years, and therefore to be quite radiation resistant. They have been also designed to study a wide spectra of physics processes in the physics program.

ATLAS is composed of two different calorimeters: the EM Calorimeter and the HAD Calorimeter, disposed one inside the other as concentric cylinders, as illustrated

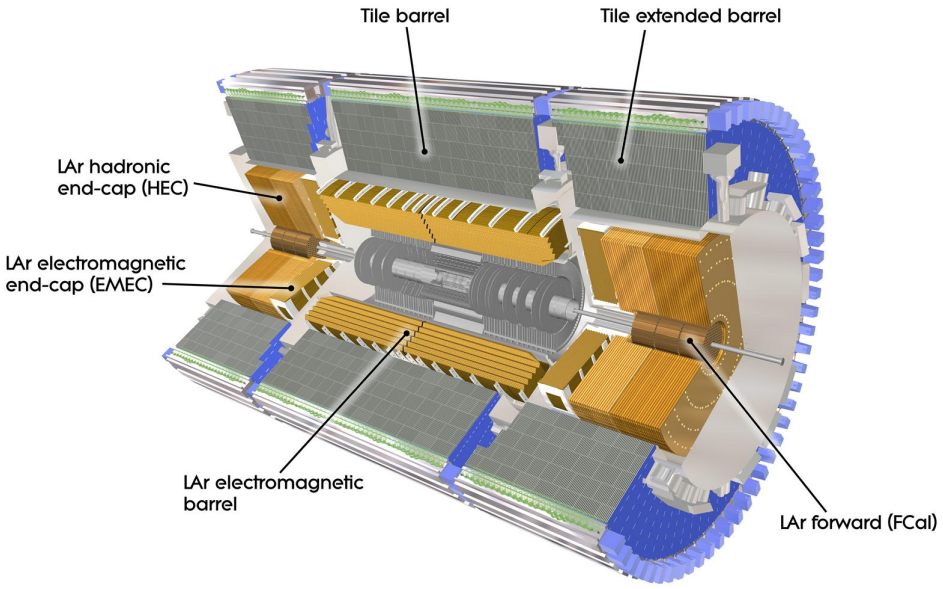

Figure 2.7: Schematic views of the ATLAS calorimeter systems, with the EM LAr calorimeter (gold) and the HAD calorimeter (blue).

in Fig. 2.7. The first one measures the energy and position of electrons and photons, while the second is devoted to the hadrons measurement and identification. The calorimeters cover the range $|\eta| < 4.9$.

One of the most important requirement for a calorimeter is to maintain a good containment of the electromagnetic and hadronic showers. The jets originating from the hadrons should not be able to reach the Muon Spectrometer in order to have a well-precised jet measurement and at the same time a high efficiency in the muon identification.

Electromagnetic Calorimeter

The EM Calorimeter [101] is disposed along the cryostat (7 m long), together with the superconducting solenoid magnet which generates the magnetic field for the inner tracker. It is made up of 1024 lead absorbers in liquid argon (LAr) with an accordion shape. This shape guarantees a complete symmetry in the ϕ plane avoiding at the same time the presence of dead zones. The main goal of the electromagnetic calorimeter is to identify electrons and photons with high precision. It also separates γ's from π's and contributes to the jets reconstruction.

It is divided in a barrel part, with a $|\eta| < 1.475$ coverage, and two end-caps ($1.375 < |\eta| < 3.2$) each one with its own cryostat. In the region dedicated to precision physics ($|\eta| < 2.5$), the EM Calorimeter is segmented in three longitudinal sections: strips, middle and back. While most of the energy of an electron is expected to be released in the middle section, the strips have a fine granularity in order to improve the $\gamma - \pi^0$ discrimination. The back section is dedicated to measure the tails of the high energetic showers and help to distinguish between electromagnetic and hadronic deposits. The width of the EM Calorimeter is more than 22 radiation length (X_0) in the barrel and 24 in the end-caps. It can thus contain electron and photon showers up to 1 TeV. The transition region between the barrel and the end-caps, in the range $1.37 < |\eta| < 1.52$, is expected to have a poor performance due to the presence of a large amount of passive material. This region is often referred as crack region.

To correct for the energy lost by electrons and photons upstream of the EM, a separate presampler detector is used to provide a first sampling of the showers in front of the calorimeter in the $|\eta| < 1.8$ region. The presampler consists of an active LAr layer of thickness 1.1 cm (0.5 cm) in the barrel (end-cap) region.

Hadronic Calorimeter

The HAD Calorimeter [102] extends up to $|\eta| = 3.2$ in coverage. It is composed of three parts realized with different technique: central, end-cap and forward. In the central region, within $|\eta| < 1.7$, the Tile Calorimeter is placed directly outside the EM Calorimeter envelope. The Tile is a sampling calorimeter made of steel as absorbers and scintillating tiles as active material. It is subdivided in a central part (barrel) and two lateral parts (extended barrels), and goes from a inner radius of 2.28 m to an outer radius of 4.25 m. This section of the calorimeter is also used to close the magnetic field flux of the central solenoid magnet. In the $1.7 < |\eta| < 3.2$ region there are the end-cap parts (Hadronic End-cap Calorimeter or HEC). These parts consist of two independent wheels per end-cap, formed of copper plates. The plates are interleaved with 8.5 mm LAr gaps, which provide the active medium for the sampling. They cover the region $1.5 < |\eta| < 3.1$, overlapping both with the Tile and Forward Calorimeters.

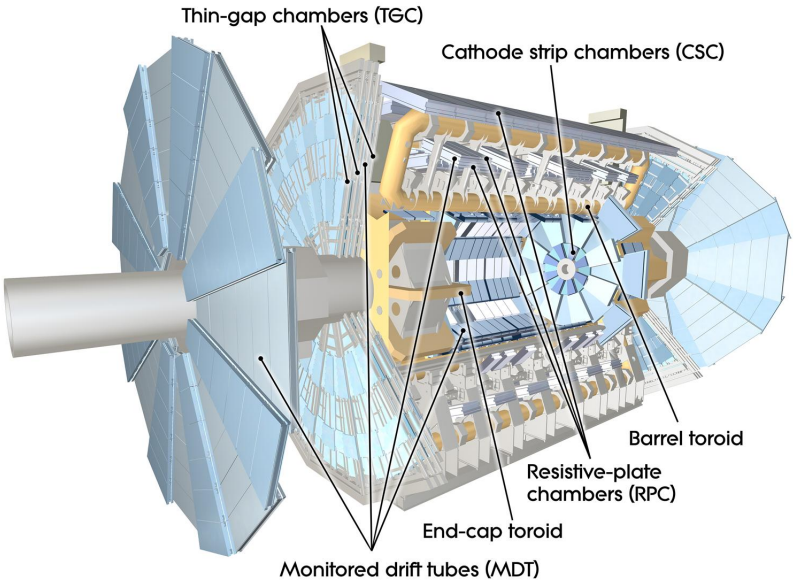

Figure 2.8: Schematic view of the ATLAS Muon Spectrometer.

To complete the η coverage up to $\eta = 4.9$ there is the Forward Calorimeter, another LAr based detector.

2.3.3 Muon spectrometer

The outer layer of the ATLAS detector is the Muon Spectrometer (MS) [103], illustrated in Fig. 2.8. Its main goal is to reveal the passage of muons up to $|\eta| = 2.7$, and to give a quick estimation of the muon momentum by reconstructing its track with a resolution of about 60 μm. The momentum measurement is based on the magnetic deflection of muon tracks. The large volume magnetic field necessary to bend the muon trajectory is provided by a barrel toroid in the region $|\eta| < 1.4$, two smaller end-caps in the region $1.6 < |\eta| < 2.7$ and a combination of the two in the transition region $1.4 < |\eta| < 1.6$. This configuration provides a field which is almost completely orthogonal to the muon trajectory, while minimizing the degradation of the resolution due to multiple scattering.

The measurement is performed over most of the η range in the Monitored Drift Tubes (MDT). At large values of the pseudorapidity, and close to the interaction point, the Cathode Strip Chambers (CSC) have higher granularity than the MDT.

ATLAS is capable of extracting two different and independent measurements of the muon momentum, since the toroidal magnet system of the MS is completely independent from the solenoid in the ID. The reconstruction of the muon momentum can thus be performed with the MS alone or by combining information from the MS and the ID. The different algorithms which are used in ATLAS to reconstruct a muon will be discussed later in the Chapter, together with their reconstruction efficiency and resolution.

The MS can also function as a trigger system to select events of interest. The triggering function covers the range $|\eta| < 2.4$ and is performed by means of the Resistive Plate Chambers (RPC) in the barrel section and the Thin Gap Chambers (TGC) in

the end-cap regions. The RPC are positioned in three concentric cylinders with respect to the beam axis, at radii 5, 7.5 and 10 m far from the interaction point. The end-cap chambers are arranged in four disks at distances 7, 10, 14 and 21-23 m from the interaction point, concentric with respect to the beam axis.

2.3.4 Luminosity and beam detectors

In the forward region three other different sub-detectors are dedicated to the measurement of the luminosity [104], which is a very important parameter for all physics analyses. At ± 17 m far from the interaction point the LUminosity Cerenkov Integrating Detector (LUCID) [105] detects inelastic pp scattering along the beam axis and is the main responsible among the other detectors for the ATLAS luminosity measurement. LUCID is also used, before collisions are delivered by the LHC, to check the beam losses. The Beam Condition Monitor (BCM) is another detector in charge of the beam monitoring.

Located at ± 240 m from the interaction point the Absolute Luminosity For ATLAS (ALFA) [106] is another detector used for luminosity measurement. ALFA consists of scintillating fibre trackers located inside Roman Pots which approach the beam up to 1 mm during measurements.

The last detector is the Zero-Degree Calorimeter (ZDC) [106], located at ± 140 m from the interaction point, just beyond the point where the two independent beam pipes unify together in the common straight-section vacuum pipe which drives to the collision point. The ZDC is composed of modules of layers of alternating quartz rods and tungsten plates which measure neutral particle at $|\eta| > 8.2$.

2.3.5 Trigger system

Considering the design configuration of the LHC, with a luminosity of 10^{34} cm^{-2}s^{-1} and a bunch crossing rate of 40 MHz, the estimated amount of raw data needed to be stored for analyses should be around 1.5 PB/s. Even with the default conditions used by LHC in 2012 (40% of the designed luminosity and a bunch spacing of 50 ns), ATLAS should have recorded $\sim$ 60 TB of raw data per second, which means $\sim$ 1.5 MB per event. These impressive numbers, however, do not match the physical available resources at the CERN Data Centre, which has been set up to store data with a maximum rate of $\sim 300 - 500$ MB/s. For this reason, ATLAS uses a trigger system to reduce the initial data rate by several order of magnitudes.

The ATLAS trigger system [107] is organized in three levels: L1, L2 and the Event Filter (EF).

At L1, all information coming from the MS and from the calorimeters is analyzed by dedicated processors in order to identify Region Of Interest (RoI) and to carry out a first selection. This trigger system acquires information at the LHC frequency and spends about 2 μs to take a decision saving the output with a 75 KHz rate. During this time all the information coming from the subsequent events is not lost but locally stored inside the detector itself.

The L2 trigger has access only to the RoI identified in the previous step but than it uses all the granularity information from each sub-detector. The event frequency is now considerably reduced with respect to the L1, and the L2 trigger can spend up to 40 ms to take a decision without causing dead times. The frequency of accepted events at L2 is almost 3.5 KHz.

Finally, all events which pass the L2 are then processed by the EF by means of analysis programs very similar to those used off-line. The EF takes and uses all possible information coming from the detector, from its geometry and from calibrations. Events which pass also the EF, are written on proper magnetic supports. The rate or frequency at this last level is of about 200-400 Hz.

The L2 and EF are software triggers and form together the High Level Trigger, or HLT. A full combination of L1, L2 and EF is called a trigger "chain". The criteria used for triggering the various physics processes are written in a trigger dedicated "menu" which can be modified depending on the chosen physics program and on the experience acquired during the LHC runs. A menu of possible chains is usually prepared for each data taking run. The menu includes the list of the used triggers, the parameter values for each single trigger and the map to match the low-level trigger with high-level triggers. The most important triggers usually run "unprescaled", which means that they accept all events passing the trigger selection. Other triggers run instead prescaled, i.e. they save events only at a specific rate (usually one every 10).

After the EF, events are divided into "streams", which contain the output of a particular set of chains. On these streams the full off-line events are available and data is saved in the CERN Data Centre, ready to be distributed all around the world.

2.4 Physics objects reconstruction in ATLAS

Given a pp collision, ATLAS is able to reconstruct the event and the final state particles thanks to the information coming from the various subdetectors.

The tracker system records the track of charged particles (electrons, muons, barions and mesons) and by means of the solenoidal magnet field curvature, it determines the sign of the electric charge. The EM and the HAD calorimeters measure the energy deposited by all particles, charged as well as neutral (photons and neutral hadrons), and by calculating the fraction of energy deposited in the two calorimeters, one can distinguish between hadrons, which interact via strong force, leptons and photons, which do not interact via strong force. High energy particles that interact weakly with the calorimeters, such as muons, are detected by the inner tracker and the outer muon chambers and their momentum is measured.

Particle reconstruction is not possible with neutrinos, since they interact only weakly with the detector and do not leave any signal of their passage. Using conservation of total transverse momentum, however, it is possible to retrieve information for these missed particles: the sum of all transverse momenta of the final state particles should be zero, since it can be assumed that the incoming particles before collision have a negligible transverse momentum. The remaining value is called Missing Transverse Energy or E_T^{miss}, and is attributed to the presence of missed particles (see section 2.4.4).

In the following, the ATLAS reconstruction and identification algorithms used to define the various physics objets are described in more details. These definitions will apply for the analyses presented in the next Chapters.

2.4.1 Electrons

The specific requirements of the ATLAS physics program have forced the electron reconstruction algorithms to achieve a large background rejection factor while still providing a good identification efficiency over the full geometric acceptance of the

detector, for electrons with transverse momentum above 10 GeV. The background rejection is needed to separate electrons from hadrons in QCD jets and from secondary electrons originating either from jet decays or from photon conversions in the tracker material.

The electron reconstruction begins with a preliminary identification of a set of cluster energy deposits in the EM Calorimeter [108]. For each reconstructed cluster, the algorithm matches a track in the ID within a specific $\Delta\eta \times \Delta\phi$ range, with respect to the cluster barycenter. Information from the EM Calorimeter is used to determine the energy of the electron.

In order to provide the best discrimination between prompt electrons (i.e. those which originate from the physics process in the interaction point) and the ones from background processes, three reference electron selection criteria have been defined:

- *Loose*: cuts are applied on the amount of hadronic leakage and on the variables describing the shower-shape. Only information from the EM Calorimeter is used. In this case the identification efficiency is excellent but the background rejection is poor.

- *Medium*: both information from the EM Calorimeter and the ID are used. Cuts are applied on the energy deposits in strips of the first layer of the EM Calorimeter and on the tracking variables. Strip-based cuts are chosen to separate π^0's from electrons. The tracking variables include the number of hits in the Pixel Detector, the number of silicon hits in the SCT and the transverse impact parameter z_0 (i.e. the z coordinate of the primary vertex). This set of cuts increases the jet rejection by a factor of six with respect to the loose version, while the identification efficiency is reduced by 4%.

- *Tight*: all the medium selection cuts are applied. Moreover, electrons from photon conversions are further rejected by discriminating on the number of hits in the first layer of the Pixel Detector. Additional cuts on the number of hits in the TRT and on the ratio of high-thresholds hits versus the number of hits in the TRT are also applied to reject the dominant background originating from charged hadrons. Final cuts on the difference between the cluster and the extrapolated track position and on the ratio of cluster energy versus the track momentum are also applied. With this set of cuts, the jet rejection factor is $\sim 10^5$, while the identification efficiency is $\sim 70\%$.

Calibrations of the electron energy, measured from data in Z boson decays, are applied at analysis level.

2.4.2 Muons

Muons are reconstructed by using information from the ID, the calorimeters and the MS. Depending on how this information is used, different muon candidates are built:

- *Stand-alone*: hits in the MS are combined into segments to form a track. The track is used to measure the muon momentum, which is further corrected for the parametrized energy losses in the calorimeter to obtain its value at the interaction point. The track is extrapolated to the beam axis to obtain the muon η and ϕ coordinates and its impact parameter with respect to the interaction point.

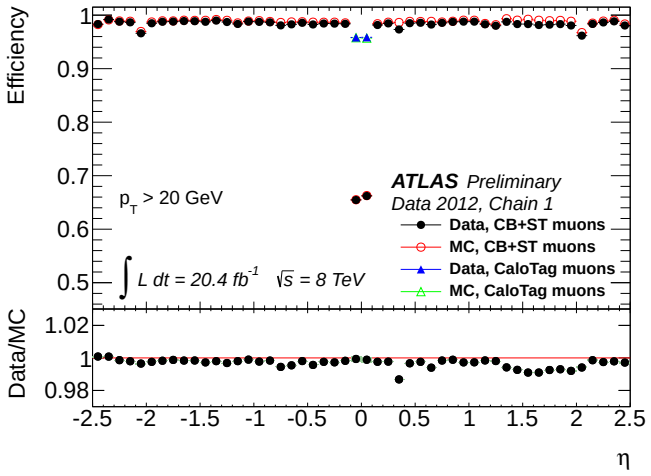

Figure 2.9: Muon reconstruction efficiency, determined from $\sqrt{s} = 8$ TeV data and Monte Carlo simulations, as a function of η for muons with $p_T > 20$ GeV and different muon reconstruction techniques. Calorimeter tagged muons are used only in the region $|\eta| < 0.1$. The panel at the bottom shows the ratio between the measured and predicted efficiencies [109].

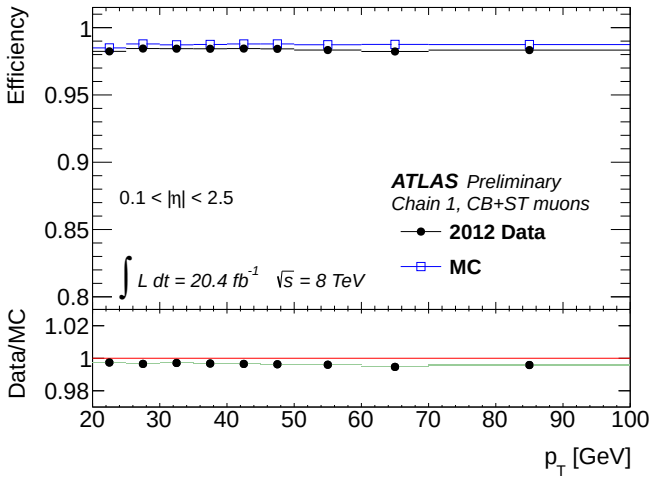

Figure 2.10: Reconstruction efficiency for CB+ST muons, determined from $\sqrt{s} = 8$ TeV data and Monte Carlo simulations, as a function of the muon p_T, for muons with $0.1 < |\eta| < 2.5$. The panel at the bottom shows the ratio between the measured and predicted efficiencies [109].

- *Combined*: stand-alone muon are combined with an ID track. The muon parameters are derived from a combined track fit in the two sub-detectors.

- *Segmented tagged*: an ID track seeds the whole reconstruction process. The algorithm than extrapolates the ID track to segments in the MS in order to build the final track.

- *Calorimeter tagged*: an ID track is identified as muon if the energy deposits in the calorimeters are compatible with those of a minimum ionizing particle.

The elements used by the classes listed above can be obtained in ATLAS with two different algorithms:

- *STACO*: uses a χ^2 approach on a statistical combination of the track vectors to obtain a combined tracks from the ID and the MS [110].
- *MuId*: starts from an ID track and then adds measurements from the MS, refitting the combined track with a χ^2 approach [111].

In the analyses discussed in the next Chapters the STACO algorithm is used to seed the reconstruction process. Combined or Segmented Tagged (CB+ST) muons are than accepted as good candidates.

The muon reconstruction performances of the various criteria described above have been studied in samples with a very high purity, consisting of $Z \to \mu\mu$ decays to a level of more than 99.9%, which have been collected from the 8 TeV data recorded by ATLAS in 2012 [109]. Figures 2.9 and 2.10 illustrate the behavior of the algorithms as a function of η and p_T of the reconstructed object. The efficiency is of the order of 99% for most of the parameter space. The same performances have also been studied in samples containing $J/\psi \to \mu\mu$ events and found to agree within the uncertainties.

2.4.3 Jets

Energy from hadronic particles produced in a collision is mostly deposited in the cells of the ATLAS calorimeter system. To reconstruct a jet from the energy deposits, ATLAS uses algorithms based on topological clusters (topoclusters). Topoclusters are built around seed cells with a signal-to-noise ratio[5] $|\Gamma| > 4$ by iteratively adding neighboring cells with $|\Gamma| > 2$. After the initial clusters are formed, they are analyzed by splitting algorithms. The reconstruction efficiency strongly depends on the algorithm used to analyze the clusters.

The default algorithm adopted by the ATLAS Collaboration is the anti-k$_t$ one [112]. It is a sequential clustering algorithm that defines the distance d_{ij} measured between two identified clusters as:

$$d_{ij} = min(p_{T_i}^{-2}, p_{T_j}^{-2}) \frac{\Delta R_{ij}^2}{R^2}, \tag{2.3}$$

and the distance of a cluster from the beam as:

$$d_{iB} = p_{T_i}^{-2}. \tag{2.4}$$

Here $\Delta R_{ij}^2 = (y_i - y_j)^2 + (\phi_i - \phi_j)^2$, and y_i and p_{T_i} are the rapidity[6] and transverse momentum of object i. The variable R is the parameter of the algorithm which sets the resolution at which jets are identified, and its default value in ATLAS is $R = 0.4$. The algorithm starts by compiling a list of all the distances d_{ij} and d_{iB} around a hard cluster i. The smallest d_{ij} value is found between all the clusters, and if $d_{ij} < d_{iB}$ the entry j is then combined within the hard cluster. The list is updated and the algorithm iterated, until $d_{ij} > d_{iB}$. At the end of the iteration, the entry is considered

[5] The signal-to-noise ratio is defined as $\Gamma = \frac{E_{cell}}{\sigma_{noise}}$, where E_{cell} is the energy deposited in the calorimeter cell and σ_{noise} is the RMS of the energy distribution measured in randomly triggered events and counts both for electronic noise and pile-up.

[6] The rapidity y is defined as $y = \frac{1}{2} \ln(\frac{E+p_z}{E-p_z})$

a jet candidate and removed from the list. By doing this, all soft objects in a cone of $\Delta R < R$ around an hard object are merged together inside the cluster. The algorithm then proceeds by recalculating the distances and repeating the procedures until no entries are left, assembling the hard-clusters in decreasing order of their p_T. Compared to other algorithms, the anti-k$_t$ is less sensitive to low energy constituents, its clustering procedure is faster and the resulting jet area is more regular.

Since the ATLAS calorimeters are non-compensating, the energy of the reconstructed jet is underestimated and a calibration scheme needs to be applied. In the ATLAS analyses presented in the next Chapters, the jets are calibrated with a combination of the EM Jet Energy Scale (EMJES) and Local Hadron Calibration scheme (LC). The EMJES calibration corrects the energy and momentum of jets measured in the calorimeter using a reference jets sample simulated at truth level from Monte Carlo (MC) simulation[7]. The JES calibration is derived as a global function depending on p_T and η. The LC calibration categorizes each topocluster as an electromagnetic or hadronic energy deposit, according to its shape, and assigns a corresponding correction weight on top of the EM calibration. The weights are obtained minimizing the difference between the reconstructed jet energy and the true value in truth reference samples generated with MC simulation.

$b-$quark identification

Jets originating from $b-$quarks fragmentation can be distinguished from light jets (i.e. originating from quarks of the first two generations) through a further identification process known as $b-$tagging. The $b-$tagging exploits the properties of hadrons containing $b-$quarks which have high masses and relatively long lifetimes, since $b-$quarks fly a few millimeters before decaying. Jets containing $b-$quark ($b-$jets) can therefore be tagged either inclusively by measuring the impact parameters of the tracks of the $b-$hadrons decay products, or by explicitly reconstructing a displaced vertex in the jet. Furthermore, it is possible to reveal the semi-leptonic decay of the $b-$quark, which happens only in 11% of the total decay cases, by requiring the additional presence of a lepton candidate inside the jet. This also helps to identify the $b-$jet.

ATLAS developed different algorithms to identify a $b-$jet. They use discriminating variables based on information on the impact parameter and the primary vertex to define a secondary vertex candidate. Each tagging algorithm defines a weight w, associated to the probability for a given jet to have been originated from a $b-$quark. For each tagging algorithm, different working points (i.e. different thresholds on the w variable) can be used. The choice of the working point sets the tagging efficiencies for $b-$jets identification and light jets rejection. The performances of the various $b-$tagging algorithms developed by ATLAS are shown in Fig. 2.11.

The latest algorithm developed by ATLAS is called MV1. It is based on a Neural Network (NN) which uses the output weights of the JetFitterCombNN, IP3D and SV1 algorithms as input [114]. The various algorithms are constructed as follows:

- *SV1*: starts by reconstructing two track vertices significantly displaced from the primary vertex. The algorithm then removes the candidate if its mass is consistent with a K^0_s meson, a Λ^0_s baryon or a photon conversion. For each jet, the tracks contained in all the surviving two-track vertices are fitted to a single

[7] An object is said to be generated at truth level if it is considered upstream of the interaction with the detector. It carries the true values of the initial produced particle associated to the object.

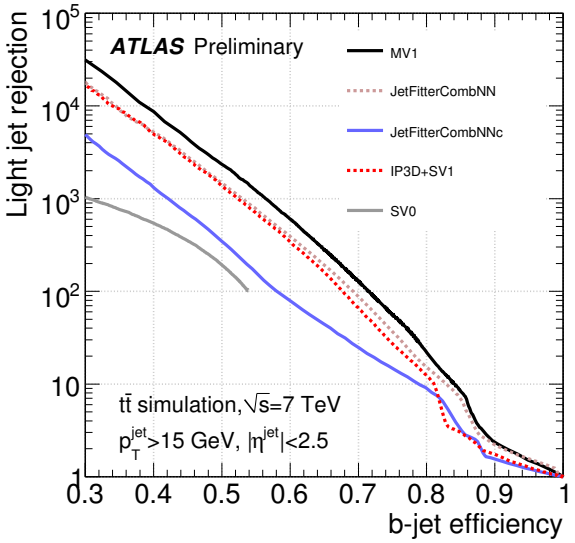

Figure 2.11: Light-jet rejection as a function of the $b-$jet tagging efficiency for the various ATLAS tagging algorithms, for simulated top-antitop events at $\sqrt{s} = 7$ TeV [113].

secondary vertex. The weight w is then defined as the decay length[8] significance, defined as L/σ_L, of the reconstructed secondary vertex.

- *IP3D*: uses the longitudinal and transverse impact parameters significances (defined as $d_0/\sigma(d_0)$ and $z_0/\sigma(z_0)$, respectively) of each track to determine a likelihood probability for the jet to originate from a $b-$quark.

- *JetFitter*: it exploits the topology of weak b and $c-$hadron decays inside the jet, using a Kalman Filter. The discrimination between b, c and light jets is based on a likelihood which uses the masses, momenta, flight-length significances and track multiplicities of the reconstructed vertices as inputs.

- *JetFitterCombNN*: combines the results of the JetFitter and IP3D taggers using an artificial NN to determine a single weight w.

For historical reasons, however, the algorithm used to identify $b-$jets in the analyses presented in the next Chapters (where applicable) is the JetFitterCombNN.

2.4.4 Missing transverse energy

Invisible particles that interact weakly with the detector, such as neutrinos and other possible BSM particles, can be reconstructed from the difference between the initial and final state total transverse momentum. At the LHC, in fact, the initial momentum of the colliding partons along the beam axis is not known a priori, so that the amount of the total missing energy cannot be determined. What can be used is instead the initial momentum transverse to the beam axis which is in good approximation zero

[8]The decay length L is the average distance the particle will travel before decaying.

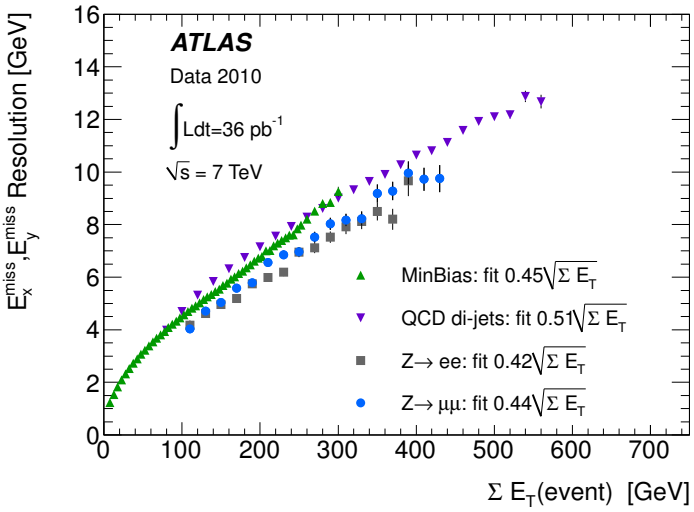

Figure 2.12: $E_{x(y)}^{miss}$ resolution as a function of the total transverse energy (ΣE_T) in 7 TeV events. The resolution of the two components is fitted with a function $\sigma = k \cdot \sqrt{\Sigma E_T}$, and the fitted values of the parameter k is reported [115].

before the collision. The missing energy, E_T^{miss}, can therefore be measured in the transverse plane as:

$$E_T^{miss} = \sqrt{(E_x^{miss})^2 + (E_y^{miss})^2} \tag{2.5}$$

where $E_x^{miss} = -\sum E_x$ and $E_x^{miss} = -\sum E_y$ and E_x and E_y are the energies measured in the transverse plane of the detector.

The default E_T^{miss} collection used by ATLAS for the events reconstruction includes contributions from transverse energy deposits in the calorimeter cells and reconstructed muons. Tracks are added to recover the contribution from low p_T particles which are missed in the calorimeters. The calorimeter cells are associated to a reconstructed object in a precise order: electrons, photons, jets and muons. The E_T^{miss} is than calculated by adding the different terms as follows:

$$E_{x(y)}^{miss} = E_{x(y)}^{miss,e} + E_{x(y)}^{miss,\gamma} + E_{x(y)}^{miss,jets} + E_{x(y)}^{miss,\mu} + E_{x(y)}^{miss,CellOut} \tag{2.6}$$

The collection uses medium electrons with $p_T > 10$ GeV, photons with $p_T > 10$ GeV, jets with $p_T > 20$ GeV calibrated at LC+EM level, and muons satisfying the baseline selection with $p_T > 10$ GeV. The CellOut component is computed from locally calibrated topoclusters and tracks which are not associated to any reconstructed objects. The hadronic taus are included either in the jet term or in the CellOut term, while soft jets with $10 < p_T < 20$ GeV are included in the CellOut term.

The E_T^{miss} performance is evaluated with a quantitative study of its resolution, as a function of the total transverse energy in the event. The resolution is measured in physics processes where it is possible to assume that the true value of E_T^{miss} is zero, such as $Z \to ee$ and $Z \to \mu\mu$ events. Fig. 2.12 shows the resolution for events with a center of mass energy of 7 TeV. A good agreement is found in the different physics channels.

A degradation of the E_T^{miss} resolution has been observed for events at 8 TeV due to the increased number of average interactions per bunch crossing μ (pile-up effect), which raised from $<\mu>=6.3$ at 7 TeV to $<\mu>=20.7$ at 8 TeV [116]. A method to correct the pile-up effect has been studied by scaling the soft jets contribution in the CellOut term ($E_{x(y)}^{miss,soft}$) with the soft term vertex fraction, which is the fraction of tracks matched to the $E_{x(y)}^{miss,soft}$ which are associated with the primary vertex. However, this method has been found to worsen the sensitivity of the analysis at 8 TeV presented in this thesis and is not applied hereafter.

In the evaluation of the uncertainties of the analyses documented in this thesis, uncertainties on the measurement of leptons and on the jet energy scale and resolution are automatically propagated to the calculation of E_T^{miss}. Additional uncertainties which come from the topoclusters reconstructed outside any object and from soft jets are evaluated separately, as described in the next Chapters.

3

Search for top squarks in final states with two leptons

This Chapter gives an introduction to the top squark production and decay processes in the context of natural SUSY and illustrates the general motivations and strategies behind a search for direct production of top squarks in the final states with two leptons at the ATLAS experiment.

3.1 The top squark particle

In Chapter 1, it has been discussed that the MSSM predicts the existence of a super-partner of the top quark ("top squark" or "stop"), and that two distinct physical states $\tilde{t}_1$ and $\tilde{t}_2$ can emerge due to the mixing between the two interaction states $\tilde{t}_L$ and $\tilde{t}_R$. It has also been seen that the lightest of these two states, $\tilde{t}_1$, can be constrained below the threshold of one TeV in a natural SUSY scenario in order to avoid fine-tuning the MSSM parameters. The stop can thus result the lightest squark in most of the MSSM parameter space and its mass can be accessible at the energies of the LHC, manifesting a chance to reveal natural SUSY at colliders.

In this context, there are mainly two types of production processes which can originate a stop at the LHC. One is via the decay of a gluino ($\tilde{g} \to t\tilde{t}_1$) and the other is via direct production ($\tilde{t}_1\tilde{t}_1$). The latter process has a smaller cross section with respect to the production of pairs of gluinos, as illustrated in Fig. 3.1, but it may dominate if the gluinos masses are above the TeV scale and their production is not accessible at the available energies.

The stop can then decay in a variety of modes, all leading to the presence of the LSP in the final state. The process and the total composition of the final state, however, depend on the mass hierarchy among the SUSY particles, as illustrated in the phase space represented in Fig. 3.2. If only the lightest stop, the lightest chargino and the lightest neutralino (which is then assumed to be the LSP) are considered as the active SUSY particles, i.e. the other SUSY particles are assumed to be heavy enough such that they decouple, than four main scenarios can be identified:

- In the kinematic region $m(\tilde{t}_1) - m(\tilde{\chi}_1^0) > m(t)$ (yellow region), the stop decays to a top quark and the lightest neutralino ($\tilde{t}_1 \to t\tilde{\chi}_1^0$).
- Throughout all the phase space, but only if the lightest chargino is lighter than the stop, the decay mode $\tilde{t}_1 \to b\tilde{\chi}_1^\pm$ is also accessible.

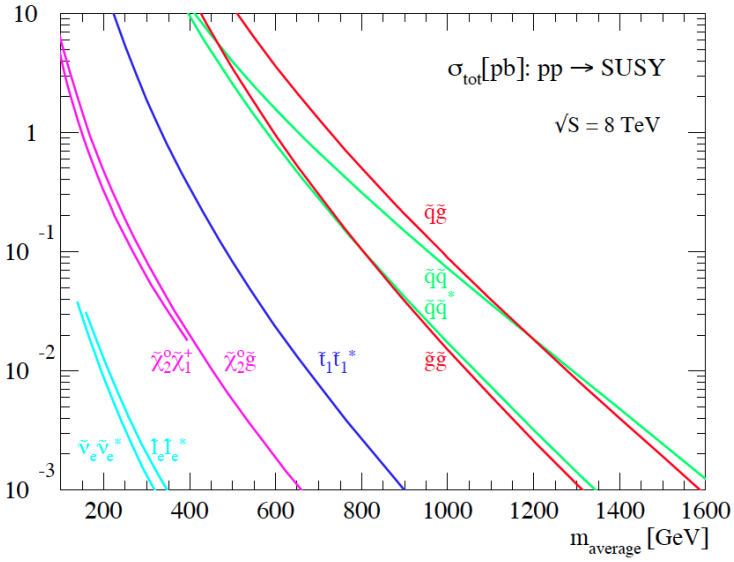

Figure 3.1: Production cross sections (in pb) of pairs of SUSY particles, as a function of the mass scale, for $\sqrt{s} = 8$ TeV pp collisions.

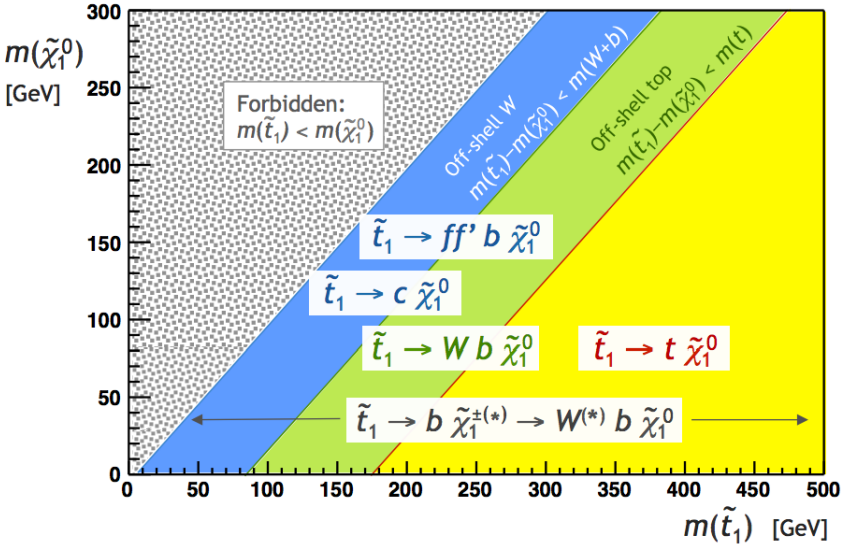

Figure 3.2: Stop decay as a function of $\tilde{t}_1$ and $\tilde{\chi}_1^0$ mass.

- If, however, $m(\tilde{t}_1) - m(b) < m(\tilde{\chi}_1^{\pm})$ and $m(\tilde{t}_1) - m(\tilde{\chi}_1^0) < m(t)$, the preferred scenario is a three-body decay of the stop to a b quark, a W boson and the neutralino ($\tilde{t}_1 \to Wb\tilde{\chi}_1^0$), represented in the figure by the green region.
- If all the two-body and three-body channels described above are forbidden, such as in the kinematic region where also the W boson is off-shell, the stop can decay via $\tilde{t}_1 \to ff'b\tilde{\chi}_1^0$ (four-body decay, light blue region), where f and f' are any SM fermions. Alternatively, the decay of the stop can lead to a production of a charm quark and the lightest neutralino via loop: $\tilde{t}_1 \to c\tilde{\chi}_1^0$.

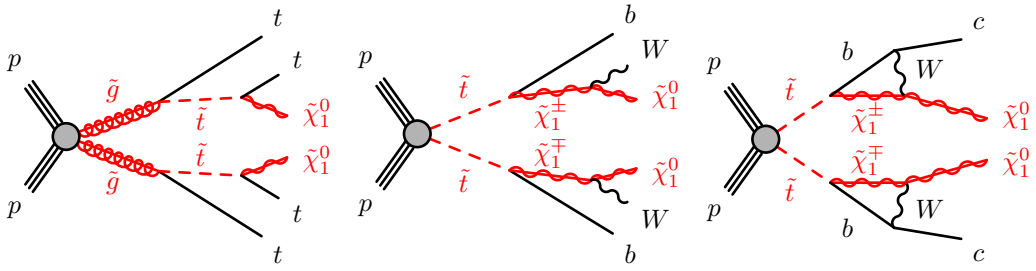

Figure 3.3: Feynman diagrams for stop production and decay. Left: gluino mediated production and decay to a top quark and $\tilde{\chi}_1^0$. Middle: direct production and decay to a $b-$quark and $\tilde{\chi}_1^\pm$. Right: direct production and decay to a charm quark and $\tilde{\chi}_1^0$ via loop.

The exact phenomenology depends however on the combination of the free parameters of the model. Some of the Feynman diagrams of the cited production and decay modes are shown in Fig. 3.3 and Fig. 3.4.

The history of the search for the stop begins in the early 90's, when the LEP experiments set the first limits on its mass, excluding $m(\tilde{t}_1) < 96$ GeV for a $\tilde{t}_1 \to c\tilde{\chi}_1^0$ final state [117]. CDF and D0 also performed various searches assuming direct production at the Tevatron. CDF performed searches in the $\tilde{t}_1 \to b\tilde{\chi}_1^\pm$ decay channel with dileptonic final states, and placed limits in the stop and neutralino mass plane for different BR of the leptonic chargino decay and for fixed values of $m(\tilde{\chi}_1^\pm)$. In the case of $m(\tilde{\chi}_1^\pm) = 105.8$ GeV and $m(\tilde{\chi}_1^0) = 47.6$ GeV, stop masses between 128 and 135 GeV were excluded [118, 119]. Other searches excluded stop masses below 180 GeV in the $\tilde{t}_1 \to c\tilde{\chi}_1^0$ decay mode, for a neutralino lighter than 95 GeV [120, 121]. The challenge to extract the signal was in these analyses increased due to the large background of top quark pairs, whose production has larger cross section and similar kinematic.

After the start of the LHC, however, the ATLAS and CMS experiments have continuously enlarged the exclusion coverage on the decay phase space of the stop. Searches with missing transverse momentum, jets and possibly leptons started to proliferate as soon as the integrated luminosity increased and the LHC program switched to collisions at $\sqrt{s} = 8$ TeV in 2012, revealing a chance to access the light cross section region of the stop pair production. Specific analyses were then developed and optimized for single decay channels, in order to cover as much as possible the sensitivity to a wide range of the decay phase space.

From the results of these analyses, exclusion limits on the masses of the stop, chargino and neutralino have been derived at 95% CL under certain conditions on the mass hierarchy and decay channel. In the following, some of the ATLAS results are presented.

In a simplified model considering a $\tilde{t}_1 \to t\tilde{\chi}_1^0$ decay channel with 100% BR, stop and neutralino masses have been constrained. A search with full hadronic final states excluded stop masses up to 680 GeV for a nearly massless neutralino [85]. A monojet search using $c-$tagging excluded stop masses below 200 GeV where also the W boson is off-shell and the stop undergoes the decay $\tilde{t}_1 \to c\tilde{\chi}_1^0$ via loop [122].

In the $\tilde{t}_1 \to b\tilde{\chi}_1^\pm$ scenario, searches with jets and leptons placed limits on the stop and neutralino masses under certain constraints on the chargino mass. The most stringent limits excluded stop masses below 600 GeV for a neutralino mass around 100 GeV and a chargino nearly degenerate with the neutralino [88].

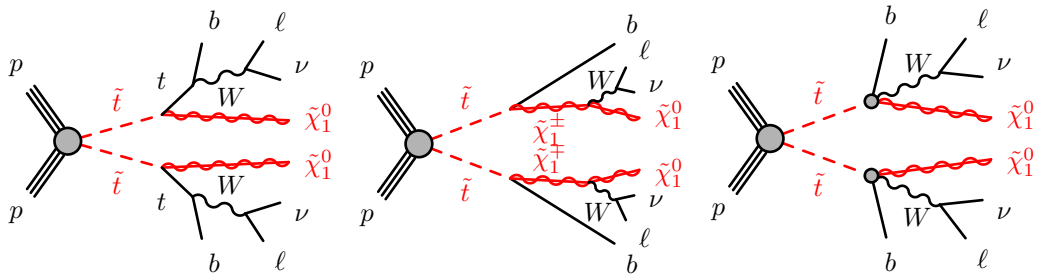

Figure 3.4: Feynman diagram of stop pair production and decay with two leptons in the final state. Left: each stop decays to a top quark and a $\tilde{\chi}_1^0$. Middle: each stop decays to a bottom quark and a $\tilde{\chi}_1^{\pm}$. Right: each stop undergoes a three-body decay to a bottom quark, a W boson and a $\tilde{\chi}_1^0$.

In summary, stop masses below 600-700 GeV are largely excluded both in the $\tilde{t}_1 \to t\tilde{\chi}_1^0$ and $\tilde{t}_1 \to b\tilde{\chi}_1^{\pm}$ decay modes. A recent result from the CMS experiment, moreover, excluded a stop mass up to 740 GeV in the $\tilde{t}_1 \to t\tilde{\chi}_1^0$ channel [123]. This is, at the time of writing, the highest constraint on the stop mass assuming direct production at colliders. It shows how the increased energy of the LHC allowed to access points in the kinematic regions with lower cross sections and to place limits on a wider range of masses with respect to what was done by the LEP and the Tevatron colliders. The results have however to be interpreted with caution, due to all the theoretical assumptions on the production and decay processes.

3.2 Motivations and overview of the search for the top squark

Among the searches presented above, analyses based on two isolated leptons (e or μ) and missing transverse energy in the final state have often been considered a promising venue for the discovery and measurement of the stop at the LHC. Two leptons are expected to be produced in the final states of many decay processes involving charginos or top quarks, while a large deviation of the momentum balance can be a hint of the presence of LSPs in the final state.

The work documented in this thesis describes a search for pair production of stop in final states with two leptons (e or μ), $b-$jets and weakly interacting particles which escape the detection (neutrinos and neutralinos), using pp collisions recorded by the ATLAS experiment in 2011 and 2012.

The final state described above is representative of various decay chains:

$$\tilde{t}_1\tilde{t}_1 \to t\tilde{\chi}_1^0\bar{t}\tilde{\chi}_1^0 \to bl^+\nu\tilde{\chi}_1^0\bar{b}l^-\bar{\nu}\tilde{\chi}_1^0\,, \tag{3.1}$$

$$\tilde{t}_1\tilde{t}_1 \to b\tilde{\chi}_1^+\bar{b}\tilde{\chi}_1^- \to bl^+\nu\tilde{\chi}_1^0\bar{b}l^-\bar{\nu}\tilde{\chi}_1^0\,, \tag{3.2}$$

$$\tilde{t}_1\tilde{t}_1 \to bW^+\tilde{\chi}_1^0\bar{b}W^-\tilde{\chi}_1^0 \to bl^+\nu\tilde{\chi}_1^0\bar{b}l^-\bar{\nu}\tilde{\chi}_1^0\,, \tag{3.3}$$

where $l^{\pm}$ here stands for e or μ.

The decay process of equation 3.1 requires $m(\tilde{t}_1) - m(\tilde{\chi}_1^0) > m(t)$, i.e. the top quark must be on-shell, and leads to a final state with two leptons only in 4.9% of the cases, considering the BR of the semi-leptonic decay of a top quark in both legs. The decay of equation 3.2 requires $m(\tilde{t}_1) - m(\tilde{\chi}_1^{\pm}) > m(b)$, while the pattern described by equation 3.3 describes a three-body decay of the stop to a $b-$quark, a W boson and a neutralino: $\tilde{t}_1 \to bW\tilde{\chi}_1^0$. This latter mode is expected to dominate if $m(\tilde{t}_1) < m(\tilde{\chi}_1^{\pm})$ and $m(W) < m(\tilde{t}_1) - m(\tilde{\chi}_1^0) < m(t)$, i.e. the top quark is off-shell and the W boson is on-shell. In all three scenarios, the final state is the same as for the leptonic decay of a pair of top quarks, which constitutes the largest source of background. Feynman diagrams of the cited processes are illustrated in Fig. 3.4.

The search uses pp collisions collected by the ATLAS experiment at a center of mass energy $\sqrt{s} = 7$ TeV in 2011, and at $\sqrt{s} = 8$ TeV in 2012. The two cases are treated separately since they present some differences on the event selections, on the SM background evaluation techniques, and on the interpretation of the results. The case with $\sqrt{s} = 7$ TeV data is optimized for a simplified model assuming the decay $\tilde{t}_1 \to t\tilde{\chi}_1^0$ of equation 3.1. In the case with $\sqrt{s} = 8$ TeV data, the event selections have been revised to optimize the sensitivity for the simplified models described by equations 3.2 an 3.3. The common analysis strategy is however based on a cut-and-count approach, which makes use of the m_{T2} variable [124,125] in order to discriminate the SUSY signal from the SM background sources.

In this cut-and-count approach, pre-selections are firstly imposed to reduce the rate of events of interest which are then analyzed. The event is then reconstructed and a sequence of selection cuts is applied to reduce the contribution from the SM background processes. At the end of this sequence, a cut on m_{T2} defines the Signal Regions (SR), in which the observed number of events from data is compared to the prediction of the remaining SM background. The comparison is done via data-driven techniques or with the aid of MC simulations. The main sources of SM background, which for this analysis are $t\bar{t}$, dibosons (WW, WZ and ZZ) and Z/γ^*+jets processes, are measured in background-enriched dedicated regions, named Control Regions (CR), by comparing data with MC simulations, and are then extrapolated to the SRs by means of transfer factors, resulting in a semi data-driven measurement. The other minor sources, such as single top (Wt channel), $t\bar{t}W$ and $t\bar{t}Z$, are measured directly from MC simulation in the SR. A non negligible source of background coming from leptons which are mis-reconstructed in the detector (fake leptons) is measured using a data-driven technique. This last source mostly consists of semi-leptonic $t\bar{t}$, s and $t-$channel single top, W+jets and light and heavy-flavour jet production from QCD. Uncertainties due to experimental setup, MC models, or related to the methods used in the background estimate, are considered in the analysis.

At the end of the process, results are used to seek for a significative excess over the SM predictions, or in case of absence of any excess, to constrain the parameters of the models by placing exclusion limits on the SUSY production cross sections and on the superpartner masses.

The rest of this Chapter is organized as follows. Section 3.3 illustrates the m_{T2} variable and how it is used in the analysis. Section 3.4 presents the MC samples used for the simulation of signal models and the SM background processes. In Section 3.5, the trigger chains used to pre-select events of interest are described in more details together with the data samples. Section 3.6 describes the object reconstruction process and the event selections, for the 7 TeV and 8 TeV cases. The treatment of uncertainties

associated to the SM background is then presented in Section 3.7, while Section 3.8 describes the general strategy for the measurement of background arising from fake leptons.

Chapters 4 and 5 will then present the results for the $\sqrt{s} = 7$ TeV and $\sqrt{s} = 8$ TeV cases, respectively, with a detailed descriptions of the technique used to estimate the SM background.

3.3 The m_{T2} variable

The m_{T2} variable, sometimes also called "stransverse mass", is a generalization of the transverse mass m_T in the case where two identical particles are produced in two legs of the decay chain, and both decay to one particle which can be observed and one which remains invisible (see Fig. 3.5). In the case of this analysis, the observed particles are the leptons (e or μ) and therefore the m_{T2} is also labelled m_{T2}^{ll}.

Considering only one leg and the production of a lepton and a neutrino, the transverse mass of a lepton-neutrino system is defined as

$$m_T(l,\nu) = \sqrt{2p_T(l)p_T(\nu)[\cos(\Delta\phi_{l\nu})]} \tag{3.4}$$

and is limited by the W boson mass for SM events involving a W boson decay: $m_T(l,\nu) < m(W)$.

The limitation still persists if we consider the maximum of the transverse masses in the case of a system with two legs:

$$\max[m_T(\vec{p}_T^{\,1}, \vec{q}_T^{\,1}), m_T(\vec{p}_T^{\,2}, \vec{q}_T^{\,2})] < m(W), \tag{3.5}$$

where $\vec{p}_T^{\,1(2)}$ is the momentum of the first (second) lepton and the vector sum of the transverse momenta of the two invisible particles gives the overall missing momentum in the transverse plane ($\vec{q}_T^{\,1} + \vec{q}_T^{\,2} = \vec{p}_T^{\,miss}$), whose magnitude is exactly E_T^{miss}.

In this case the direction of the two neutrinos remains unknown, but it is possible to try all combinations and take the lower bound. To do so, the maximum between the two transverse masses built with one lepton and each combination of the invisible momenta is considered:

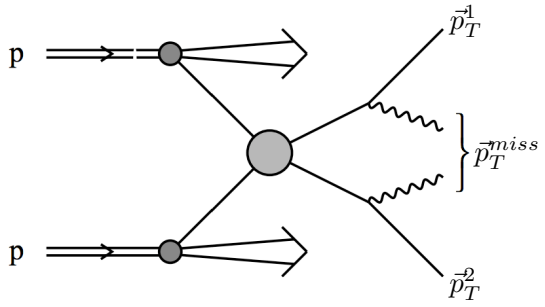

Figure 3.5: Diagram of the production of a pair of particles, each decaying into one particle that is observed with momenta p and one invisible particle, whose presence can only be inferred from the missing transverse momentum.

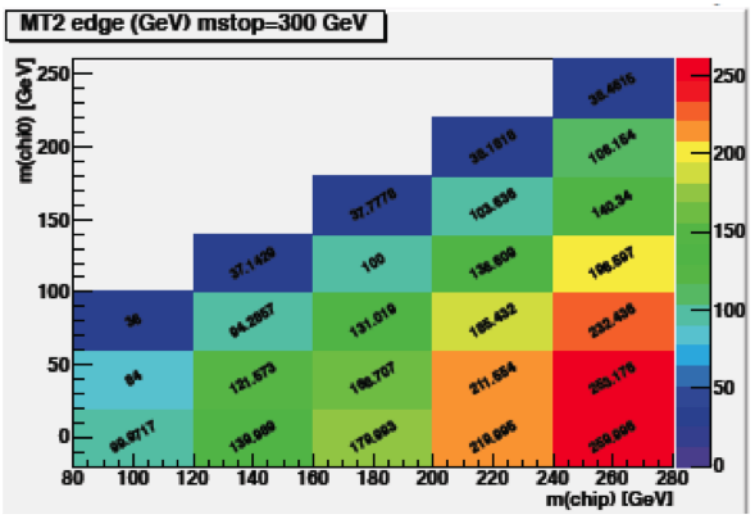

Figure 3.6: Kinematic edge of m_{T2}^{ll} as a function of $\tilde{\chi}_1^{\pm}$ and $\tilde{\chi}_1^0$ mass, for a 300 GeV stop.

$$m_{T2}(\vec{p}_T^{\,1}, \vec{p}_T^{\,2}, \vec{p}_T^{\,miss}) = \min_{\vec{q}_T^{\,1}+\vec{q}_T^{\,2}=\vec{p}_T^{\,miss}} \max[m_T(\vec{p}_T^{\,1}, \vec{q}_T^{\,1}), m_T(\vec{p}_T^{\,2}, \vec{q}_T^{\,2})]. \tag{3.6}$$

It can be observed at this point that the minimum value over all possible combinations is still lower than the end-point for the decay on a single leg.

For SM events ($t\bar{t}$, WW and Wt) the value of m_{T2}^{ll} has an upper bound equal to the end-point for the W boson decay, which is the W boson mass. For the signal model of equation 3.1, the E_T^{miss} receives a contribution from the neutralinos produced in the stop decay and therefore the end-point depends on the mass hierarchy between the stop and the $\tilde{\chi}_1^0$, and increases with increasing mass difference $m(\tilde{t}_1) - m(\tilde{\chi}_1^0)$. The analysis is therefore sensitive to values of the hierarchy with an m_{T2}^{ll} end-point extending beyond the W boson mass. By selecting events with $m_{T2}^{ll} > m_W$ it's thus possible to enhance the signal over background ratio in the analysis.

In the case of equation 3.2, the end-point is driven by the mass difference $m(\tilde{\chi}_1^{\pm}) - m(\tilde{\chi}_1^0)$, as shown in Fig. 3.6 in the case of a 300 GeV stop. The larger is the mass splitting, the higher is the endpoint. The analysis is therefore more sensitive to models with large mass difference between $\tilde{\chi}_1^{\pm}$ and $\tilde{\chi}_1^0$.

3.4 Monte Carlo simulation

MC generators are used to simulate the SUSY signal models and to help in the background description. The predictions of the main background sources are normalized to data in some specific CRs, and then extrapolated to the SRs by means of transfer factors. Sources whose contribution in the SR is small or negligible are measured directly from MC. Moreover, in the CRs, simulations are also used to estimate and subtract the contribution of other minor processes different from that targeted by the measurement.

The dominant SM background processes for the search documented in this thesis include $t\bar{t}$, Wt, $WW \to l\nu l\nu$, ZZ/ZW, and Z/γ^*. Production of top quark pairs is simulated using the MC@NLO [126,127] generator, interfaced with the HERWIG [128]

and JIMMY [129] simulators for the fragmentation and the hadronization processes. The top mass is fixed at 172.5 GeV in all simulations, and the set CTEQ10 [130] (CT10 [131] for the 8 TeV case) is used for the description of the Parton Distribution Functions (PDFs), i.e. the momentum distribution functions of the partons within the proton. Additional MC samples help to estimate the event generator systematic uncertainties, as described in Section 3.7: two POWHEG [132] samples, one interfaced with PYTHIA [133] and the other with HERWIG, an ALPGEN [134] sample, interfaced with HERWIG, and two ACERMC [135] samples produced by varying the PYTHIA parton shower parameters in order to reproduce the radiation consistently with data. Wt production is simulated using MC@NLO interfaced with HERWIG. Z/γ^* samples produced in association with light and heavy-flavour jets are generated for the 7 TeV analysis with ALPGEN using the PDF set CTEQ6.1 [136]. For the 8 TeV results, the nominal generator has been switched to the SHERPA [137] generator, using the PDF set CT10, while ALPGEN is considered for systematic uncertainty evaluation due to the generator choice. Dibosons samples ($WW/WZ/ZZ$) are generated with SHERPA for the 7 TeV case, using ALPGEN and HERWIG for the evaluation of the systematic uncertainties. For the 8 TeV case, POWHEG is used as nominal generator, while SHERPA is used for the evaluation of the generator systematic uncertainty. Samples for $t\bar{t}$ production in association with W/Z bosons are generated using MADGRAPH [138] interfaced with PYTHIA and using the PDF set CTEQ6.1. For the 8 TeV analysis, additional samples considering a SM Higgs production and decay are simulated with PYTHIA8 [139]. These samples include Higgs production via gluon

Physics process	σ·BR [pb] (7 TeV)	σ·BR [pb] (8 TeV)	Perturb. order
$t\bar{t} \to l + X$	91	-	NLO+NNLL
$t\bar{t} \to ll + X$	-	26.6	NNLO+NNLL
Wt	15.7	-	NLO+NNLL
Wt	-	22.4	NNLO+NNLL
$Z/\gamma^\star \to ll$, $m(ll) > 12$ GeV	1069	-	NNLO
$Z/\gamma^\star \to ll$, $m(ll) > 40$ GeV	-	1240	NNLO
$ZZ \to llll$	0.27	0.78	NLO
$ZZ \to ll\nu\nu$	0.24	0.5	NLO
$WZ \to lll\nu$	1.36	9.8	NLO
$WW \to ll\nu\nu$	2.98	5.83	NLO
$t\bar{t}W$	0.17	0.23	NLO
$t\bar{t}Z$	0.13	0.20	NLO
$H \to ZZ \to ll\nu\nu$	-	0.024	NLO
$H \to WW \to ll\nu\nu$	-	0.24	NLO
$WH \to WWW \to ll + X$	-	0.018	NLO
$ZH \to ZWW \to ll + X$	-	0.009	NLO
$WH \to l\nu b\bar{b}$	-	0.13	NLO
$ZH \to llb\bar{b}$	-	0.023	NLO

Table 3.1: The most important SM background processes considered in the analyses and their production cross sections, listed separately for $\sqrt{s} = 7$ TeV and $\sqrt{s} = 8$ TeV. The production cross section is multiplied by the branching ratio of the leptonic decays indicated in the first column, where $l = e, \mu$, or τ.

fusion, vector boson fusion, or in association with a W or Z boson. In all simulations, the Higgs boson mass is fixed at 125 GeV.

Tables 3.1 summarizes the samples used in the analyses, together with their cross sections at 7 TeV and 8 TeV.

The background predictions are normalized to the theoretical cross sections, including higher-order QCD corrections. Next-to-leading order (NLO) cross sections are used in the diboson samples, the Higgs samples and for the $t\bar{t}W$ and $t\bar{t}Z$ samples. Inclusive cross sections for Z/γ^*+jets are calculated at the next-to-next-to-leading order (NNLO). The normalizations of the $t\bar{t}$ and Wt samples are obtained using NLO+NNLL (next-to-next-to-leading-logarithm) cross sections for the 7 TeV case and NNLO+NNLL cross sections for the 8 TeV case.

All samples are processed through a full ATLAS detector simulation [140] based on GEANT4 [141], or through a fast simulation using a parametrization of the performances of the electromagnetic and hadronic calorimeters [142]. Effects due to the overlapping of two or more pp interactions in the same event (pile-up) are also included in the simulation. The events are weighted so that the distribution of the average number of interactions per bunch crossing matches that in data.

SUSY signal samples are generated for the 7 TeV analysis in the context of the simplified model described by equation 3.1. A sample grid based on the two parameters $m(\tilde{t}_1)$ and $m(\tilde{\chi}_1^0)$ is produced with stop masses ranging from 100 GeV to 500 GeV and a granularity which goes from 25 GeV for lower masses to 100 GeV for the highest mass values. Samples are generated with the HERWIG++ [143] generator, and the mixing in the stop and gaugino sectors have been chosen such that the lightest stop is mostly the $\tilde{t}_R$ and the lightest neutralino is a pure bino. Under such conditions, the stop is expected to decay almost exclusively to a top quark and the lightest neutralino.

For the 8 TeV analysis, the two different decay patterns described by equations 3.2 and 3.3 are considered separately. In the first case, grids on the three $m(\tilde{t}_1)$, $m(\tilde{\chi}_1^{\pm})$ and $m(\tilde{\chi}_1^0)$ parameters are produced, with stop masses ranging from 150 GeV to 600 GeV and a granularity which goes from 25 GeV for lower masses to 100 GeV for the highest mass values. The sample grids are generated with MADGRAPH and showered with PYTHIA. To maximize the sensitivity, and to help in the interpretation of the results, projections of the three-dimensional decay phase space have been considered:

- for a neutralino mass set to 1 GeV, the chargino and stop mass plane is scanned;
- for a fixed mass difference $m(\tilde{t}_1) - m(\tilde{\chi}_1^{\pm}) = 10$ GeV, the neutralino and stop mass plane is scanned;
- for a fixed stop mass $m(\tilde{t}_1) = 300$ GeV, the $m(\tilde{\chi}_1^{\pm})$ vs $m(\tilde{\chi}_1^0)$ plane is scanned;
- for a fixed chargino mass $m(\tilde{\chi}_1^{\pm}) = 2 \times m(\tilde{\chi}_1^0)$, the $m(\tilde{\chi}_1^0)$ vs $m(\tilde{t}_1)$ plane is scanned;
- for a fixed chargino mass $m(\tilde{\chi}_1^{\pm}) = 150$ GeV, the $m(\tilde{\chi}_1^0)$ vs $m(\tilde{t}_1)$ plane is scanned.

In all cases the $\tilde{\chi}_1^{\pm}$ mass starts from 100 GeV, consistently with the LEP chargino limits. The granularity of some of these grids can be appreciated in Fig. 3.10 and Fig. 3.11 of Section 3.6.2, where a study of the sensitivity of the search is presented.

For the three-body decay scenario of equation 3.3, the grid is generated from the masses of the stop and the neutralino. The grid points require $m(W) < m(\tilde{t}_1) -$

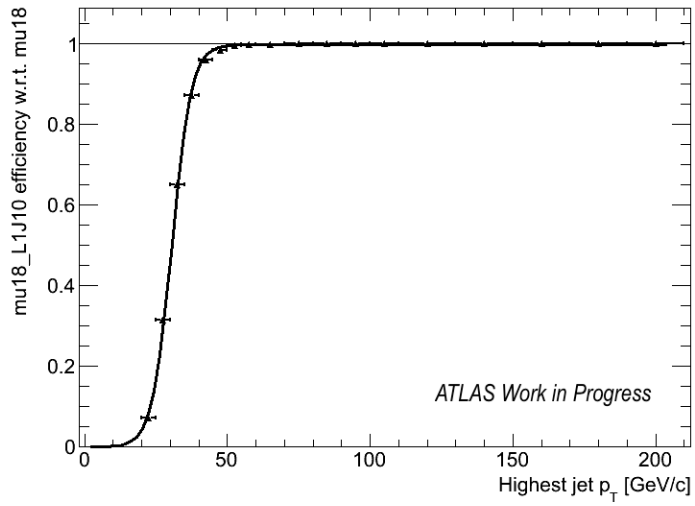

Figure 3.7: Ratio of the efficiency of the mu18 and mu18_L1J10 triggers as a function of the highest jet p_T in the event, measured in 7 TeV data by using a Tag&Probe method with a Z boson, on muon triggered events. A fit to a Fermi function is superimposed to the data.

$m(\tilde{\chi}_1^0) < m(t)$ and neutralino masses are generated up to 260 GeV. The samples are produced using the HERWIG++ generator.

In all cases signal cross sections are calculated at NLO in perturbative QCD. Moreover, different initial-state and final-state radiation and different values of the strong coupling constant have been used to produce additional samples for the evaluation of the effect of systematic uncertainties.

3.5 Trigger and data sample

The search uses all pp collisions recorded by ATLAS in 2011 and 2012, delivered by the LHC at a center of mass energy of $\sqrt{s} = 7$ TeV and $\sqrt{s} = 8$ TeV, respectively. After beam, detector and data quality requirements, a total integrated luminosity of 4.7 fb^{-1} at 7 TeV and 20.3 fb^{-1} at 8 TeV are left for analysis.

Data is collected based on the decision of the three-level ATLAS trigger system, and categorized according to the periods of the year in which it was delivered by the LHC.

For the 7 TeV analysis, events are accepted if they pass the single lepton (e or μ) triggers. A threshold on the lepton p_T is imposed by the trigger to reject background events with low momentum leptons. The value of the threshold depends on the instantaneous luminosity of the detector and varies from 20 GeV to 22 GeV, for electrons, and 18 GeV for muons, depending on different data periods. For the muon trigger and starting from late periods characterized by high instantaneous luminosity values, the trigger requirement also includes a jet selection at L1. This selection is fully efficient for events with an offline jet of $p_T > 50$ GeV, as can be observed in Fig. 3.7. The

Period	Egamma trigger	Muon trigger
B to I	e20_medium	mu18
J	e20_medium	mu18_L1J10
K	e22_medium	mu18_L1J10
L, M	e22vh_medium1 or e45_medium1	mu18_L1J10

Table 3.2: Trigger chains used in the analysis with $\sqrt{s} = 7$ TeV data, listed separately for each data period. The numbers refer to the lepton p_T threshold imposed by the trigger. Triggers with the 'vh' label apply a cut on the hadronic core isolation ($\leq$1 GeV) at L1. The 'medium' label in the electron triggers refers to the object definitions described in Section 2.4.1. 'L1J10' indicates a requirement of a 10 GeV jet at L1.

analysis selections reach a plateau efficiency of about 97% for electrons with $p_T > 25$ GeV and 90% (75%) in the barrel (end-caps) region for events including muon with $p_T > 25$ GeV and jets with $p_T > 50$ GeV. Table 3.2 lists the triggers used for each period number of the year 2011 (B-M).

For the 8 TeV analysis, a combination of single (e or μ) and dilepton (ee, $\mu\mu$, $e\mu$) triggers is used to select events. An event is accepted if it passes the logical OR of all the chains listed in Table 3.3. All triggers contain a threshold selection on the lepton transverse momentum. In order to be in the single lepton triggers efficiency plateau, both electrons and muons must have $p_T > 25$ GeV. Electrons are in the efficiency plateau of the asymmetric (symmetric) di-electron trigger if they have $p_T(e_1/e_2) > 25/10$ GeV ($p_T(e) > 15$ GeV). The asymmetric di-muon trigger chain is fully efficient for muons with $p_T(\mu_1/\mu_2) > 25/8$ GeV, while the di-muon symmetric trigger for muons with $p_T > 15$ GeV. In the electron-muon case, events are in the plateau of the $e\mu$ trigger if $p_T^e > 25$ GeV and $p_T^\mu > 10$ GeV or in the plateau of the μe trigger if $p_T^\mu > 20$ GeV and $p_T^e > 8$ GeV. Requirements on the p_T of the leading and sub-leading leptons are applied at analysis level according to the trigger thresholds, in order to avoid biases.

Single lepton chains with p_T thresholds of 25 GeV also contain requests on the lepton isolation. Triggers with the 'vh' label apply a cut on the hadronic core isolation ($\leq$1 GeV) at L1. The 'i' triggers apply a cut on track isolation at EF: $\sum p_T(\Delta R < 0.2) < 0.1 \times p_T$ for electrons and $\sum p_T(\Delta R < 0.2) < 0.12 \times p_T$ for muons. Isolation requirements are hence explicitly applied at the analysis selection level in order to avoid trigger biases.

The trigger efficiency for the selection criteria of the 8 TeV analysis, described in Section 3.6.2, exceeds 99%, 96% and 91% for ee, $e\mu$ and $\mu\mu$, respectively.

3.6 Object reconstruction and event selection

The reconstruction of the physics objects in this analysis follows the guidelines of Section 2.4.

The primary vertex of the event is reconstructed from the ID and is the vertex with the highest p_T^2 sum of the associated tracks. It is required to contain at least five tracks, in order to reduce the chance of selecting a cosmic event and to suppress

Single Electron	e24vhi_medium1 or e60_medium1
Single Muon	mu24i_tight or mu36_tight
Double Electron	e24vh_medium1_e7_medium1 or 2e12Tvh_loose1
Double Muon	mu24_tight_mu6_EFFS or EF_2mu13
Electron-Muon	EF_e12Tvh_medium1_mu8 or EF_mu18_tight_e7_medium1

Table 3.3: Trigger chains used in the analysis with $\sqrt{s} = 8$ TeV data. The numbers refer to the lepton p_T threshold imposed by the trigger. The 'vh' and 'i' labels indicate that the triggers contain hadronic and track isolations, respectively, as explained in the text. The 'loose', 'medium' and 'tight' labels refer to the object definitions described in Section 2.4.1. The 'tight' label for muon triggers is an index of the signature used at L1 and L2.

pile-up effects.

Jets are reconstructed using the anti-k$_t$ algorithm from the calorimeter energy clusters, with a radius parameter of 0.4. A jet candidate must have $p_T > 20$ GeV and $|\eta| < 2.5$. Jets with $20 < p_T < 50$ GeV and $|\eta| < 2.4$ are rejected if they have a value of the jet vertex fraction smaller than 0.5, in order to reject a large fraction of events coming from pile-up. This variable quantifies the fraction of the total momentum of the tracks associated to the jets which originates from the reconstructed primary vertex. Events must also pass jet quality criteria designed to reduce calorimeter noise and non-collision backgrounds, otherwise they are rejected.

Electron candidates (also called baseline) must have $p_T > 10$ GeV, $|\eta| < 2.47$ and must satisfy the 'medium' criteria described in Section 2.4.1. The candidates are then required to pass the 'tight' criteria and to be isolated. The isolation requirement asks that the scalar sum of the p_T of ID tracks with $p_T > 1$ GeV ($\sum p_T$), not including the electron track, and within a cone of radius $\Delta R < 0.2$ around the electron candidate, must be less than 10% of the electron p_T.

Muons are reconstructed with the STACO algorithm as combined muons. They must have hits in the pixel, strip and straw tube detectors, otherwise the candidate is rejected. Baseline muons are then required to have $p_T > 10$ GeV, $|\eta| < 2.4$ and must have longitudinal impact parameter $|z_0|$ within 1 mm and transverse impact parameter $|d_0|$ within 0.2 mm of the primary vertex, to reject candidates from cosmic rays. Signal muons are then required to have $\sum p_T < 1.8$ GeV, where $\sum p_T$ is defined in analogy with the electron case.

Overlaps between jets, electron and muon candidates are then solved following the reconstruction definitions described above. Jets at a distance $\Delta R < 0.2$ from preselected electrons are discarded. Electrons or muons within $\Delta R < 0.4$ from any remaining jet are rejected to reduce the contribution from the decay of $b-$ and $c-$hadrons.

The E_T^{miss} is finally measured using the transverse momenta of all remaining jets and lepton candidates after overlap removal and all the calorimeter clusters not associated to these objects.

After passing the trigger selections and the object reconstruction processes, events are required to have two opposite-sign (OS) leptons (e or μ). The leading lepton, i.e. the one with the highest transverse momentum, is required to have $p_T > 25$ GeV, in order to lay on the triggers efficiency plateau. The invariant mass of the two leptons

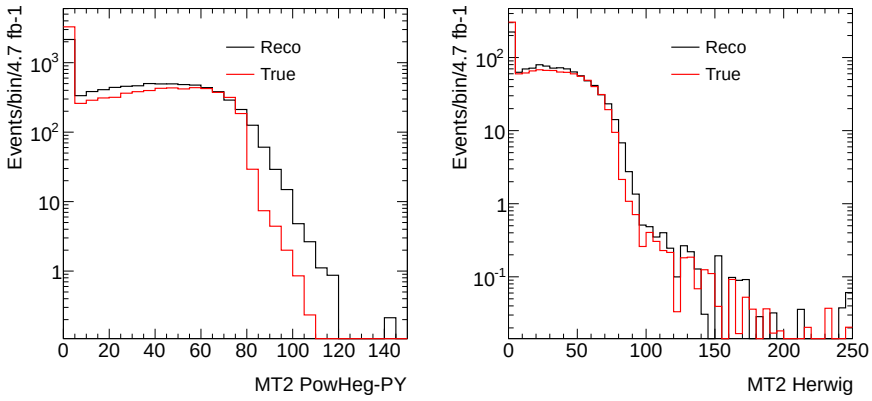

Figure 3.8: Distribution of m_{T2}^{ll} for top pairs (left) and WW (right) processes, obtained from MC simulation. The red line is the distribution at truth level, the black line at reconstruction level.

SR	SF	DF
leptons	opposite-sign same-flavor	opposite-sign different-flavor
m_{ll}	20< m_{ll} <71, m_{ll} >111 GeV	> 20 GeV
p_T leading lepton	> 25 GeV	
p_T leading jet	> 50 GeV	
p_T second jet	> 25 GeV	
n. $b-$jet	≥ 1	no selection
m_{T2}^{ll}	> 120 GeV	

Table 3.4: Signal Regions used in the analysis with $\sqrt{s} = 7$ TeV data.

is required to be greater than 20 GeV, to reduce the background contribution from Drell-Yan processes with low invariant mass values. Events with a third reconstructed lepton are discarded. Moreover, in order to reduce the contribution from SM processes with an on-shell Z boson decaying to two leptons, same-flavour events with an invariant mass lying in the window 71-111 GeV are rejected.

3.6.1 7 TeV Signal Regions

Two SRs are defined for the 7 TeV analysis, one with different-flavour events (DF) and the other with same-flavour events (SF). At least two jets with $p_T^{j1} > 50$ GeV and $p_T^{j2} > 25$ GeV are also required to suppress the WW and Z/γ^*+jets backgrounds. At least one of the jets of events passing the SF SR cuts must be $b-$tagged in order to suppress contributions from diboson processes. For this analysis, jets are considered $b-$tagged if they satisfy the 60% efficiency working point in the JetFitterCombNN algorithm. After these cuts, the dominant background source is given by $t\bar{t}$ production.

For both the SRs, signal candidates must have $m_{T2}^{ll} > 120$ GeV. This requirement suppresses the remaining background by several orders of magnitude and isolates the SUSY signal. The 120 GeV threshold has been chosen to optimize the sensitivity of the analysis. As can be seen from Fig. 3.8, in fact, the distribution of m_{T2}^{ll} at truth

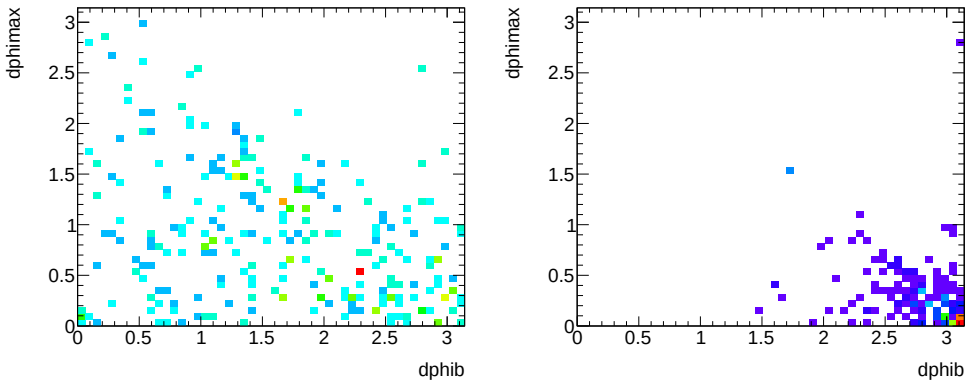

Figure 3.9: Distribution of the $\Delta\phi$ vs $\Delta\phi_b$ variables for top (left) and Z (right) events. Only events with $m_{T2}^{ll} > 90$ GeV are plotted

and reconstruction levels for the $t\bar{t}$ and WW processes sometimes extends beyond the kinematic edge driven by the W boson mass. WW production has a high m_{T2}^{ll} tail, which is mostly populated by events where one of the W is produced off-shell and thus has a greater mass value with respect to the nominal W mass. $t\bar{t}$ events, on the contrary, present a much sharper fall of the m_{T2}^{ll} distribution around the W mass, and high tails can be determined only by the finite experimental resolution. A cut at 120 GeV is sufficient to reject most of the two background sources at reconstruction level. Table 3.4 summarizes the selection cuts for the two SRs.

3.6.2 8 TeV Signal Regions

For the 8 TeV analysis, the selection cuts have been re-optimized for the $\tilde{t}_1 \to b\tilde{\chi}_1^{\pm}$ decay mode. Specific new pre-selections have also been studied to reduce the contamination from top pairs and Z/γ^*+jets backgrounds with significant contribution to E_T^{miss} coming from mis-measured jets. This additional contribution is expected to point towards the hadronic jets that are mis-measured and away from the vector sum of the leptonic activity in the event. Therefore, the following angular cuts are applied throughout the analysis:

- a cut on $\Delta\phi_b$, which is the azimuthal angle between the transverse missing energy vector $\vec{p}_T^{miss}$, whose magnitude is E_T^{miss}, and $\vec{p}_{Tb}^{ll} = \vec{p}_T^{miss} + \vec{p}_T^{l_1} + \vec{p}_T^{l_2}$, i.e. a measure of the transverse boost of the activity upstream of the lepton-lepton-E_T^{miss} system;

- a cut on $\Delta\phi$, which is the azimuthal angle difference between $\vec{p}_T^{miss}$ and the closest jet.

Fig. 3.9 shows the scatter plot of $\Delta\phi$ versus $\Delta\phi_b$ for events with $m_{T2}^{ll} > 90$ GeV, for $t\bar{t}$ and Z/γ^*+jets events. It can be seen from the figure that Z/γ^* events have a clear E_T^{miss} alignment, since the E_T^{miss} does not come from the presence of neutrinos, but has been originated from instrumental effects, while for top pairs the distribution widens due to the real contribution from neutrinos. The considerations expressed above led to the choice $\Delta\phi_b < 1.5$ and $\Delta\phi > 1$.

SR	M90	M100	M110	M120
p_T leading lepton	> 25 GeV			
$\Delta\phi(E_T^{miss}, \text{closest jet})$	> 1.0			
$\Delta\phi_b(E_T^{miss}, p_{Tb}^{ll})$	< 1.5			
m_{T2}^{ll}	> 90 GeV	> 100 GeV	> 110 GeV	> 120 GeV
p_T leading jet	no selection	> 100 GeV	> 20 GeV	no selection
p_T second jet	no selection	> 50 GeV	> 20 GeV	no selection

Table 3.5: Signal Regions used in the analysis with $\sqrt{s} = 8$ TeV data.

A study of the dependence of the final state kinematic on the $\tilde{t}_1$, $\tilde{\chi}_1^\pm$ and $\tilde{\chi}_1^0$ masses hierarchy has also been developed in the optimization phase of the analysis. Firstly, various cuts on m_{T2}^{ll}, from 90 to 120 GeV, have been tested for the SRs to account for signal models with different values of $m(\tilde{\chi}_1^\pm) - m(\tilde{\chi}_1^0)$ (the largest the mass splitting, the hardest the leptons produced in the decay). On the other hand, additional requests on the transverse momentum of the two leading jets have been studied to enhance the sensitivity to signal models with significant hadronic activity due to large values of $m(\tilde{t}_1) - m(\tilde{\chi}_1^\pm)$. A wide scan on the p_T of the two leading jets has been performed for each m_{T2}^{ll} cut and four optimal SRs have been finally chosen, as shown in Table 3.5. Moreover, no $b-$jets are explicitly asked for in this analysis, on the contrary of the 7 TeV case, since it was found that the gain in terms of sensitivity on most of the parameter space is negligible.

Among the SRs, M90 has the loosest selection on m_{T2}^{ll} and no additional requirements on jets. It provides the best sensitivity in a scenario with a small mass difference between the stop and the chargino, where the hadronic activity is expected to be soft. SRs M110 and M120 have a loose selections on jets ($p_T > 20$ GeV) and require m_{T2}^{ll} to be larger than 110 GeV and 120 GeV, respectively. These regions are sensitive to scenarios with moderate values of $m(\tilde{t}_1) - m(\tilde{\chi}_1^\pm)$. The last SR, M100, requires $m_{T2}^{ll} > 100$ GeV and has tighter cuts on the hadronic activity. This provides sensitivity to scenarios with large values of $m(\tilde{t}_1) - m(\tilde{\chi}_1^\pm)$ and $m(\tilde{\chi}_1^\pm) - m(\tilde{\chi}_1^0)$.

Fig. 3.10 shows the SR which gives the best expected sensitivity, and its corresponding value, for each mass hypothesis on the stop and chargino, for the scenario with $m(\tilde{\chi}_1^0) = 1$ GeV. The sensitivity is in this case expressed as $S/\sqrt{S + B + (\Delta B)^2}$, where S is the signal yield and B the SM background expectation taken from MC simulation. In the evaluation of the sensitivity, the background arising from fake leptons is measured from data, and the total uncertainty on all background sources has been chosen to be 30% of the background estimate ($\Delta B = 0.3 \times B$). A sensitivity value of $\sim$1.6 corresponds to a $p-$value of 0.05 on the signal plus background hypothesis, and thus excludes the model at 95% CL. In the figure, the observed exclusion limits from a previous ATLAS search with two leptons in the final state which used a partial set of the entire 8 TeV pp data (published in [144]), is superimposed for comparison. As can be seen from the figures, the SRs of this analysis give sensitivity to points of the parameter space which could not be reached by the previous search.

Fig. 3.11 shows the sensitivity as a function of the stop and neutralino masses for the scenario with a chargino mass $m(\tilde{\chi}_1^\pm) = m(\tilde{t}_1) - 10$ GeV.

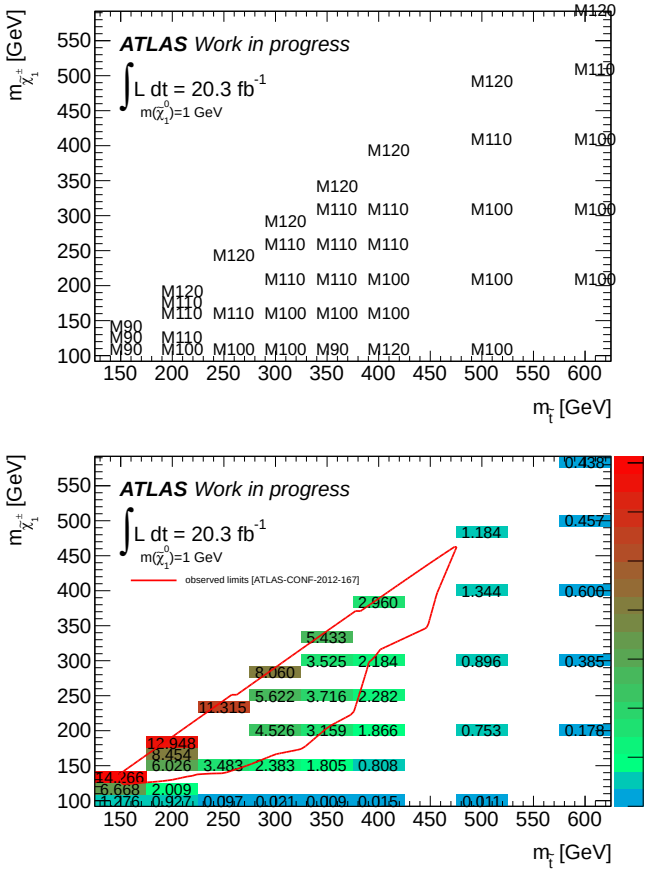

Figure 3.10: Best SR (top) and sensitivity $S/\sqrt{S+B+\Delta B^2}$ (bottom, with $\Delta B = 0.3B$) for a fixed neutralino mass of 1 GeV, assuming 20.3 fb^{-1} of 8 TeV data. The observed limits taken from Ref [144] are superimposed for comparison. A sensitivity around 1.6 corresponds to a $p-$value of 0.05 and thus excludes the point in the grid.

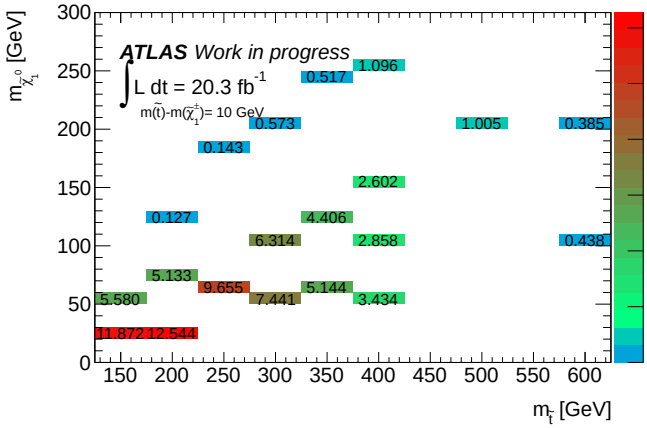

Figure 3.11: $S/\sqrt{S+B+\Delta B^2}$ (with $\Delta B = 0.3B$) for a chargino mass equal to the $\tilde{t}_1$ mass minus 10 GeV, assuming 20.3 fb^{-1} of data.

3.7 Uncertainties on the evaluation of SM background

Various sources of systematic uncertainty affecting the predictions of the SM background are considered both in the 7 TeV and 8 TeV analyses:

- **Jet Energy Scale (JES) and Resolution (JER)**: uncertainties are related to the measurement of the jet energy. The JES is derived using test beam results and in-situ measurements and varies as a function of the jet p_T and $|\eta|$. The JER is derived from a data-driven measurement in di-jet events. The parameters of the JES and JER uncertainties are varied by $\pm 1\sigma$ in the MC simulations and propagated to the event yield in the SR. They are also propagated to the E_T^{miss} measurement.

- **Electron**: uncertainties are due to reconstruction efficiency, energy scale and energy resolution. The former accounts for differences in the simulated reconstruction efficiency with respect to data, and includes both identification efficiency and reconstruction/track quality efficiency. The second is computed by scaling up and down the energy of the momentum of all selected electrons by its $\pm 1\sigma$ uncertainty and is thus an asymmetric source. The latter is obtained by rescaling the electron energy with a smearing procedure according to a Gaussian function with a p_T and η dependent sigma.

- **Muon**: uncertainties are due to reconstruction efficiency and momentum corrections. The reconstruction efficiency accounts, in analogy with the electron case, for differences in the simulated reconstructions with respect to data. The momentum corrections provide an asymmetric uncertainty which comes from varying the MS and ID components of the muon momentum estimate by their $\pm 1\sigma$ uncertainties.

- **Soft terms scale and resolution**: uncertainties are related to the energy scale and resolution of calorimeter cells not associated with electrons, muons and jets, and which contribute to the E_T^{miss} measurement in the CellOut term. Jets with low-momentum ($7 < p_T < 20$ GeV) also contribute to this source.

- **Pile-up**: events in simulations are weighted by a pile-up modeling function, which scales the average number of interactions per bunch crossing to match the one present in data. The uncertainty related to this procedure is evaluated by comparing the nominal results with those obtained by varying the modeling function by 10%.

- $b-$**tag efficiency and mis-tagging:** an uncertainty is evaluated by varying the $b-$tagging working point, i.e. the efficiency and mis-tagging rates, within the uncertainties measured from data. It only affects the 7 TeV results since no $b-$jets are required in the SRs of the 8 TeV case.

- **Limited MC sample size**: the statistical error coming from the available statistics of the simulation.

- **Trigger efficiency**: uncertainties are associated to the differences in the trigger efficiencies between MC and data. They are measured comparing the simulated events and real data in CRs with a Z boson decaying to two leptons. The

inefficiencies have been found to affect only the muon channel, and are of the order of 3%. They have been considered only for the 8 TeV analysis.

The sources listed above arise from experimental effects. Theoretical uncertainties have also been considered and they include:

- **Top pair production**: an uncertainty is associated to the choice of a specific MC generator. It is evaluated by comparing the predictions of $t\bar{t}$ yields from MC@NLO and POWHEG. Moreover, the difference in the predictions between POWHEG interfaced with PYTHIA and POWHEG interfaced with HERWIG is used to assess the uncertainty related to the description of the parton shower. Two other dedicated ACERMC samples are used the evaluate the uncertainty on the amount of simulated initial and final state QCD radiation (ISR and FSR), which can introduce additional gluon jets in the observed events.
- **Diboson production**: an uncertainty is evaluated by comparing the predictions from the MC generators SHERPA and ALPGEN, in the 7 TeV case, and SHERPA and POWHEG, in the 8 TeV case.
- Z**+jets production**: an uncertainty is evaluated by comparing the predictions from the MC generators SHERPA and ALPGEN, both for the 7 TeV and 8 TeV cases.
- **Luminosity**: a 2.8% error is assigned to the luminosity measurement. This value has been evaluated from luminosity calibration procedures using the ALPHA and LUCID detectors.
- **Cross sections**: uncertainties are related to the SM cross section theoretical calculations. They are listed in Table 3.7, both for $\sqrt{s} = 7$ TeV and $\sqrt{s} = 8$ TeV.

Physics process	σ [pb] 7 TeV	σ [pb] 8 TeV
$t\bar{t}$	167^{17}_{-18}	253^{+13}_{-15}
Wt	15.7 ± 1.2	22.4 ± 1.5
ZZ	6.2 ± 0.3	7.3 ± 0.4
WZ	19.1 ± 1.3	23.0 ± 1.6
WW	44.4 ± 2.8	54.6 ± 3.3

Table 3.6: Cross sections and their uncertainties for the most important SM background processes considered in the analyses presented in this thesis.

Uncertainties on the $t\bar{t}$ and diboson productions do not influence directly the background estimate in the SRs, since these processes are normalized to data in CRs. They do however contribute indirectly to the uncertainty on the normalization factors and on the MC predictions which are shown in the plots.

Systematic uncertainties are also taken into account for the expected signal yields. They include JES, JER, calorimeter energy scale, event pile-up, and b-tagging uncertainties (only for the 7 TeV case) discussed above. Moreover, additional uncertainties on the modeling of ISR and FSR have been introduced for the 8 TeV case. Theoretical uncertainties on the signal cross sections, together with variations on the choice of the factorization and renormalization scales, are also considered.

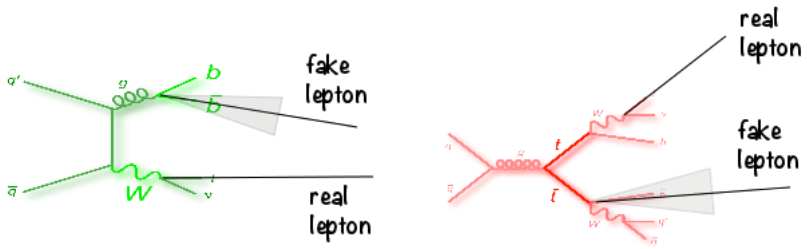

Figure 3.12: Production diagrams of events with one prompt lepton and one fake lepton, for W+jets production (left) and the semi-leptonic decay of a top pair (right). In both cases the fake lepton originates from a misidentified jet.

3.8 Background arising from fake leptons

In two-lepton final states, a non negligible source of background originates from events with two fake and non-prompt leptons, from light and heavy-flavour jet QCD production, or from events with one true and one fake lepton, typically from the semi-leptonic decay of $t\bar{t}$, single top and W+jets. Fake leptons can originate from jets which are misidentified as leptons. Examples of these sources are illustrated in the diagrams of Fig. 3.12. Photon conversions, in addition, contributes as a background source of fake leptons.

In order to estimate the background due to fake leptons the data-driven Matrix Method is used, both for the 7 TeV and 8 TeV analyses. It is based on a technique which extracts the number of expected events with real(R)-fake(F) and fake(F)-fake(F) leptons directly from the data-set by comparing the observed composition of the dilepton sample in terms of the two lepton selection criteria "tight" and "exclusively loose". Tight leptons pass all standard object selection requirements as described in Section 2.4. Exclusively loose leptons differ from tight leptons by failing isolation requirements.

The technique can be used for a generic two-lepton final states, but it depends on the measurement of two efficiencies, the fake rate f and the real efficiency r, which are a function of the selection criteria and must be re-determined every time the analysis cuts change. The fake rate f and the real efficiency r are defined as the probabilities that a fake or real loose lepton will pass the tight criteria.

If events containing exactly one lepton are used, these definitions translate in the following equations:

$$f = \frac{N_T^F}{N_L^F} \quad \text{and} \quad r = \frac{N_T^R}{N_L^R} \,, \tag{3.7}$$

where N refers to the number of events with one lepton fulfilling loose (L) or tight (T) requirements.

When considering two-lepton events, one has:

$$\begin{cases} N_{TT}^{RR} = N_{LL}^{RR} r_1 r_2 \\ N_{TT}^{RF} = N_{LL}^{RF} r_1 f_2 \\ N_{TT}^{FR} = N_{LL}^{FR} f_1 r_2 \\ N_{TT}^{FF} = N_{LL}^{FF} f_1 f_2 \end{cases} \tag{3.8}$$

where here N refers to the number of events with two leptons fulfilling loose (L) or

tight (T) requirements. It is understood that f and r depend on lepton properties such as p_T, η, etc., and therefore are labelled f_1/f_2 and r_1/r_2, accordingly.

The number of events with double-fake and fake-real tight leptons (N_{TT}^{FF} and $N_{TT}^{RF}+N_{TT}^{FR}$ respectively) can thus be obtained from the number of events with double-fake and fake-real loose leptons (N_{LL}^{FF} and $N_{LL}^{RF}+N_{LL}^{FR}$) once the fake rates f_i and efficiencies r_i are known. In turn, N_{TT}^{FF}, N_{TT}^{FR} and N_{TT}^{RF} can be obtained by inverting the matrix M:

$$\begin{pmatrix} N_{TT} \\ N_{Tl} \\ N_{lT} \\ N_{ll} \end{pmatrix} = M \begin{pmatrix} N_{LL}^{RR} \\ N_{LL}^{RF} \\ N_{LL}^{FR} \\ N_{LL}^{FF} \end{pmatrix} \tag{3.9}$$

where l stands for exclusively loose and the notation N_{lT} or N_{Tl} translates into ordered lepton pairs. In the equation above, the matrix M is defined as:

$$M = \begin{pmatrix} r_1 r_2 & r_1 f_2 & f_1 r_2 & f_1 f_2 \\ r_1(1-r_2) & r_1(1-f_2) & f_1(1-r_2) & f_1(1-f_2) \\ (1-r_1)r_2 & (1-r_1)f_2 & (1-f_1)r_2 & (1-f_1)f_2 \\ (1-r_1)(1-r_2) & (1-r_1)(1-f_2) & (1-f_1)(1-r_2) & (1-f_1)(1-f_2) \end{pmatrix} \tag{3.10}$$

One can thus extract the contribution due to double-fake and fake-real events in the SR (N_{TT}^{FF} and $N_{TT}^{FR}+N_{TT}^{RF}$) from the observable quantities N_{TT}, N_{Tl}, N_{lT} and N_{ll}.

The measurement of the f and r efficiencies, however, is of crucial importance for the estimate of the fakes background. It usually occurs in suitable CRs: f can be evaluated in QCD-enriched CRs, typically characterized by low missing transverse energy and moderate jet activity, while r can be measured in events with two prompt leptons from the Z boson decay. In order to reduce biases and provide a reliable estimate, CRs alike the SR have to be considered, and a good parametrization of the efficiencies on the event kinematic must be considered. Once they are known, the Matrix Method can be applied at the desired selection level and the estimate is obtained.

The procedure through which the two efficiencies are measured for the 7 TeV and 8 Tev analyses and the results of the Matrix Method in their SRs are presented in Chapters 4 and 5, respectively.

4

Results of the search using 4.7 fb^{-1} of data at $\sqrt{s} = 7$ TeV

This Chapter presents the result of the search using 4.7 fb^{-1} of data at $\sqrt{s} = 7$ TeV. More emphasis is placed on the estimate of the background arising from fake leptons, since this has been part of my work. Results are shown for a simplified model with stop pair production and each stop decaying to a top quark and a neutralino with 100% BR. No excess over the SM predictions has been found and exclusion limits are set on the parameters of the model. This analysis has been already published on the JHEP journal [145].

4.1 Introduction

This Chapter presents the results from the search for pair production of stop in ATLAS using events with two leptons in the final state at a center of mass energy of 7 TeV. The analysis is optimized to have maximal sensitivity for a simplified model which considers the $\tilde{t}_1 \to t\tilde{\chi}_1^0$ decay. The two-lepton channel is obtained when each of the top quarks decays to a W boson and a bottom quark and the W bosons subsequently decay to a lepton and a neutrino. This happens only in in 4.9% of the cases, as already said, considering the BR of the top quark leptonic decay in both legs. The channel is sensitive to cases with moderate or large mass splitting between the stop and the neutralino, although it is limited at high stop masses by the signal cross section.

The m_{T2}^{ll} variable is used to discriminate the signal from the SM background, and additional requests on the presence of ($b-$)jets have been found to increase the sensitivity of the search. The analysis strategy, the event selections and the MC and data samples utilized in this analysis have already been discussed in Chapter 3. In this Chapter, the results of the search are presented. Section 4.2 describes the general approach used to estimate the SM background, while Section 4.3 describes in details the estimate of the background arising from fake leptons. Section 4.4 finally illustrates the outcomes of the search.

4.2 SM background estimate

The dominant SM background contributions in the SRs arise from $t\bar{t}$ production and Z/γ^*+jet events, the latter contributing only to the SF SR. Each of these sources is measured in a dedicated CR and extrapolated to the SR by means of a transfer factor:

$$N_{SR} = (N_{CR}^{data} - N_{CR}^{other}) \frac{N_{SR}^{MC}}{N_{CR}^{MC}} \ , \tag{4.1}$$

where N_{SR} is the expected rate of the targeted background process in the SR, N_{CR}^{data} is the observed number of events from data in the CR, N_{CR}^{other} is the MC predicted rate of all SM background processes except the targeted one in the CR, while N_{SR}^{MC} and N_{CR}^{MC} are the predicted number of events from MC of the targeted process in the SR and CR. Finally, the rate N_{SR}^{MC}/N_{CR}^{MC} is the transfer factor.

The estimate relies on a good choice of the CRs, which should be mostly populated by the targeted process. If this is the case, the $(N_{CR}^{data} - N_{CR}^{other})$ term allows to predict from the data the background yields in the CR, and the transfer factor propagates the prediction to the SR.

The $t\bar{t}$ CR is defined as the SR, except for the m_{T2}^{ll} cut, which is required to lie between 85 GeV and 100 GeV. This region is expected to be populated by top pairs with a purity of 84% for SF events and 94% for DF events. The non-top background is measured in the CR using the simulations, with the exception of the fake leptons background which is measured with a data-driven technique, described in Section 4.3. The composition of the $t\bar{t}$ CR, with the observed number of events from data and the MC predictions, is shown in Table 4.2. Good agreement between data and the background yields is found.

The CR for Z/γ^*+jets is defined applying the same selections of the SF SR, but with the invariant mass veto reversed. The observed number of events in the CR is found to be 11, compared to an expectation of 7.6±1.1, where the quoted uncertainties include the statistical and systematic ones. The transfer factor for Z/γ^*+jet events is measured releasing the $b-$tagging requirement, in order to cope with the limitations due to statistical fluctuations. Of course, the transfer factor has been tested to be stable against the $b-$tag requirement. Z/γ^*+jet events with the Z decaying to $\tau\tau$ have a negligible effect on the measurements, and also the DF channel has been found to be not affected by this background source, independently from the Z decay.

Additional minor SM processes generating two isolated leptons and E_T^{miss}, such as Wt, WW, WZ, ZZ, $t\bar{t}W$ and $t\bar{t}Z$ are measured in the SR from MC simulation. The composition of the various background sources in the SRs, together with the number of observed events from data, is provided later in the Chapter in Table 4.10.

Process	DF rate in CR	SF rate in CR
$t\bar{t}$	68.1 ± 11.4	39.0 ± 11.2
$t\bar{t}W$,$t\bar{t}Z$	0.33 ± 0.09	0.17 ± 0.06
single top	2.7 ± 1.0	1.8 ± 0.5
Z+jets	-	3.5 ± 1.4
Fakes	0.4 ± 0.3	0.5 ± 1.6
Diboson	0.49 ± 0.27	0.11 ± 0.10
Total non-$t\bar{t}$	3.9 ± 1.6	6.1 ± 3.7
Total Expected	72 ± 11	45 ± 12
Data	79	53

Table 4.1: Top CR composition for 4.7 fb^{-1}. The quoted uncertainties include both statistical and systematic uncertainties.

4.3 Estimate of the fake leptons background

4.3.1 Fake rate

The fake rate for the 7 TeV analysis is measured in QCD-enriched CRs. This is achieved by requiring a high jet multiplicity and low E_T^{miss} in the event, with either one single lepton or two same-sign (SS) DF leptons. In both cases, the regions are expected to be dominated by the QCD multijet background, with one or two non-prompt leptons, respectively. Multiple CRs with the requirements described above, and summarized in Table 4.2 and Table 4.3, have been tested.

The fake rate in the one-lepton regions is measured as the ratio:

$$f = \frac{N_T}{N_L} \ , \tag{4.2}$$

where N_T is the number of events with one tight lepton (T) and N_L is the number of events with one loose lepton (L).

In the two-lepton regions, an anti-tag&probe method is used to enhance the contribution from events with fake leptons: one of the two leptons in the event is tagged to be exclusively loose (l), i.e. loose and not tight, and the other is probed against tight requirements. Therefore the fake rate is determined as:

$$f = \frac{N_{lT}}{N_{lL}} \ . \tag{4.3}$$

For each CR, the contamination of events with prompt (real) leptons originating from SM background such as W+jets, Z+jets, top pairs, single top and dibosons, which will naturally contribute to a higher fake rate, have been evaluated using the MC simulation and subtracted to the number of observed events in data. Then the purity of the QCD composition after the MC subtraction is defined as the ratio between the expected QCD events and the quantity observed in the data. This can be written as:

$$Purity = \frac{N_{data} - N_{MC}}{N_{data}} \approx \frac{N_{QCD}}{N_{data}} \tag{4.4}$$

where all MC samples have been normalized to the integrated luminosity of data.

In the 2LCR3 of Table 4.3 the anti-tag request has been removed. This results in a sample with higher statistics but slightly worsens the purity of the sample, due to a little contamination from prompt leptons which are expected to pass the tight selections. In this region, the fake rate in the electron (muon) channel is measured by tagging the muon (electron) and probing the electron (muon) against tight requirement.

Despite several CRs were studied, the final estimate of the fake rate comes from a weighted average of 1LCR1 and 2LCR2, which guarantee a good similarity with the two-lepton final state of the SRs, and present the best compromise between statistics and purity.

The contribution from conversions, which - as non-prompt leptons - are sources of fakes, is naturally included in this estimate. A study of this contribution was performed by adding a hit requirement in the innermost layer of the Pixel Detector for all the

CR(e)	Cuts	N(L)	N(T)	Purity
1LCR1	$E_T^{miss} < 25$, $n_j \geq 2$, $\Delta\phi_{l\nu} < 0.5$	2.0×10^6	0.5×10^6	0.98
1LCR2	$E_T^{miss} < 25$, $n_j \geq 1$, $\Delta\phi_{l\nu} < 0.5$	8.5×10^6	2.0×10^6	0.97
1LCR3	$E_T^{miss} < 40$, $n_j \geq 1$, $\Delta\phi_{l\nu} < 0.5$	1.1×10^7	2.7×10^6	0.96
CR(μ)	Cuts	N(L)	N(T)	Purity
1LCR1	$E_T^{miss} < 25$, $n_j \geq 2$, $\Delta\phi_{l\nu} < 0.5$	9.9×10^5	3.8×10^5	0.97
1LCR2	$E_T^{miss} < 25$, $n_j \geq 1$, $\Delta\phi_{l\nu} < 0.5$	4.8×10^6	1.9×10^6	0.97
1LCR3	$E_T^{miss} < 40$, $n_j \geq 1$, $\Delta\phi_{l\nu} < 0.5$	6.3×10^6	2.5×10^6	0.97

Table 4.2: One-lepton QCD-enriched CRs used to measure the fake rate: definition, number of events with (exactly) one loose lepton N_L, number of events with (exactly) one tight lepton N_T and purity of the sample.

CR(μe)	Cuts	N(lL)	N(lT)	Purity
2LCR1	same-sign, anti-tag, $E_T^{miss} < 25$	2.5×10^4	0.6×10^4	0.98
2LCR2	same-sign, anti-tag, $E_T^{miss} < 25$, $N_{jets} > 0$	1.8×10^4	0.4×10^4	0.99
2LCR3	same-sign, $E_T^{miss} < 25$	4.6×10^4	1.2×10^4	0.96
CR($e\mu$)	Cuts	N(lL)	N(lT)	Purity
2LCR1	same-sign, anti-tag, $E_T^{miss} < 25$	3.4×10^4	1.5×10^4	0.96
2LCR2	same-sign, anti-tag, $E_T^{miss} < 25$, $N_{jets} > 0$	2.3×10^4	1.0×10^4	0.97
2LCR3	same-sign, $E_T^{miss} < 25$	4.6×10^4	2.1×10^4	0.95

Table 4.3: Two-lepton QCD-enriched CRs used to measure the fake rate: number of events with one loose and one exclusively loose leptons N_{lL}, number of events with one exclusively loose and one tight lepton N_{lT} and purity of the sample. In the 2LCR3 sample, the exclusivity of the loose tagged lepton is removed by dropping the anti-tag requirement.

loose electrons, which removes most conversions: as a consequence, the agreement between predictions and data was observed to worsen, showing that the contribution from conversions is indeed folded in the method outlined before.

Another component that is expected to have an effect on the fake rate estimate is the heavy-flavor content of the CR as compared to the SR. This has been taken into account by measuring for each CR two different fake rates: one without the $b-$jet requirement, to be used in the pre-tag scenarios, and one with the $b-$jet requirement, to be used for predictions in the SF SR where a $b-$jet is explicitly required.

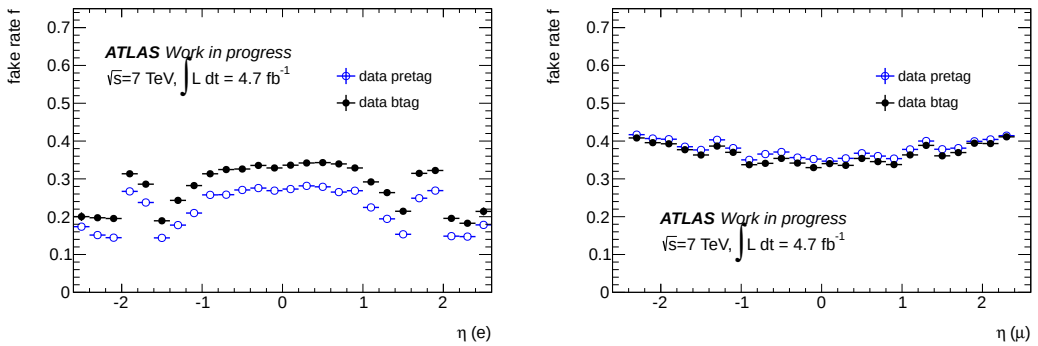

Figure 4.1: Fake rate versus the electron η (left) and muon η (right), in the pre-tag and $b-$tag samples. A combination of 1LCR1 and 2LCR2 is used, as described in the text.

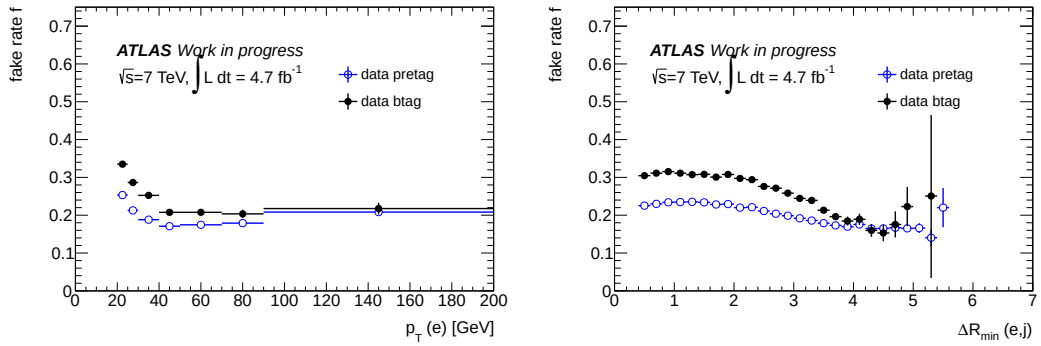

Figure 4.2: Fake rate versus the electron p_T (left) and ΔR_{ej}^{min} (right), in the pre-tag and $b-$tag samples. A combination of 1LCR1 and 2LCR2 is used, as described in the text.

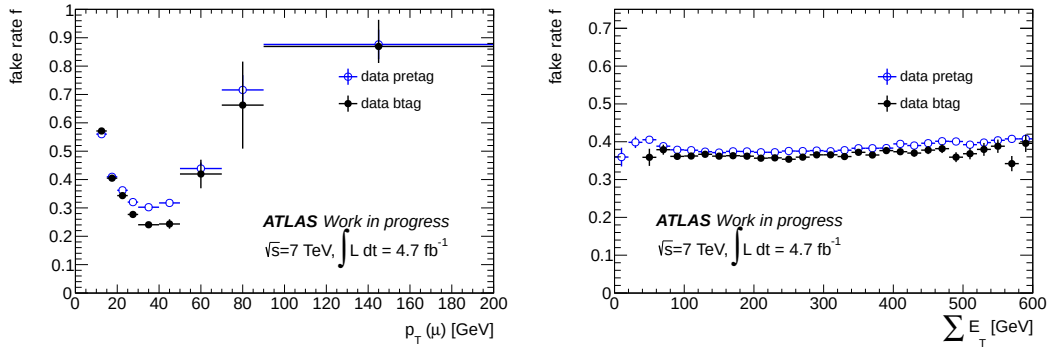

Figure 4.3: Fake rate versus the muon p_T (left) and the $\sum E_T$ of the event (right), in the muon channel, in the pre-tag and $b-$tag samples. A combination of 1LCR1 and 2LCR2 is used, as described in the text.

Figures 4.1, 4.2 and 4.3 summarize the results obtained separately for electrons and muons. As expected, the f value is not constant in general but depends on lepton quantities (η, p_T) and on the isolation (ΔR_{lj}^{min}) as well as on global variables such as $\sum E_T$. In order to retain statistical power of the estimate, a bin-by-bin parameterization on the fake rate has been performed in the lepton η only; any residual dependance (p_T and ΔR_{ej}^{min} for electrons, p_T and $\sum E_T$ for muons) has been taken into account by a suitable parameterization. This can be expressed as:

$$f(\eta, p_T, ...) = f'(\eta) \prod_{i=p_T,...} \frac{f''(i)}{< f >} \tag{4.5}$$

where $< f >$ is the average fake rate of the two control regions 1LCR1 and 2LCR2 independently from any parameterization.

The parameterization of the muon fake rate as a function of the muon p_T is however not valid anymore for $p_T > 40$ GeV, due to a non negligible contamination from prompt muons after that threshold. Figures 4.4 shows the composition of the QCD-enriched 1LCR sample in the muon channel, both for loose and tight sample. Generally, there is a large observed difference between data and MC simulation due to the presence of fake leptons in data, which guarantee a high purity of the sample. However, in the

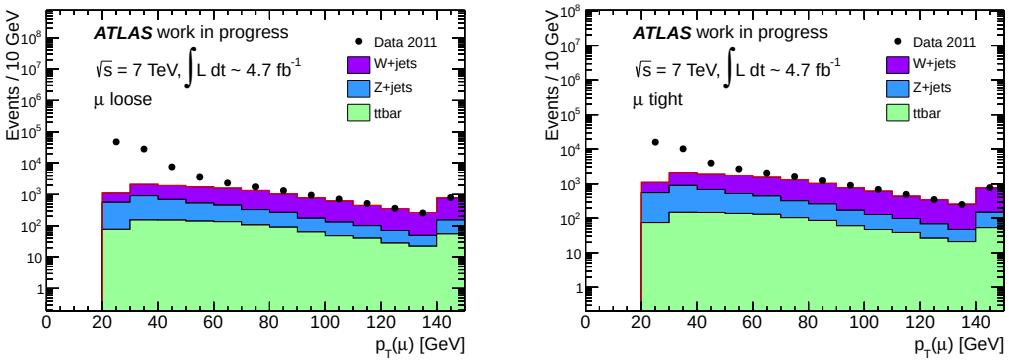

Figure 4.4: Data/MC comparison for the 1LCR sample requiring one loose (left) or tight (right) muon. The large observed discrepancy is due to fake leptons.

high muon p_T bins, the purity of the QCD sample worsens due to contamination from prompt and real leptons, and the estimate of the fake rate is contaminated, although a MC subtraction is applied. After having checked from MC that the fake rate has a flat distribution above 40 GeV, it has been therefore decided to apply the fake rate from the bin before 40 GeV also for muons with $p_T > 40$ GeV.

4.3.2 Real efficiency

The real efficiency is extracted from a highly pure sample of Z boson events. This is achieved by requiring two OS loose leptons with same flavor whose invariant mass lies in the range 86-96 GeV. The real efficiency is then estimated with a tag&probe method: one of the two leptons is required to pass tight criteria, the other one is then probed for tight selection cuts. Consequently, r turns out to be:

$$r = \frac{N_{TT}}{N_{TL}} \ . \tag{4.6}$$

The efficiencies in the electron and muon channels are shown in Fig. 4.5 and Fig. 4.6. The dominant effects come from the lepton η and p_T, while other additional dependences are negligible: r is thus measured bin per bin in η and parametrized with respect to the p_T of the lepton.

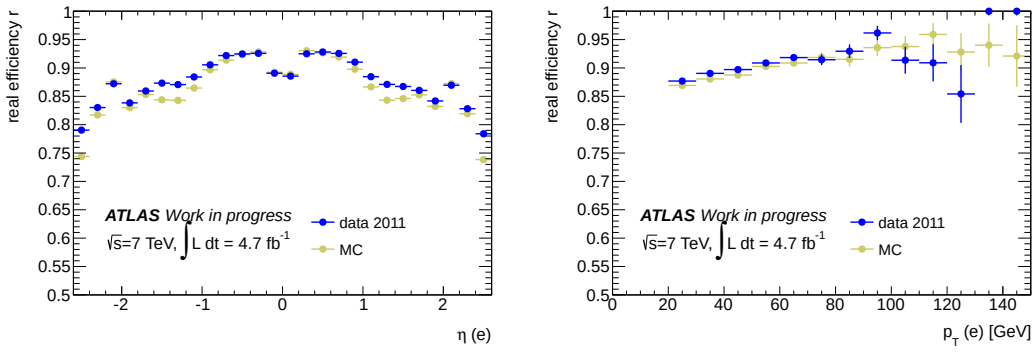

Figure 4.5: Comparison of the real efficiency from MC and data, as a function of the η (left) and p_T (right) of the electron.

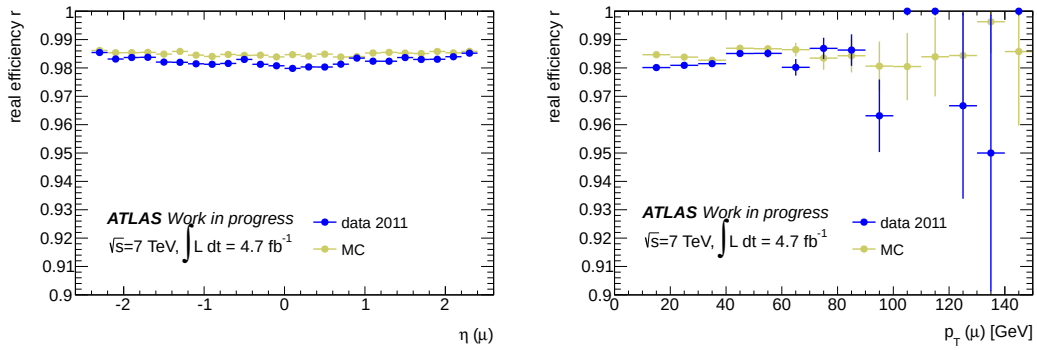

Figure 4.6: Comparison of the real efficiency from MC simulation and data, as a function of the muon η (left) and p_T (right).

4.3.3 Signal Region predictions

The final estimate of fake events in the SR can be obtained by applying the Matrix Method directly on the events which survive to the SR cuts. Table 4.4 shows the results.

	SF Est. fake	DF Est. fake
OS-SR	-0.06±0.06(stat.)±0.02(syst.)	0.49±0.54(stat.)±0.06(syst.)

Table 4.4: Estimated fake contribution in the SF and DF SRs using the Matrix Method.

The estimate in this case relies on the number of events observed from data in the SR, which, for this analysis, is very small: the m_{T2}^{ll} cut ($m_{T2}^{ll} > 120\,\text{GeV}$) is in fact so selective that only one (two) event survives in the SF (DF) SR, leading to a very high statistical error and suffering from a possible signal contamination. To cope with these problem, an additional approach has been studied.

4.3.4 Extrapolation to the Signal Regions

To solve the low statistics problem in the SRs, an additional approach has been studied to measure the fake background in suitable CRs and project the contribution in the SR by means of transfer factors.

In the SF channel, the number of events in the SR is estimated by means of the Matrix Method after dropping the explicit Z-veto requirement; the effect of the Z-veto is introduced a posteriori as a scaling factor measured before the m_{T2}^{ll} requirement:

$$N_{fakes}^{SR} = N_{fakes}^{SRZ} \times \frac{N_{fakes}^{SF}}{N_{fakes}^{SFZ}} \,, \tag{4.7}$$

where N_{fakes}^{SRZ} is the Matrix Method prediction in the SF SR after releasing the Z-veto, N_{fakes}^{SF} is the prediction in the SF SR after releasing the m_{T2}^{ll} cut, and N_{fakes}^{SFZ} after releasing both the Z-veto and the m_{T2}^{ll} cut. Results of this procedure are summarized in Table 4.5.

	SF Est. fake
OS-SR	-0.20±0.11(stat.)±0.09(syst.)

Table 4.5: Estimated fake leptons contribution obtained by projection into the SR in the SF channel.

The DF channel suffers from lower statistics, and need to be handled in a different way. The SR is defined by cuts applied on m_{T2}^{ll} and on the number of jets; however, this last requirement cannot be relaxed below one in order to avoid the bias induced by the L1 lepton+jet trigger primitive used for the latest period of data taking. Moreover, no events are observed in data with $m_{T2}^{ll} > 120$ GeV and only one jet (the p_T of which must exceed 50 GeV in order to be in the trigger plateau). For this reason an extrapolation procedure (a.k.a. ABCD method) has been implemented on the basis of m_{T2}^{ll} and the p_T of the subleading jet.

Four mutually exclusive regions have been defined as follows:

- A: $m_{T2}^{ll} < 120$ Gev and $p_T^{sub-j} > 25$ GeV;
- B: $m_{T2}^{ll} > 120$ GeV and $p_T^{sub-j} > 25$ GeV. This corresponds to the SF SR;
- C: $m_{T2}^{ll} < 120$ GeV and $p_T^{sub-j} < 25$ GeV;
- D: $m_{T2}^{ll} > 120$ GeV and $p_T^{sub-j} < 25$ GeV.

The number of fake events in the SR is then predicted from the following formula:

$$N_{SR}^{fakes} = N_B = N_D \times \frac{N_A}{N_C} \ , \tag{4.8}$$

while the number of fake events in regions A,C and D is estimated using the Matrix Method, and is listed in table 4.6. The result of the ABCD extrapolation procedure in the DF SR is summarized in Table 4.7.

Region	Fakes
A	421.8±20.6
C	51.9±7.5
D	-0.01±0.01

Table 4.6: Number of estimated events with fake leptons in region A, C and D for the DF channel. The quoted errors are only statistical.

	DF Est. fake
OS-SR	-0.08±0.08(stat.)±0.03(syst.)

Table 4.7: Estimated contribution due to fake leptons obtained by projection into the SR in the DF channel.

It can be seen that the results obtained by projections into the SR are compatible with the results of the Matrix Method itself (Table 4.4); however, being affected by smaller uncertainties, these are considered as the best estimates. In the following both extrapolation methods are called ABCD method for simplicity.

4.3.5 Uncertainties on the fakes predictions

To evaluate the systematic uncertainties on the final estimate of fake leptons, several sources of errors have been considered and measured, the results of which are listed in Table 4.8.

Two effects contribute to the systematic uncertainty affecting the determination of the fake rate f: the limited statistics of the CRs and the discrepancy between values of f estimated from different CRs. In this case, if the discrepancy is statistically relevant, a systematic uncertainty is attributed to the best value of f (i.e. the weighted average of the values measured in different CRs) to account for a larger-than-expected spread of the single measurements around their central value. The combination of this two errors is listed in Table 4.8 under the label f CR sys.

Other sources of systematic uncertainty have been investigated within the Matrix Method. The first one enters the definition of the CRs, namely through the E_T^{miss} cut, the nominal value of which has been varied by an amount equal to the detector resolution (taken to be 5 GeV for this case). The second source is induced by the MC correction applied to data in order to reduce the contamination due to real leptons when using QCD-enriched CRs. In this case a $\pm 25\%$ uncertainty is assigned to the predicted cross section (as for the W+jets process). A third source keeps into account the differences between data and MC and is evaluated by computing the real efficiency directly on MC and by comparing the result with what is obtained from data.

A further contribution to the systematic uncertainty originates from the extrapolation procedure (the ABCD method) that has been used to predict the contribution of fake leptons to the total background in the SR. The highest observed discrepancy between the extrapolation and the direct Matrix Method prediction in the validation regions (30%) is assumed as a systematic error (see Table 4.9).

The total systematic uncertainty is then computed by considering each source as independent and by summing in quadrature their values.

Systematic	SF (%)	DF (%)
f CR sys.	32.6	24.6
E_T^{miss} cut	1.3	0.4
MC scaled	1.3	3.4
r from MC	12.4	1.5
ABCD met.	30.0	30.0
Total	46.0	39.0

Table 4.8: List of systematic uncertainties for the fakes estimate method used in the 7 TeV analysis.

	$5 < m_{T2}^{ll} < 70$	$15 < m_{T2}^{ll} < 70$	$25 < m_{T2}^{ll} < 70$
MM (DF)	229.6 ± 15.3	150.4 ± 12.7	99.1 ± 11.1
MM+ABCD (DF)	232.6 ± 65.7	160.5 ± 45.3	95.6 ± 31.1
MM (SF)	82.7 ± 11.9	65.0 ± 10.7	40.3 ± 8.9
MM+ABCD (SF)	77.9 ± 15.6	58.0 ± 12.7	36.6 ± 9.4
	$35 < m_{T2}^{ll} < 95$	$70 < m_{T2}^{ll} < 90$	$90 < m_{T2}^{ll} < 120$
MM (OF)	58.9 ± 9.1	6.8 ± 6.4	0.3 ± 0.5
MM+ABCD (OF)	52.8 ± 23.7	9.6 ± 8.4	0.2 ± 0.2
MM (SF)	27.0 ± 7.9	1.1 ± 2.3	0.7 ± 0.6
MM+ABCD (SF)	20.4 ± 7.3	0.8 ± 2.1	0.4 ± 0.3

Table 4.9: Comparison between the number of estimated fake events after all SR cuts but at different values of m_{T2}^{ll} using the Matrix Method (MM) and the Matrix Method plus ABCD (MM+ABCD) for SF and DF channels. All m_{T2}^{ll} values are in GeV. Error is only statistical.

4.3.6 Validation of the fakes predictions

The Matrix Method is validated using a CR with two SS signal leptons before and after applying all cuts (but without the $m_{T2}^{ll} > 120$ GeV requirement). In these regions, most of the SM background is expected to come from fake leptons and minor contributions from Z+jets and dibosons. An extra small contribution is expected from the $t\bar{t}$ undergoing charge flip process. This is taken into account by adding $t\bar{t}$ production from MC simulation where all leptons are matched at truth level. Two examples of these validation plots are reported in Fig. 4.7 and Fig. 4.8. The former shows the dilepton invariant mass distribution of the two signal leptons before the analysis cuts, while the latter shows the missing transverse energy distribution after applying all cuts (except m_{T2}^{ll}). All the errors in the figures are only statistical, since they are expected to dominate. An overall good agreement is observed between data and the fake estimate in all channels. The only relevant discrepancy, in the 80-100 GeV bin of Fig. 4.8, is due to events with a large jet multiplicity which are not perfectly parameterized. The effect is however confined and no further actions have been taken.

The validation of the extrapolation procedure is performed by comparing its performance in some CRs with the prediction obtained directly from the Matrix Method. The comparison was carried over in regions with large statistics and where the Matrix Method was validated. For this reason, regions with all analysis cuts except for m_{T2}^{ll} have been considered, as listed in Table 4.9. Only statistical errors are considered for this validation. As one can see from the table, in the DF channel this error is much higher for the extrapolation procedure than for the Matrix Method. This is due to the fact that the ABCD method uses a very narrow window for the p_T of the subleading jet. However, at high m_{T2}^{ll} values (i.e. approaching the SR), this difference turns out to be the opposite and the statistics on which performing the extrapolation procedure is similar or even better than that used in the Matrix Method itself.

By looking at Table 4.9, a good compatibility can be observed in all the regions within the errors. The highest overall discrepancy between the nominal values of the different methods, which is of the order of 30%, is however taken as a systematic uncertainty for the final estimate.

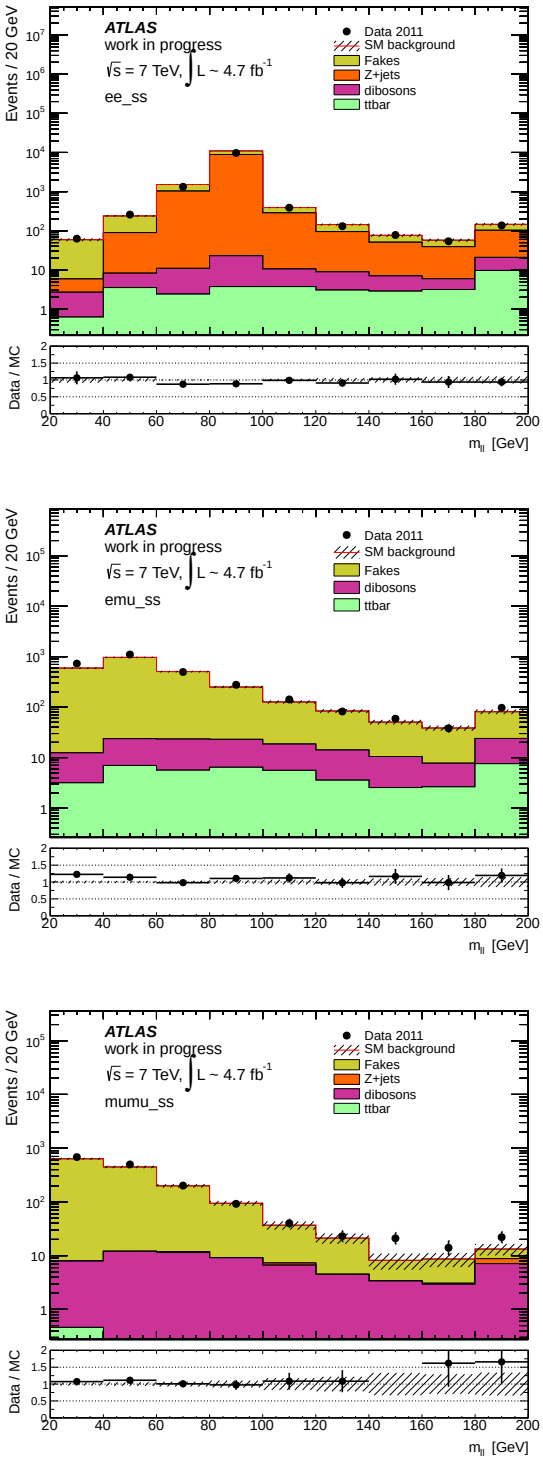

Figure 4.7: Invariant mass distribution of dilepton events (ee, $e\mu$ and $\mu\mu$) in the fakes validation region after the two same sign signal leptons requirement. The shown uncertainty is only statistical.

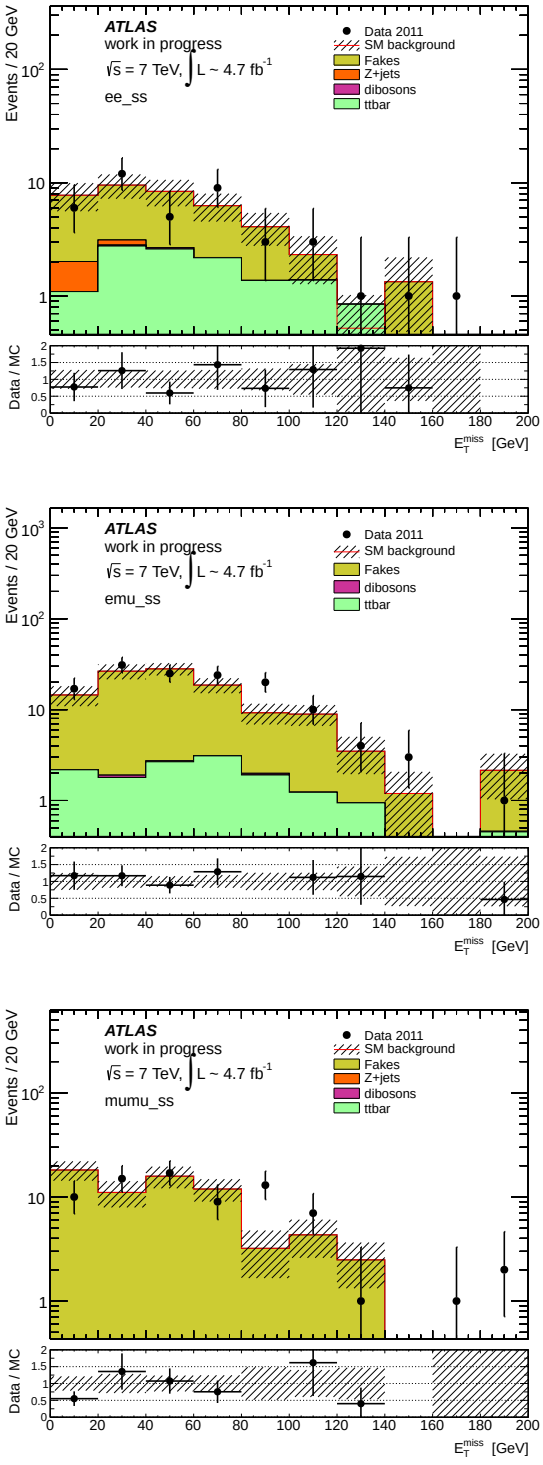

Figure 4.8: Missing transverse energy distribution of same sign dilepton events (ee, $e\mu$ and $\mu\mu$) in the fakes validation region after applying all cuts before m_{T2}^{ll}. The shown uncertainty is only statistical.

	SF	DF
Observed	1	2
Expected	$1.58^{+0.63}_{-0.59}$	0.94 ± 0.60
$t\bar{t}$	$0.23^{+0.24}_{-0.23}$	$0.43^{+0.48}_{-0.43}$
$t\bar{t}W$	0.06 ± 0.04	0.11 ± 0.08
$t\bar{t}Z$	0.05 ± 0.04	0.08 ± 0.05
Wt	$0.00^{+0.19}_{-0.10}$	$0.10^{+0.19}_{-0.10}$
Z+jets	1.17 ± 0.49	0.00 ± 0.00
WW	$0.01^{+0.02}_{-0.01}$	0.19 ± 0.18
WZ	0.03 ± 0.03	0.03 ± 0.03
ZZ	0.02 ± 0.02	$0.00^{+0.03}_{-0.00}$
fakes	$0.00^{+0.14}_{-0.00}$	$0.00^{+0.09}_{-0.00}$

Table 4.10: Observed and expected number of events in the SF and DF SRs. The breakdown of the background processes in the individual components is also reported. Negative values in the fakes predictions are indicate with zeroes.

4.4 Results

By using the procedures described so far, the total number of expected SM events in the two SRs is measured, as shown in Table 4.10. The SM background yields are evaluated with the method described in Section 4.2, while the background from fake leptons has been measured as described in Section 4.3. Statistical and systematic uncertainties are computed in the rates, the latter including all the sources listed in Section 3.7.

Fig. 4.9 shows the distribution of the m_{T2}^{ll} variable in the SF and DF SRs. Data points agree with the SM background expectation within the uncertainties. No excess of events is observed, and thus the rates in the SRs are firstly used to extract limits at 95% CL on the model independent visible cross section of new physics: $\sigma_{vis} = \sigma \times \epsilon \times \mathcal{A}$. Here σ refers to the total production cross section for any new physics, ϵ is the detector efficiency (including reconstruction, identification and trigger efficiencies) and $\mathcal{A}$ is the acceptance defined as the fraction of events passing the geometric and kinematic selections at particle level. The results are listed in Table 4.11.

Model dependent limits have also been derived on the simplified model $\tilde{t}_1 \to t\tilde{\chi}_1^0$, where each stop decays to a top quark and a neutralino with 100% BR. The limits are set on the $m(\tilde{t}_1) - m(\tilde{\chi}_1^0)$ plane, and are shown in Fig. 4.10. In this case, a statistical combination of the SF and DF SRs is used. Experimental uncertainties are considered in the signal samples, while limits are re-evaluated and shown separately for the $\pm 1\sigma$ variation on the theoretical uncertainties of the SUSY model. To calculate these limits, the CL_s likelihood ratio prescriptions described in [146] have been followed. The systematic uncertainties have been included in the likelihood as nuisance parameters described by a gaussian probability density function.

In conclusion, a stop below 300 GeV is excluded at 95% CL for a nearly massless neutralino[1].

[1]The limit is cited for the -1σ variation on the theoretical uncertainties of the signal model.

	SF	DF
95% CL limit on σ_{vis}^{obs}	0.86	1.08
95% CL limit on σ_{vis}^{exp}	0.89	0.79

Table 4.11: Model independent limits on the visible cross section σ_{vis}. Both observed and expected values are reported.

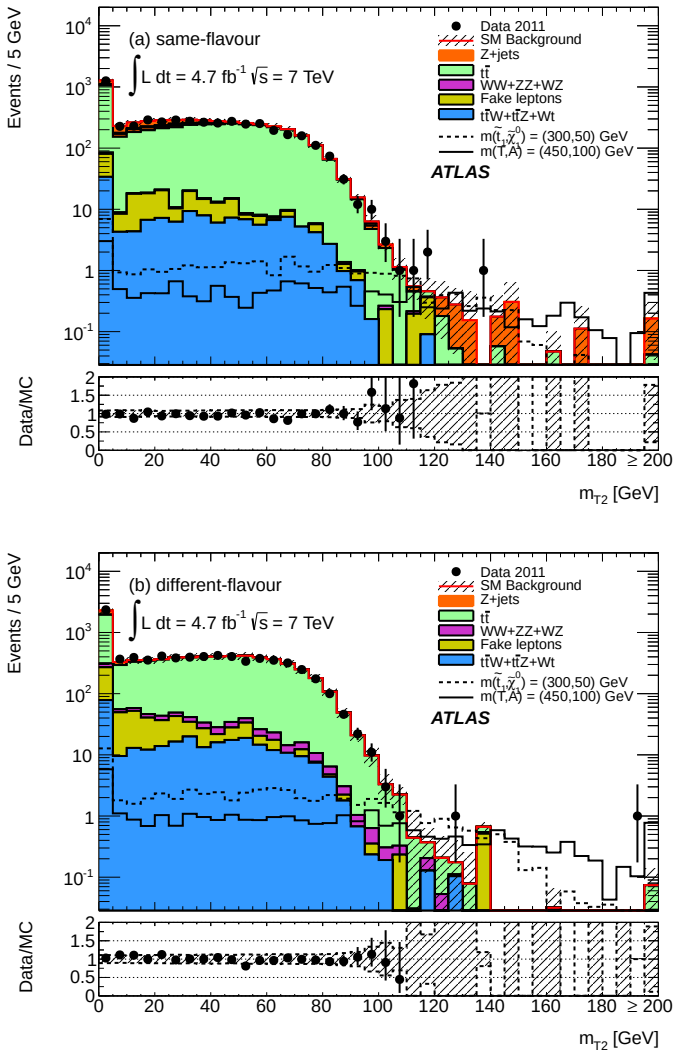

Figure 4.9: Distribution of m_{T2}^{ll} for events passing the signal candidate selection requirements except that on m_{T2}^{ll} itself, for SF (top) and DF (bottom) events. The contributions of the background processes are all derived from MC simulation, with the exception of the fake leptons background which is estimated by means of the Matrix Method. The band represents the total uncertainty (statistical plus systematic). At the bottom of the distribution, the ratio between the number of observed data events and the total MC prediction is shown. The dashed and solid black lines are the distribution for two benchmark signal models with $m(\tilde{t}_1, \tilde{\chi}_1^0) = (300, 50)$ GeV and $m(\tilde{t}_1, \tilde{\chi}_1^0) = (450, 100)$ GeV, respectively.

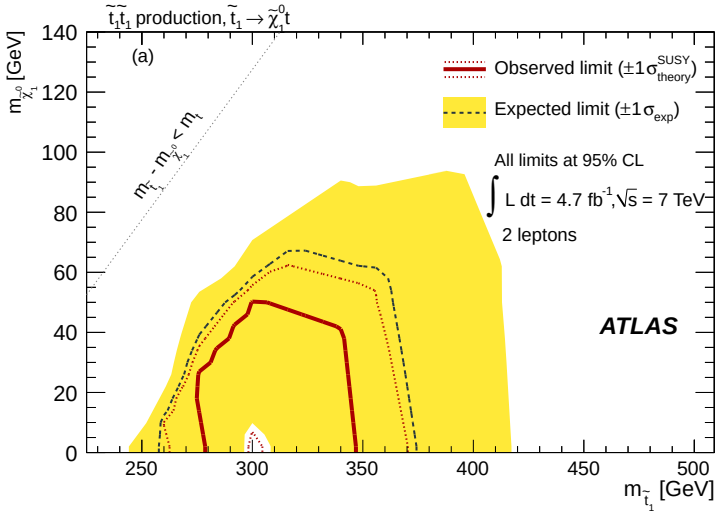

Figure 4.10: Expected and observed limits at 95% CL in the $\tilde{t}_1 \to t\tilde{\chi}_1^0$ simplified model, as a function of the stop and neutralino masses. The red solid line is the observed limit. The dashed red line and shaded yellow band are the expected limit and its $\pm 1\sigma$ uncertainty, respectively. The dotted red lines show the effect of varying by $\pm 1\sigma$ the theoretical uncertainties on the SUSY model.

5

Results of the search using 20.3 fb^{-1} of data at $\sqrt{s} = 8$ TeV

This Chapter presents the result of the search using 20.3 fb^{-1} of data at $\sqrt{s} = 8$ TeV. The estimate of all sources of background is described in details. Results are shown for two simplified models: $\tilde{t}_1 \to b\tilde{\chi}_1^{\pm}$ and $\tilde{t}_1 \to bW\tilde{\chi}_1^0$. No excess over the SM predictions has been found and exclusion limits are set on the parameters of the models. Preliminary results of this search have already been published [147]: the ones presented in this Chapter update the publication and at the time of writing are still under approval by the ATLAS Collaboration to be published on the JHEP journal.

5.1 Introduction

The analysis strategy presented for the search with $\sqrt{s} = 7$ TeV, and optimized for the $\tilde{t}_1 \to t\tilde{\chi}_1^0$ simplified model, presented some limitations when it was firstly applied to the data-set with $\sqrt{s} = 8$ TeV data, which started to be available in the early periods of 2012. The two-lepton channel showed in fact a restriction in terms of sensitivity on both sides of the stop-neutralino plane: either at high stop mass values, due to the very low cross section time branching ratio values, and approaching the diagonal $m(\tilde{t}_1) - m(\tilde{\chi}_1^0) = m(t)$, region of the parameter space where the signal kinematic cannot be easily distinguished from that of a top quark pair by means of a simple cut and count approach, and where therefore the analysis looses sensitivity.

Considering also that the full-hadronic and the one-lepton final states, covered by other ATLAS searches, showed a larger sensitivity with respect to the two-lepton channel, it was then decided to move to the $\tilde{t}_1 \to b\tilde{\chi}_1^{\pm}$ simplified model, always considering direct production. Here, a two-lepton final state is obtained when, for each decay leg of the pair produced stops, the chargino decays to a W boson and a $\tilde{\chi}_1^0$, and the W boson subsequently decays to a lepton and a neutralino. The kinematic of the final state, however, depends on the mass hierarchy between the stop, the chargino, and the neutralino. It was found that the two-lepton final state has a good sensitivity to models with a moderate or large mass difference between the chargino and the neutralino, where the m_{T2}^{ll} variable can be used to discriminate the signal from the SM background. Moreover, the final state was found to have also sensitivity to the three-body decay $\tilde{t}_1 \to bW\tilde{\chi}_1^0$, kinematic region which were not covered by any other search at the LHC at that time.

The analysis strategy, the event selections and the MC and data samples utilized in this analysis have already been discussed in Chapter 3. In this Chapter, Section 5.2

presents the distributions of the most important kinematic variables used in the definition of the SRs, Sections 5.3 and 5.4 present the estimate of the main SM background sources and the background arising from fake leptons, respectively, while the outcomes of the search are finally illustrated in Sections 5.5 and 5.6.

5.2 Kinematic distributions

In this Section a comparison between data and MC simulation for the main observables used in the definitions of the SRs is shown to probe the stability of the analysis.

In all the distributions shown in the following, MC samples are normalized to their theoretical nominal cross section and the error bands on the predicted SM yields include a combination of statistical and systematic uncertainties. The background originating from fake leptons is measured through a data-driven procedure which is explained in Section 5.4, and is the only background source not evaluated from simulation.

Figures 5.1 and 5.2 show the distribution of the p_T of the leading lepton and the leading jet, respectively, after the pre-selections described in Section 3.6.2.

Figures 5.3 and 5.4 show respectively the invariant mass distribution of the two leptons and E_T^{miss} distribution of the event, all at the same selection level.

The distributions of the transverse momenta of the leading lepton and the distribution of the missing transverse energy have been chosen because these variables enter the definition of m_{T2}^{ll}, which is used as the key discriminating variable between signal and background. The distribution of the transverse momenta of the jets has been chosen due to the fact that jets are additionally required in some SRs to enhance the sensitivity on scenarios with large mass splitting between the stop and the chargino. The invariant mass distribution is finally shown to ensure the reader that the reconstruction of the two lepton system is performed consistently between data and MC simulation.

Distributions of m_{T2}^{ll} are then shown in Figures 5.14, 5.15 and 5.16, respectively for the SRs M90, M100 and M110, before the m_{T2}^{ll} cut itself and after applying the normalization procedure described in Section 5.3.

All the distributions show a very good agreement between the observed data and the MC predictions. Even the tails of the main observable distributions are well described, apart from some spurious cases, where the limited statistic of the MC samples reflects into few simulated events with high weights.

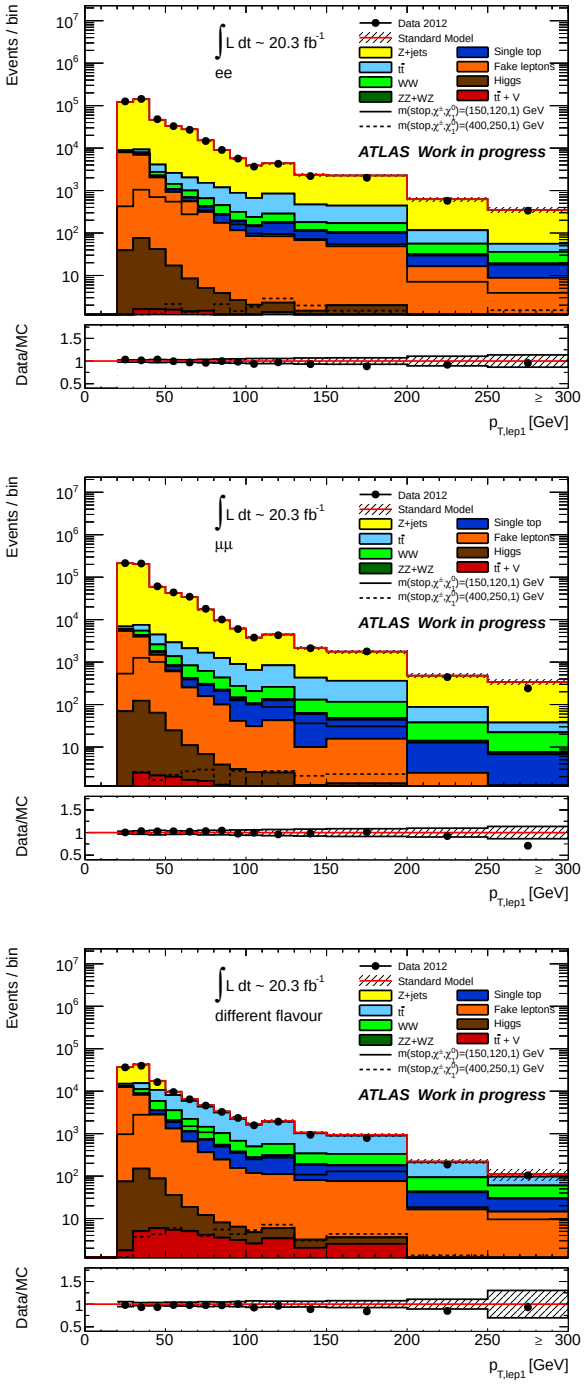

Figure 5.1: Distribution of the transverse momentum of the leading lepton, for events with two isolated leptons passing all common selection cuts. The plots report the distribution for the ee (top) and $\mu\mu$ (middle) and $e\mu$ (bottom) channel respectively. Data and predicted SM backgrounds from MC are shown, the band indicating the total uncertainty. At the bottom of the distribution, the ratio between the number of observed data events and the total MC prediction is shown. Two reference signal samples are also included in the plot: the solid black line represents a signal model with $m(\tilde{t}_1, \tilde{\chi}_1^{\pm}, \tilde{\chi}_1^0) = (150, 120, 0)$ GeV and the dashed black line a signal model with $m(\tilde{t}_1, \tilde{\chi}_1^{\pm}, \tilde{\chi}_1^0) = (400, 250, 0)$ GeV.

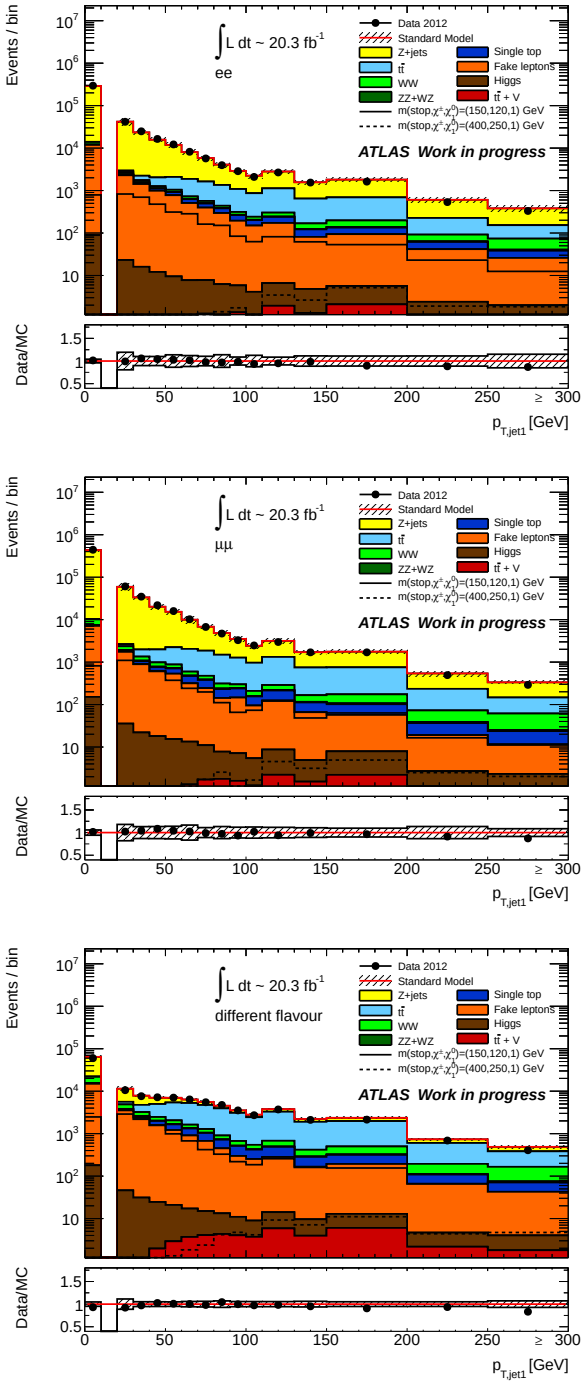

Figure 5.2: Distribution of the transverse momentum of the leading jet, for events with two isolated leptons passing all common selection cuts. The plots report the distribution for the ee (top) and $\mu\mu$ (middle) and $e\mu$ (bottom) channel respectively. Data and predicted SM backgrounds from MC are shown, the band indicating the total uncertainty. At the bottom of the distribution, the ratio between the number of observed data events and the total MC prediction is shown. Two reference signal samples are also included in the plot: the solid black line represents a signal model with $m(\tilde{t}_1, \tilde{\chi}_1^{\pm}, \tilde{\chi}_1^0) = (150, 120, 0)$ GeV and the dashed black line a signal model with $m(\tilde{t}_1, \tilde{\chi}_1^{\pm}, \tilde{\chi}_1^0) = (400, 250, 0)$ GeV.

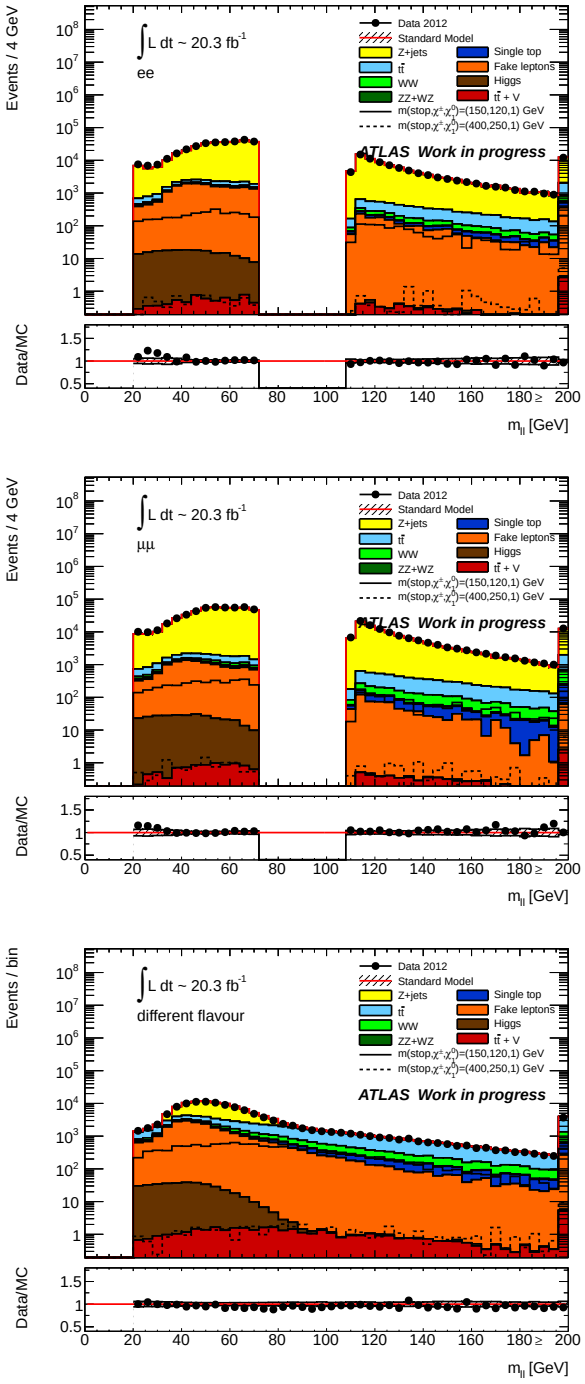

Figure 5.3: Distribution of the invariant mass of the two leptons for events with two isolated leptons passing all common selection cuts. The plots report the distribution for the ee (top) and $\mu\mu$ (middle) and $e\mu$ (bottom) channel respectively. Data and predicted SM backgrounds from MC are shown, the band indicating the total uncertainty. At the bottom of the distribution, the ratio between the number of observed data events and the total MC prediction is shown. Two reference signal samples are also included in the plot: the solid black line represents a signal model with $m(\tilde{t}_1, \tilde{\chi}_1^{\pm}, \tilde{\chi}_1^0) = (150, 120, 0)$ GeV and the dashed black line a signal model with $m(\tilde{t}_1, \tilde{\chi}_1^{\pm}, \tilde{\chi}_1^0) = (400, 250, 0)$ GeV.

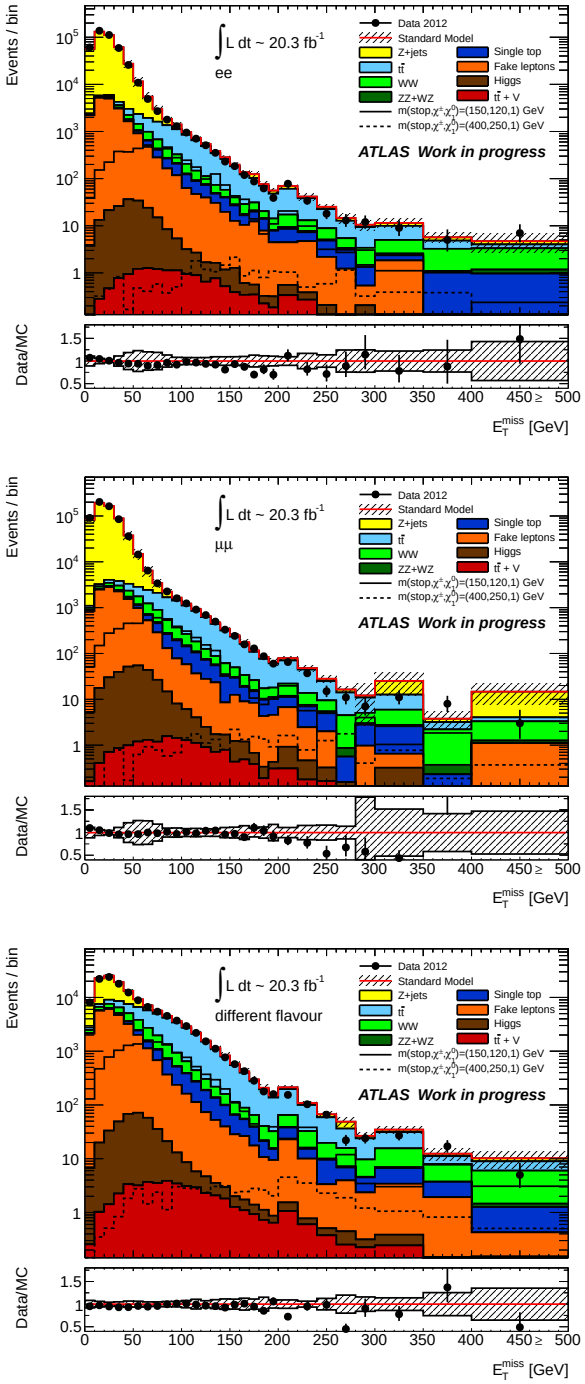

Figure 5.4: Distribution of the transverse missing energy, for events with two isolated leptons passing all common selection cuts. The plots report the distribution for the ee (top) and $\mu\mu$ (middle) and $e\mu$ (bottom) channel respectively. Data and predicted SM backgrounds from MC are shown, the band indicating the total uncertainty. At the bottom of the distribution, the ratio between the number of observed data events and the total MC prediction is shown. Two reference signal samples are also included in the plot: the solid black line represents a signal model with $m(\tilde{t}_1, \tilde{\chi}_1^{\pm}, \tilde{\chi}_1^0) = (150, 120, 0)$ GeV and the dashed black line a signal model with $m(\tilde{t}_1, \tilde{\chi}_1^{\pm}, \tilde{\chi}_1^0) = (400, 250, 0)$ GeV.

5.3 Estimate of SM background processes

Due to the $\Delta\phi$ and $\Delta\phi_b$ cuts, the Z/γ^*+jets background contamination in the SR is reduced with respect to the $\tilde{t}_1 \to t\tilde{\chi}_1^0$ analysis performed with 7 TeV data, and the main SM background sources remain $t\bar{t}$, WW and WZ/ZZ productions. Top pairs enter the SR via the leptonic decay of the two top quarks: $t\bar{t} \to W^+bW^-\bar{b} \to l^+\nu bl^-\nu\bar{b}$. WW events contribute to the SR yields via the W decay to a lepton and a neutrino: $W^+W^- \to l^+\nu l^-\nu$. WZ production contributes through its three-lepton decay mode with one of the lepton being out of the selection acceptance, and ZZ production with one Z boson decaying to two leptons and the other to two neutrinos. For all these processes, the E_T^{miss} contribution is due to the presence of neutrinos.

The main general strategy to evaluate these three background sources is to normalize the MC rates to the observed data in three CRs dominated by each of the targeted process, and then use the normalization factors (μ_T,μ_W,μ_Z) to adjust the MC predictions in the SRs. The evaluation of the three normalization factors is performed simultaneously by means of a likelihood fit: a likelihood is solved with the three observed rates in the CRs as a constraint and the three μ terms as free parameters. The systematic uncertainties discussed in Section 3.7 are included in the fit and described as nuisance parameters by a gaussian function centered on the nominal value and of width one standard deviation. The nuisance parameters are however not constrained in the fit and they are treated as uncorrelated. No contamination from signal is assumed in the CRs for this background fit.

The procedure makes use of the following formula, which relates the number of observed events from data, $N^{obs}(CR)$, with the background yields in each CR:

$$N^{obs}(CR) = \mu_T N_T^{MC}(CR) + \mu_W N_W^{MC}(CR) + \mu_Z N_Z^{MC}(CR) + N_{others}^{MC}(CR) + N_{fakes}(CR) \quad (5.1)$$

where μ_T, μ_W, μ_Z are the three normalization factors, respectively for the processes $t\bar{t}$, WW and WZ/ZZ. Of course there are three of these equations, one for each CR. $N_T^{MC}(CR)$, $N_W^{MC}(CR)$ and $N_Z^{MC}(CR)$ are the related predictions from MC in the CR, $N_{others}^{MC}(CR)$ is the predicted MC yield for the sum of all other smaller SM processes, and $N_{fakes}^{MC}(CR)$ is the number of events with fake leptons determined from data, as described in Section 5.4.

The background evaluation in each SR is then determined by scaling the MC predictions of these three main sources with the μ terms determined via the procedure described above, and by adding the other smaller SM sources (Wt, Z/γ^*+jets, Drell-Yan, $t\bar{t}W$, $t\bar{t}Z$ and Higgs) evaluated directly from MC simulations. The procedure can be summarized as follows:

$$N^{bkg}(SR) = \mu_T N_T^{MC}(SR) + \mu_W N_W^{MC}(SR) + \mu_Z N_Z^{MC}(SR) + N_{others}^{MC}(SR) + N_{fakes}(SR) \quad (5.2)$$

where again $N_T^{MC}(SR)$, $N_W^{MC}(SR)$ and $N_Z^{MC}(SR)$ are the MC predictions in the SR for $t\bar{t}$, WW and WZ/ZZ, respectively; N_{others}^{MC} is the sum of the MC rates for the smaller SM sources and N_{fakes} is the number of events with fake leptons.

The goodness of this measurement relies on a good choice of the CRs where the main background sources are measured. After the measurement, the result of the fit is cross-checked in validation regions (VRs) to verify the extrapolation procedure. The CRs and VRs used for this analysis and the results of the fit are described in details in the next section.

5.3.1 Background fit results

Three CRs are used for the measurement of the normalization factors μ_T, μ_W and μ_Z:

- **CRT**: defined by DF events passing the SR cuts on $\Delta\phi_b$ and $\Delta\phi$ but with $40 < m_{T2}^{ll} < 80$ GeV and $p_{Tb}^{ll} > 30$ GeV. This regions is mostly populated by $t\bar{t}$ events, with a purity around 75%.

- **CRW**: defined by DF events with $40 < m_{T2}^{ll} < 80$ GeV and $p_{Tb}^{ll} < 15$ GeV and passing the SR cuts on $\Delta\phi_b$ and $\Delta\phi$. Only DF events are used, since the SF channels have a signicant contamination from events with a Z boson. A reasonably pure WW sample, with an expected purity of 65%, is obtained for this region.

- **CRZ**: defined by SF events passing the $\Delta\phi_b$ and $\Delta\phi$ cuts, $m_{T2}^{ll} > 90$ GeV and with the two-lepton invariant mass lying inside the $Z-$mass window: $71 < m_{ll} < 111$ GeV. An expected purity of 69% in WZ and ZZ events is obtained.

Fig. 5.5 illustrates the distribution of the p_{Tb}^{ll} variable after the requirement of $40 < m_{T2}^{ll} < 80$ GeV and the angular cuts on $\Delta\phi_b$ and $\Delta\phi$. The region with $p_{Tb}^{ll} > 30$ GeV corresponds to the CRT, while the region with $p_{Tb}^{ll} < 15$ GeV is CRW. The distribution of m_{T2}^{ll} for events passing all the CRZ cuts except the m_{T2}^{ll} one is shown in Fig. 5.6. CRZ corresponds to the region with $m_{T2}^{ll} > 90$ GeV.

The obtained normalization factors are listed in Table 5.1. They are all compatible with one. The results of the background fits with the evaluated yields in the CRs are reported in Table 5.2, where the expected background composition from the MC simulations, which is given as input to the fit procedure, is also reported for comparison.

To verify the extrapolation procedure, the background fit predictions are compared to the observed event rates in four VRs, defined alike the SRs and CRs. VRSF and

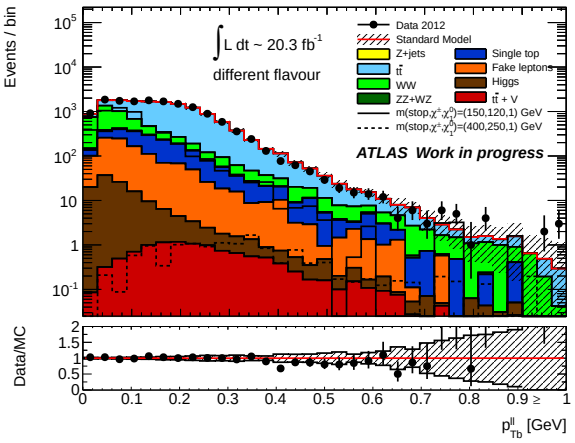

Figure 5.5: Distribution of p_{Tb}^{ll} for DF events with two isolated leptons, $40 < m_{T2}^{ll} < 80$ GeV, $\Delta\phi > 1$, $\Delta\phi_b < 1.5$. Both data and MC predictions are shown. The band indicates the total uncertainty. Two reference signal samples are also included in the plot: the solid black line represents a signal model with $m(\tilde{t}_1, \tilde{\chi}_1^{\pm}, \tilde{\chi}_1^0) = (150, 120, 0)$ GeV and the dashed black line a signal model with $m(\tilde{t}_1, \tilde{\chi}_1^{\pm}, \tilde{\chi}_1^0) = (400, 250, 0)$ GeV.

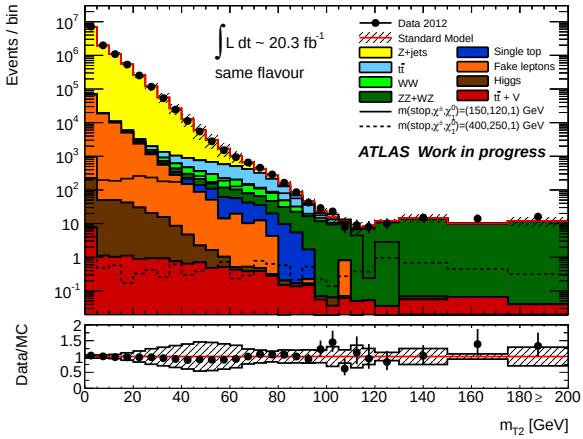

Figure 5.6: Distribution of m_{T2}^{ll} for events with two SF isolated leptons with a invariant mass between 71 GeV and 111 GeV, $\Delta\phi > 1$, and $\Delta\phi_b < 1.5$. Both data and MC predictions are shown. The band indicates the total uncertainty. Two reference signal samples are also included in the plot: the solid black line represents a signal model with $m(\tilde{t}_1, \tilde{\chi}_1^{\pm}, \tilde{\chi}_1^0) = (150, 120, 0)$ GeV and the dashed black line a signal model with $m(\tilde{t}_1, \tilde{\chi}_1^{\pm}, \tilde{\chi}_1^0) = (400, 250, 0)$ GeV.

VRDF are defined as SF and DF events, respectively, which pass all the SRs cuts, excluding the jet selections, but with $80 < m_{T2}^{ll} < 90$ GeV. They are as close as possible to the inclusive SR M90. VR20 and VR100, instead, are defined as the CRT, but with the additional requirement of the presence of two jets with $p_T > 20$ GeV, in the first case, and two jets with $p_T > 100$ GeV and $p_T > 50$ GeV, in the second case, in analogy with the SRs M100 and M110. The result of the validation is reported in Table 5.3. In all regions, the observed number of data events are in agreement with the predicted event yields within the systematics, the largest discrepancy being of 0.9 standard deviations.

Scale Factor	Value
μ_T	0.91 ± 0.07
μ_{WW}	1.27 ± 0.24
μ_{WZ+ZZ}	0.85 ± 0.16

Table 5.1: Scale factors for the $t\bar{t}$, WW, and the sum of WZ and ZZ backgrounds.

channel	CRT	CRW	CRZ
Observed events	12158	913	174
Total (constrained) bkg events	12158 ± 110	913 ± 30	174 ± 13
Fitted $t\bar{t}$ events	8610 ± 400	136 ± 24	27 ± 6
Fitted WW events	1600 ± 400	630 ± 50	14 ± 4
Fitted WZ events	63 ± 12	14 ± 5	36 ± 7
Fitted ZZ events	1.8 ± 0.5	0.48 ± 0.25	76 ± 13
Total expected bkg events	12700 ± 700	800 ± 90	190 ± 20
Fit input, expected $t\bar{t}$ events	9500 ± 600	150 ± 25	30 ± 7
Fit input, expected WW events	1260 ± 110	490 ± 80	10.7 ± 2.5
Fit input, expected WZ events	73 ± 10	16 ± 5	42 ± 5
Fit input, expected ZZ events	2.13 ± 0.60	0.57 ± 0.26	90 ± 6
Expected $Z\gamma^* \to \ell\ell$ events	9^{+11}_{-9}	$1.5^{+2.2}_{-1.5}$	19 ± 8
Expected $t\bar{t} + V$ events	10.8 ± 3.4	0.08 ± 0.04	0.64 ± 0.21
Expected Wt events	1070 ± 90	35 ± 7	1.6 ± 1.1
Expected tZ events	0.59 ± 0.08	$0.00^{+0.01}_{-0.00}$	0.36 ± 0.07
Expected Higgs boson events	67 ± 21	20 ± 6	0.08 ± 0.04
Expected events with fake leptons	740 ± 90	81 ± 16	0.0 ± 0.0

Table 5.2: Background fit results for the three CRs. The nominal expectations from MC simulation are given for comparison also for those backgrounds ($t\bar{t}$, WW, WZ and ZZ) which are normalised to data. Combined statistical and systematic uncertainties are given. Events with fake leptons are estimated with the data-driven technique described in Section 5.4. The observed events and the total (constrained) background are the same by construction. Uncertainties on the predicted background event yields are quoted as symmetric except where the negative error reaches down to zero predicted events, in which case the negative error has been truncated.

channel	VRSF	VRDF	VR110	VR100
Observed events	494	622	8162	1370
Total bkg events	500 ± 40	620 ± 50	7800 ± 400	1390 ± 110
Fitted $t\bar{t}$ events	338 ± 19	430 ± 29	6800 ± 400	1230 ± 110
Fitted WW events	97 ± 22	121 ± 27	290 ± 70	38 ± 15
Fitted WZ events	3.6 ± 0.8	2.0 ± 1.2	13.2 ± 3.2	1.4 ± 1.2
Fitted ZZ events	2.2 ± 0.7	0.15 ± 0.07	0.27 ± 0.17	$0.02^{+0.02}_{-0.02}$
Expected $Z\gamma^* \to \ell\ell$ events	4^{+5}_{-4}	0.0 ± 0.0	3^{+5}_{-3}	1^{+1}_{-1}
Expected $t\bar{t} + V$ events	0.48 ± 0.18	0.80 ± 0.27	10.1 ± 3.1	4.1 ± 1.3
Expected Wt events	39 ± 8	60 ± 10	430 ± 50	62 ± 8
Expected tZ events	0.04 ± 0.02	0.01 ± 0.01	0.33 ± 0.06	0.06 ± 0.02
Expected Higgs boson events	0.39 ± 0.16	0.55 ± 0.20	14 ± 4	1.7 ± 0.6
Expected events with fake leptons	10.5 ± 3.5	13 ± 4	275 ± 33	45 ± 7

Table 5.3: Background fit results for the four VRs. Combined statistical and systematic uncertainties are given. Events with fake leptons are estimated with the data-driven technique described in Section 5.4. The observed events and the total (constrained) background are not the same for the VRs, where the consistency between these event yields is the test of the background model. Uncertainties on the predicted background event yields are quoted as symmetric except where the negative error reaches down to zero predicted events, in which case the negative error has been truncated.

5.4 Estimate of the fake leptons background

Estimate of events with fake leptons has been reviewed in the 8 TeV analysis with respect to the 7 TeV case. The general approach used in the 7 TeV case was to measure the fake rate in QCD-enriched control samples studied ad-hoc to be similar to the SR. For the 8 TeV analysis, however, the different trigger signatures employed and the multiple definitions of SRs, CRs and VRs, required a more flexible strategy, above all for the measurement of the fake rate, which should now improve the stability of the measurement with respect to a wider range of selections.

The motivation of this can be seen in Fig. 5.7, which compares the electron fake rate distribution, as a function of the number of jets, in two different fakes-enriched samples. Both samples are obtained by requiring two DF SS leptons, but one has in addition a request of low E_T^{miss} values ($E_T^{miss} < 50$ GeV), while the other has an intermediate m_{T2}^{ll} cut ($30 < m_{T2}^{ll} < 50$ GeV). The curves of the two samples behave differently, especially at low jet multiplicity. This is due to the fact that the two samples are different in terms of composition of fake leptons. The former is in fact expected to be dominated by the QCD multijet background with double fake leptons, while the latter is dominated by W+jets and $t\bar{t}$ events with one real and one fake leptons. This effect thus provides a non-negligible influence on the fake rate measurement, and need to be handled coherently between CRs and SRs.

5.4.1 Efficiencies estimate

The leptons fake rate f is computed from the ratio $f = N_T/N_L$, where N_T (N_L) is the number of tight (loose) leptons, in two separate fake-enriched regions defined on the

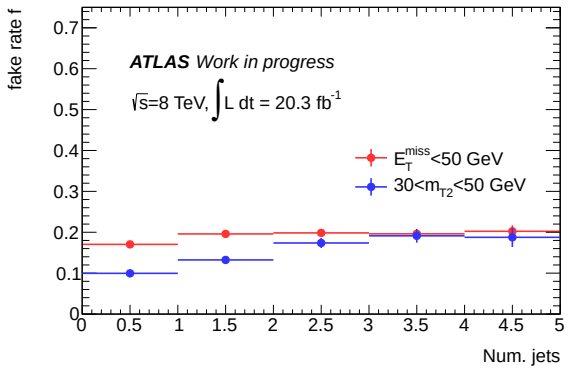

Figure 5.7: Electron fake rate distributions as a function of the number of jets, measured from a sample of DF SS leptons. The red curve is derived requiring in addition $E_T^{miss} < 50$ GeV while the blue one requiring $30 < m_{T2}^{ll} < 50$ GeV. The two regions show a different behavior of the fake rate due to the different composition in terms of fakes.

basis of the lepton p_T:

- Case A: $p_T(l) < 25$ GeV. It is assumed that the event has been triggered by one of the two-lepton low-p_T triggers. f is thus obtained from a sample of DF SS events, labelled 2LCR, yielded by requiring the trigger signatures EF_e12Tvh_medium1_mu8 or EF_mu18_tight_e7_medium1 to have fired[1].

- Case B: $p_T(l) > 25$ GeV. The event is assumed to be triggered by one-lepton high-p_T triggers (EF_e24vhi_medium1 OR EF_e60_medium1 for electrons and EF_mu24i_tight OR EF_mu36_tight for muons). f is thus measured from a one-lepton sample, labelled 1LCR, collected with non-isolated prescaled triggers (e24vh_medium1 and mu24_tight for the electron and muon channels respectively), and requiring $n_{jet} > 1$, $\Delta\phi_{lE_T^{miss}} < 0.5$ and $E_T^{miss} < 25$ GeV, in order to enhance the contribution from the QCD multijet background. The effect of the prescaled triggers, which accept only one event every ten, vanishes when computing the ratio N_T/N_L, since both the nominator and the denimonator values are prescaled.

The parameterization of the fake rate is now treated separately for the two cases. In the A case, the composition of the events which originated the fake leptons is firstly guessed through the variable m_{eff}, here defined as the scalar sum of the lepton momenta, the transverse missing energy and the first four jet momenta. The fake rate is then parameterized as a function of the lepton η and p_T, the number of jets and m_{T2}^{ll}. The m_{eff} and m_{T2}^{ll} variables help to isolate the contributions expected to dominate among di-jet, W+jets, or $t\bar{t}$ productions.

The parameterization is carried out on a two-dimensional (2D) plane where the x-axis is one of the above variables and the y-axis is the m_{eff} value. Fig. 5.8 shows the 2D parameterization of the electron (top) and muon (bottom) fake rate as a function of m_{eff} and the p_T of the lepton. Fig. 5.9 shows the fake rate as a function of m_{eff} and the number of jets, both for the electron and muon channels. Fig. 5.10 shows the fake rate as a function of m_{eff} and m_{T2}^{ll}, in the electron channel. The parameterization

[1]See Section 3.5 for a complete list of all the trigger signatures of the analysis.

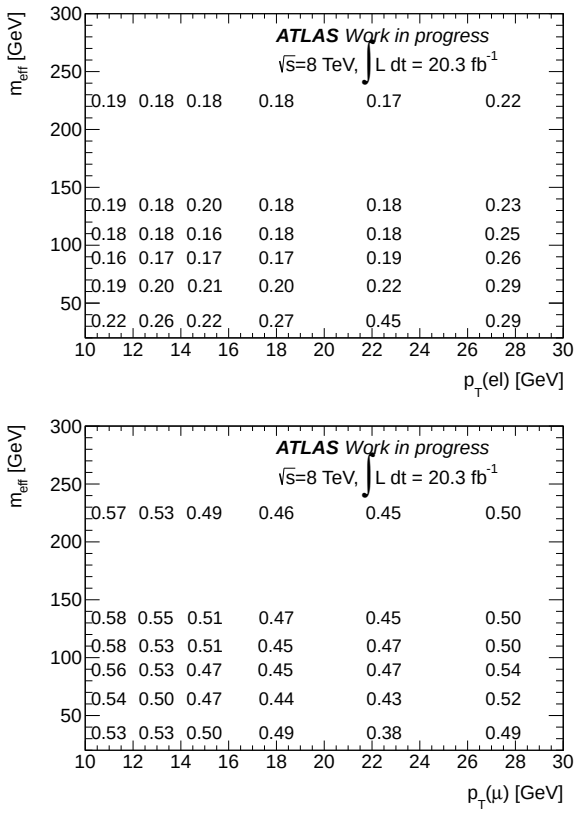

Figure 5.8: 2D fake rate distribution as a function of m_{eff} and the p_T of the lepton, for electrons (top) and muons (bottom).

on m_{T2}^{ll} is applied only in the electron channel, since the 2LCR sample has a non-negligible contamination from prompt muons in high m_{T2}^{ll} bins. The parameterization is performed as follows:

- the fake rate $f(p_T, m_{eff})$ is taken from a 2D plane as a function of the lepton p_T and m_{eff} in sample 2LCR, as shown in Fig. 5.8,
- f is than parameterized by variable X, by using the formula $f' = f \times \frac{f''(X,m_{eff})}{<f(m_{eff})>}$, where $< f(m_{eff}) >$ is the nominal fake rate measured in bins of m_{eff},
- in the muon channel, the parameterization is refused if $\frac{f''(X,m_{eff})}{<f(m_{eff})>} > 1$, in order to avoid contamination from prompt leptons or low statistics bins,
- the parameterization is repeated for the other remaining variables.

In all the measurements, the prompt leptons contribution is subtracted via MC simulation.

In the B case, the fake rate is taken from sample 1LCR as a function of the lepton p_T and parameterized in bins of η and by the number of jets of the event. In the muon channel, the p_T parameterization is stopped at 40 GeV, since studied performed in Section 4.3 have shown that high-p_T regions start to have a predominant contribution from prompt muons.

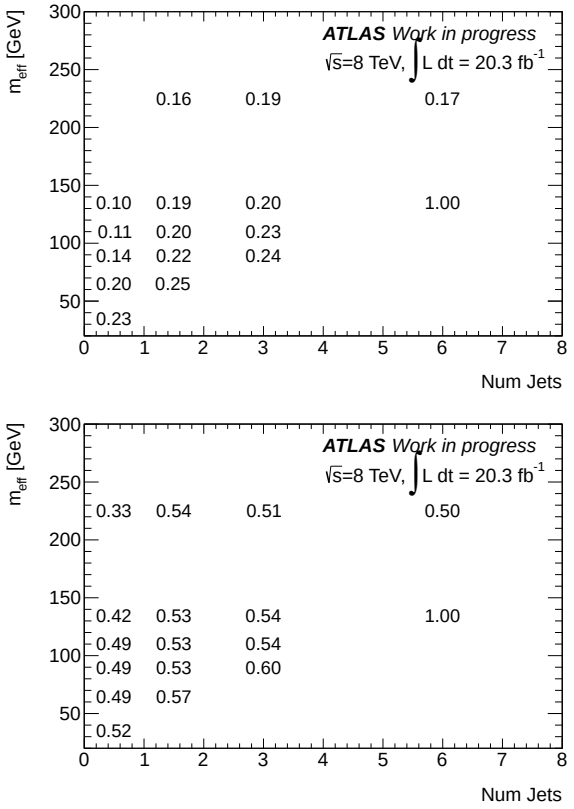

Figure 5.9: 2D fake rate distribution as a function of m_{eff} and the number of jets of the event, for electrons (top) and muons (bottom) with $p_T(l) < 25$ GeV.

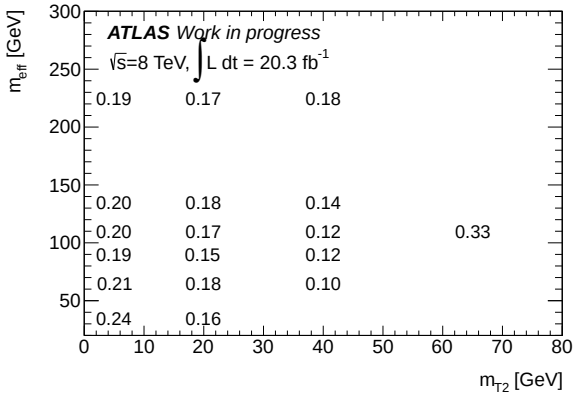

Figure 5.10: 2D fake rate distribution as a function of m_{eff} and m_{T2}^{ll} of the event, for electrons with $p_T < 25$ GeV.

5.4.2 Uncertainties

The systematic uncertainties affecting the determination of the fake rate f are now treated according to case A or B.

In the A case, a source of systematic uncertainty is due to the calculation of m_{eff} and the lepton p_T and thus to the selection of the bin in the 2D-plane. A conservative

10% variation on the value of m_{eff} and p_T is then introduced on the measurement of f, and the largest deviation from the nominal fake rate is taken as uncertainty. Another source of systematic is the choice of the method used to measure the efficiency: the fake rate is re-evaluated from sample 1LCR and using the case B technique, and the difference with respect to the nominal value is taken as uncertainty.

For the B case, the fake rate is re-evaluated by using sample 2LCR and by applying the case A technique, and the difference between the two values is taken as uncertainty.

In both cases the limited statistics of the binned CR used to measure f is considered as a source of systematic uncertainty and added in quadrature with the previous sources.

The parameterized uncertainties are in general dominated by discrepancies in the measurement of the fake lepton probabilities obtained when using the two different control regions above. The overall systematic uncertainty ranges between 10 and 50% across the various regions (control, validation and signal). Ultimately in SRs with very low predicted event yields the overall uncertainty on the fake lepton background yield is dominated by the statistical uncertainty arising from having few data events in the SRs, and reaches 60-80% in the tightest SRs. In these regions, however, the contributions from fake lepton events are small or negligible.

5.4.3 Validation of the method

The predictions are validated, in analogy with the 7 TeV case, using SS two-lepton samples at different stages of the cutflow. Additional regions are also used to validate the robustness of the estimate against contributions from different sources of fake leptons. These regions include SS events with $m_{eff} < 120$ GeV and $30 < m_{T2}^{ll} < 50$ GeV.

Fig. 5.11 shows the m_{eff} distribution after the $\Delta\phi$ and $\Delta\phi_b$ cuts of the analysis. Figures 5.12 and 5.13 show the number of jets and m_{T2}^{ll} distributions, respectively, after the requirement of $m_{eff} < 120$ GeV. In the latter figure, low m_{T2}^{ll} bins are dominated by di-jet events from the multijet QCD background, but in the region $30 < m_{T2}^{ll} < 50$ GeV the W+jets and WW productions become the dominant sources.

Good agreement between data and the predicted fakes is found in all three channels for all the regions, showing that the method outlined here is robust against selections which accent different sources of fake leptons. In the figures, the contribution from prompt leptons is added from the MC simulation by asking a match of the reconstructed leptons with the leptons at truth level, in order to avoid a double counting of the fakes.

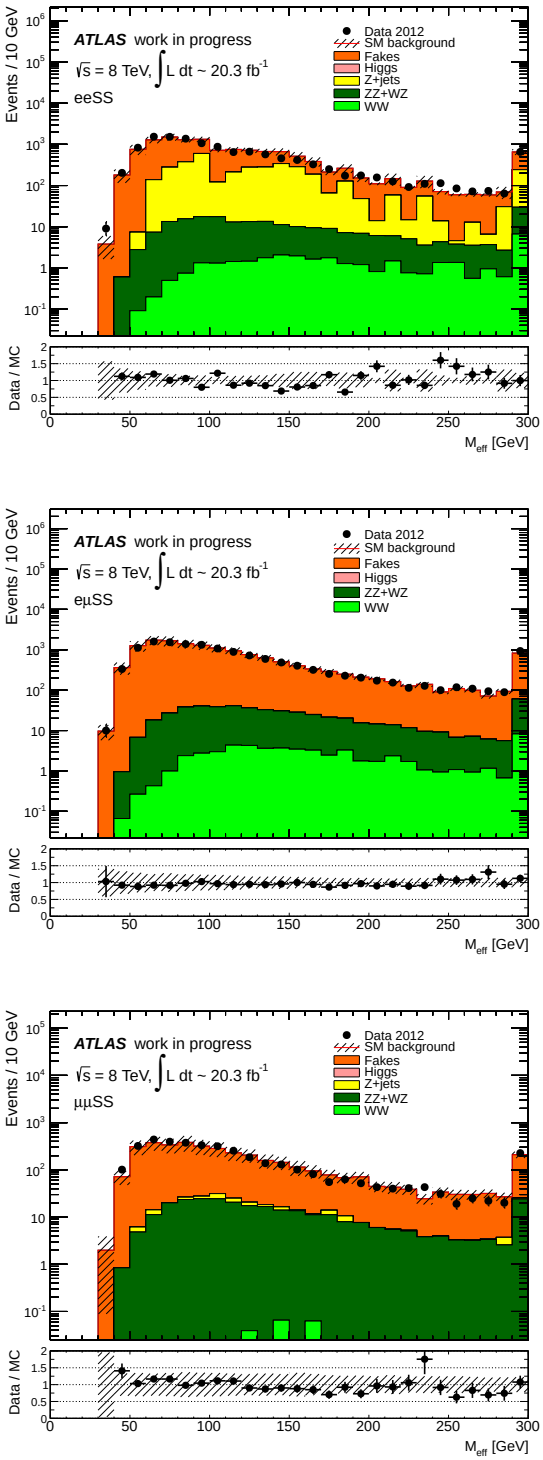

Figure 5.11: m_{eff} distribution of SS events (top: ee; middle: $e\mu$; bottom: $\mu\mu$) after the requirements of two signal leptons, $\Delta\phi > 1$ and $\Delta\phi_b < 1.5$. Both data and the predicted fakes are shown. All other SM processes are simulated via MC, normalized at the nominal cross-sections. At the bottom of the distribution, the ratio between the number of observed data events and the total MC prediction is shown. A match at truth level is required for the reconstructed leptons in the MC samples to avoid double counting the fakes. The band indicates statistical plus systematic uncertainties on the estimate.

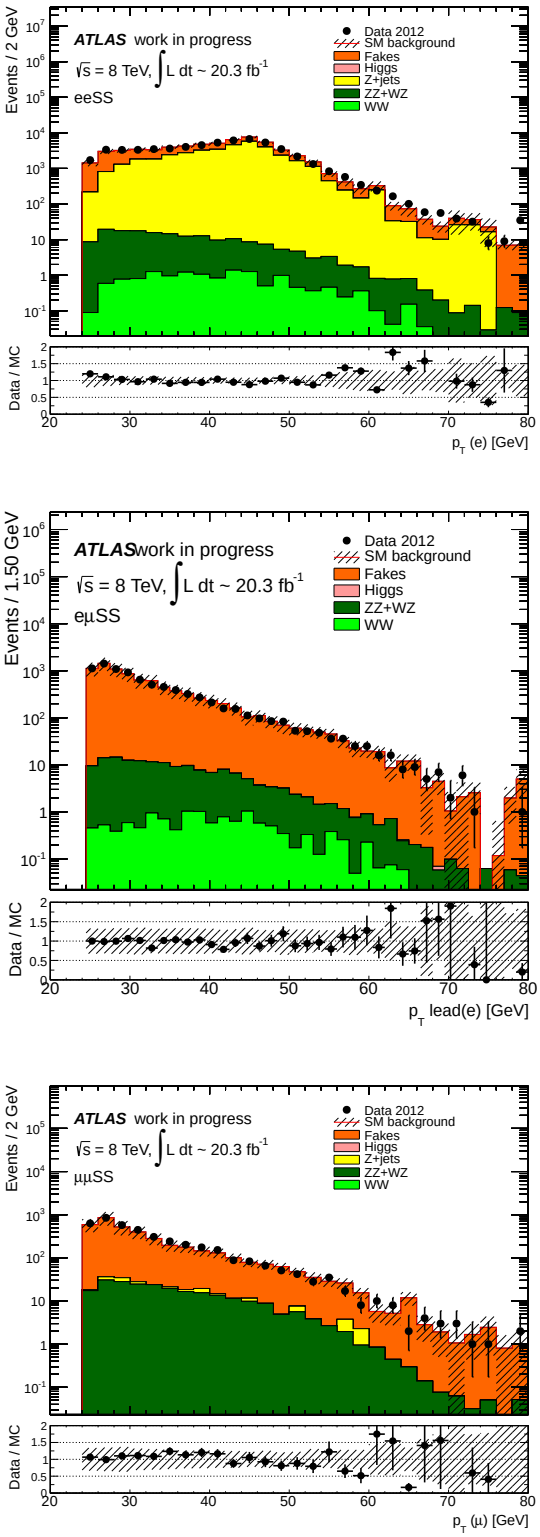

Figure 5.12: Distribution of the leading lepton p_T in SS events (top: ee; middle: $e\mu$; bottom: $\mu\mu$) after the requirements of two signal lepton and $m_{eff} < 120$ GeV. Both data and the predicted fakes are shown. All other SM processes are are simulated via MC, normalized at the nominal cross-sections. At the bottom of the distribution, the ratio between the number of observed data events and the total MC prediction is shown. A match at truth level is required for the reconstructed leptons in the MC samples to avoid double counting the fakes. The band indicates statistical plus systematic uncertainties on the estimate.

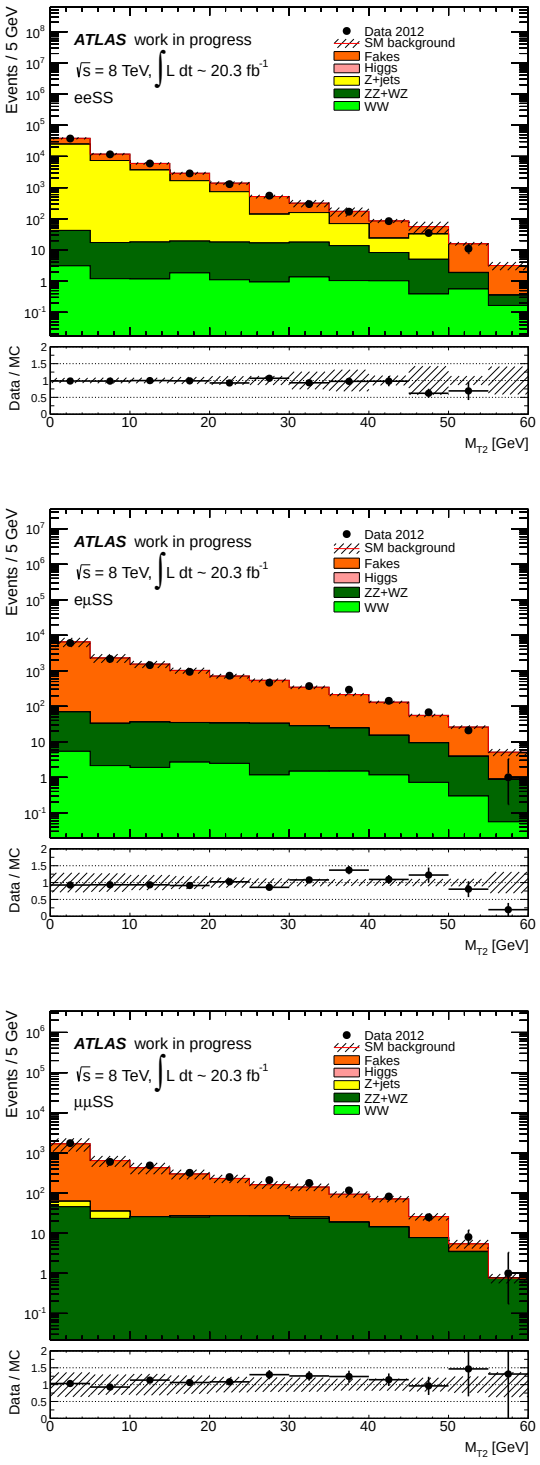

Figure 5.13: $m_{T2}^{ll}(ll)$ distribution of SS events (top: ee; middle: $e\mu$; bottom: $\mu\mu$) after the requirements of two signal leptons and $m_{eff} < 120$ GeV. Both data and the predicted fakes are shown. All other SM processes are are simulated via MC, normalized at the nominal cross-sections. At the bottom of the distribution, the ratio between the number of observed data events and the total MC prediction is shown. A match at truth level is required for the reconstructed leptons in the MC samples to avoid double counting the fakes. The band indicates statistical plus systematic uncertainties on the estimate.

5.5 Results

The methods described so far are used to estimate the SM background sources in the SRs, which are then compared to the observed rates, seeking for any excess as a hint of new physics. To help in the visualization of the results, the m_{T2}^{ll} distributions after all SR selections, except the m_{T2}^{ll} cut, are shown in Figures 5.14, 5.15 and 5.16, for the M90, M100 and M110 SRs, respectively. Distributions for M90 and M120 are equivalent since the two SRs only differ for the cut in m_{T2}^{ll}. All plots include a comparison between the observed data and the SM background predictions, measured from MC simulation and normalized to data with the background fit procedure, as described in Section 5.3. Background arising from fake leptons is evaluated with the data-driven technique described in Section 5.4. Above the 90, 100, 110 and 120 GeV values on the x-axis, which represents the m_{T2}^{ll} variable, the plots include the SRs with their observed yields and the SM predictions. As can be seen in the figures, in all the distributions the SM predictions agree with the observed data within uncertainties.

Table 5.4 shows the expected yields in the four SRs for each background source and the observed number of events from data. The sum of events in the SF and DF channels is considered in this case.

A breakdown of the various sources of the total uncertainty is listed in Table 5.5. This table quotes, for each SR, the absolute value of each source of systematic uncertainty on the background yield. Since these uncertainties are correlated, there is no requirement for these to sum in quadrature to 100%. For M90, M100 and M110, which are dominated by $t\bar{t}$, the main contribution arises from the differences in the predictions of the MC@NLO and POWHEG generators. In M120, which is on the countrary dominated by WW production, the largest uncertainty comes from the comparison of the two diboson generators SHERPA and POWHEG. Relevant contributions also arise from the JER, pile-up and soft term uncertainties in almost all regions. The uncertainty on the WZ/ZZ normalization (where appropriate) has comparable statistical and systematic components, whilst the $t\bar{t}$ ($t\bar{t}, Wt$) and WW normalization uncertainties are systematics dominated. The total uncertainty varies between 17% and 47%, depending on the region, and is higher in M100 and in M120, due to the tightest cuts in the jet multiplicity and in m_{T2}^{ll}, respectively.

Since no evidence of excess is observed, model independent limits at 95% CL are derived on the visible cross section on new physics, $\sigma_{vis} = \sigma \times \epsilon \times \mathcal{A}$, as shown in Table 5.6. Limits are also placed on the parameters of the SUSY simplified models considered for this analysis.

To derive the limits, the number of events observed in each SR is compared with the SM expectations using frequentist exclusion limits based on profile log-likelihood ratio tests with the CL_s prescriptions [146]. To do so, a likelihood function $\mathcal{L}(n_s)$ is defined as follows:

$$\mathcal{L}(n_s; \mu b, \theta) = Poiss(n_s | s(\mu, b, \theta)) \times \prod_i N_{syst}^i(\theta_0^i, \theta^i) \tag{5.3}$$

where $Poiss(n_s)$ is a Poissonian probability density function (pdf) describing the expected event counts n_s in each SR, given the expectation s. μ is the signal strength to be tested, b the number of background events and θ describes the systematic uncertainties as nuisance parameters. $\prod_i N_{syst}^i$ is the convolution of Gaussian pdfs which models the individual systematic uncertainty components around their nominal value.

The test statistic is then defined as twice the difference between the log-likelihood of the signal model, with signal strength μ, and that of the background-only model, obtained by fixing $\mu = 0$. The $p-$value of the observation is then extracted from the pdf of the test statistic, generated using toy MC experiments, and validated using the asymptotic formulas.

For a specific signal model, the signal hypothesis is rejected at 95% CL if $p-$value$<$ 0.05. For this procedure, signal contamination is taken into account in the CRs and signal prediction uncertainties include detector response, luminosity and MC statistic uncertainties. Theoretical uncertainties on the signal cross section and on the description of the PDFs are not included, but the limits are re-measured for their $\pm 1\sigma$ variations. Uncertainties which affects both the background and the signal are considered as completely correlated.

For the model independent limits, only background uncertainties are considered, and the procedure assumes there is no contamination from new physics in the CRs. The upper limit on μ is calculated as the highest value of μ not excluded, found by solving $p_\mu = 0.05$ for μ. With this value, one derives the upper-limits on the number of non-SM events and on the visible cross section.

channel	M90	M100	M110	M120
Observed events	274	3	8	18
Total bkg events	300 ± 50	5.2 ± 2.2	9.3 ± 3.5	19 ± 9
Fitted $t\bar{t}$ events	172 ± 33	3.5 ± 2.1	3.4 ± 2.9	$1.1^{+1.1}_{-1.1}$
Fitted WW events	78 ± 20	1.0 ± 0.5	3.2 ± 1.4	12 ± 7
Fitted WZ events	6 ± 1	$0.09^{+0.16}_{-0.09}$	0.36 ± 0.28	1.2 ± 1.0
Fitted ZZ events	6.9 ± 1.7	0.14 ± 0.11	0.56 ± 0.31	3.0 ± 1.1
Fit input, expected $t\bar{t}$ events	190 ± 40	3.9 ± 2.4	3.7 ± 3.2	$1.2^{+1.2}_{-1.2}$
Fit input, expected WW events	62 ± 9	0.75 ± 0.38	3 ± 1	9 ± 5
Fit input, expected WZ events	6 ± 1	$0.10^{+0.19}_{-0.10}$	0.42 ± 0.31	1.4 ± 1.2
Fit input, expected ZZ events	8.1 ± 1.6	0.16 ± 0.12	0.66 ± 0.34	3.5 ± 1.3
Expected $Z\gamma^* \to \ell\ell$ events	2.8 ± 1.4	$0.14^{+0.14}_{-0.14}$	$0.09^{+0.14}_{-0.09}$	$0.07^{+0.09}_{-0.07}$
Expected $t\bar{t} + V$ events	1.8 ± 0.6	0.35 ± 0.14	0.62 ± 0.21	0.51 ± 0.18
Expected Wt events	21 ± 7	$0.00^{+0.19}_{-0.00}$	–	$0.35^{+0.39}_{-0.35}$
Expected tZ events	0.04 ± 0.02	–	0.01 ± 0.01	0.01 ± 0.01
Expected Higgs boson events	0.65 ± 0.22	$0.02^{+0.02}_{-0.02}$	0.03 ± 0.03	0.31 ± 0.12
Expected events with fake leptons	13.0 ± 3.5	–	1.0 ± 0.6	1.1 ± 0.8

Table 5.4: Background fit results for the M90, M100, M110 and M120 region(s), for an integrated luminosity of 20.3 fb^{-1}. Nominal MC expectations (normalised to MC cross-sections) are given for comparison. Estimate of events with fake leptons is evaluated with the data-driven procedure described in section 5.4. The errors shown are the statistical plus systematic uncertainties.

Channel	M90	M100	M110	M120
Total background expectation	300	5.2	9.3	19
Total background uncertainty	±50 [17%]	±2.2 [42%]	±3.5 [38%]	±9 [47%]
Uncertainty source				
Jet energy resolution	±21	±1	±0.04	±0.75
$t\bar{t}$ generator	±21	±1.2	±2.6	±0.4
Soft term scale	±20	±0.56	±0.23	±0.31
Pile-up	±20	±0.49	±0.66	±1
WW yield	±15	±0.18	±0.62	±2.2
$t\bar{t}$ yield	±14	±0.29	±0.28	±0.09
$t\bar{t}$ cross section	±10	±0.21	±0.20	±0.06
$t\bar{t}$ ISRFSR	±9	±0.6	±0.03	±0.66
Trigger Efficiency	±8.6	±0.16	±0.25	±0.54
Diboson generator	±8.5	±0.52	±1.4	±8
ttbar parton shower	±8	±0.44	±0.75	±0.46
Diboson cross section	±5.3	±0.07	±0.25	±0.93
Soft term resolution	±4.2	±0.36	±0.31	±0.04
WZ ZZ yield	±2.2	±0.04	±0.17	±0.77
Fakes estimate	±1.5	-	±0.02	±0.08
Wt cross section	±1.4	-	-	±0.02
Jet energy scale	±1	±0.26	±0.12	±0.15
Z+jets generator	±0.76	±0.04	±0.03	±0.02
Lumi	±0.73	±0.01	±0.02	±0.03
$t\bar{t}$+V cross section	±0.55	±0.11	±0.18	±0.15
Higgs cross section	±0.19	±0.01	±0.01	±0.09
MC statistics M90	±6.9	-	-	-
MC statistics M100	-	±0.69	-	-
MC statistics M110	-	-	±1	-
MC statistics M120	-	-	-	±1.3

Table 5.5: Breakdown of the dominant systematic uncertainties on background estimates in the various signal regions. Note that the individual uncertainties can be correlated, and do not necessarily add up quadratically to the total background uncertainty. The percentages show the size of the uncertainty relative to the total expected background.

Signal Region	$S^{\text{exp(obs)}}$	$\sigma_{vis}^{\text{exp(obs)}}$ [fb]
M90	85 (74)	4.2 (3.6)
M100	6.4 (5.6)	0.32 (0.28)
M110	9.4 (9.0)	0.46 (0.44)
M120	17 (17)	0.89 (0.86)

Table 5.6: 95% CL expected (observed) upper limits on the number of non-SM events ($S^{\text{exp(obs)}}$) and the visible cross section ($\sigma_{vis}^{\text{exp(obs)}}$).

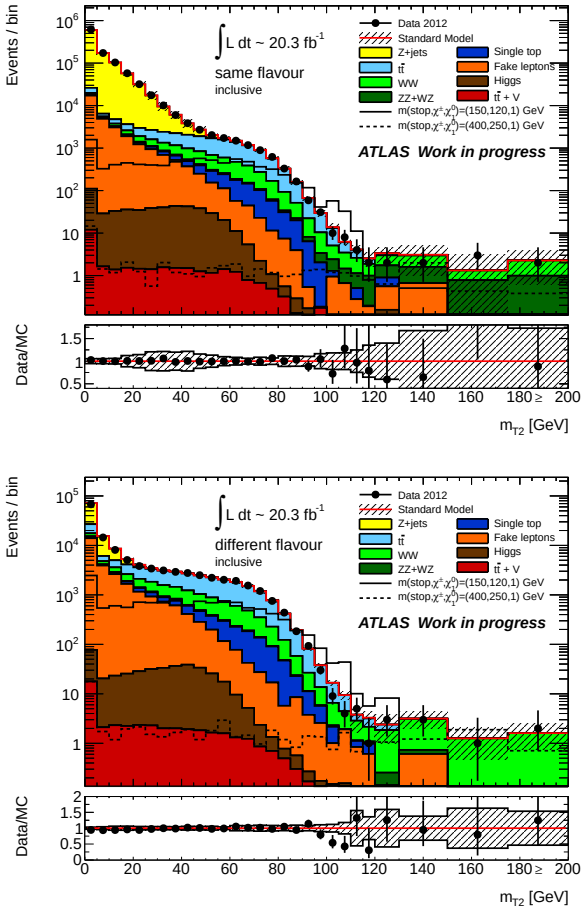

Figure 5.14: Distributions of m_{T2}^{ll} for events passing all the signal candidate selection requirements, except that on m_{T2}^{ll}, of the M90 and M120 SRs, for SF (top) and DF (bottom) events. Data and predicted SM backgrounds from MC are shown, the band indicating the total uncertainty. At the bottom of the distribution, the ratio between the number of observed data events and the total MC prediction is shown. The number of events from MC simulation of the three dominant background sources ($t\bar{t}$, WZ/ZZ and WW) is normalized to data using the results of the background fit procedure described in Section 5.3.1. The expected distributions for two signal models are also shown: the full line corresponds to a model with m($\tilde{t}_1$)=150 GeV, m($\tilde{\chi}_1^{\pm}$)=120 GeV and m($\tilde{\chi}_1^0$)=1 GeV; the dashed line to a model with m($\tilde{t}_1$) = 400 GeV, m($\tilde{\chi}_1^{\pm}$) = 250 GeV and m($\tilde{\chi}_1^0$)=1 GeV.

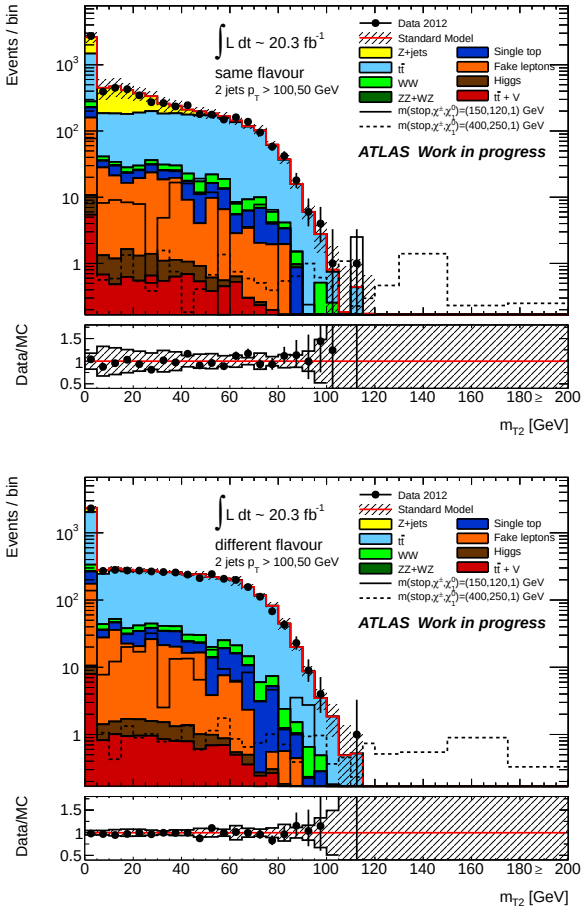

Figure 5.15: Distributions of m_{T2}^{ll} for events passing all the signal candidate selection requirements, except that on m_{T2}^{ll}, of the M100 SR, for SF (top) and DF (bottom) events. Data and predicted SM backgrounds from MC are shown, the band indicating the total uncertainty. At the bottom of the distribution, the ratio between the number of observed data events and the total MC prediction is shown. The number of events from MC simulation of the three dominant background sources ($t\bar{t}$, WZ/ZZ and WW) is normalized to data using the results of the background fit procedure described in Section 5.3.1. The expected distributions for two signal models are also shown: the full line corresponds to a model with m($\tilde{t}_1$)=150 GeV, m($\tilde{\chi}_1^{\pm}$)=120 GeV and m($\tilde{\chi}_1^0$)=1 GeV; the dashed line to a model with m($\tilde{t}_1$) = 400 GeV, m($\tilde{\chi}_1^{\pm}$) = 250 GeV and m($\tilde{\chi}_1^0$)=1 GeV.

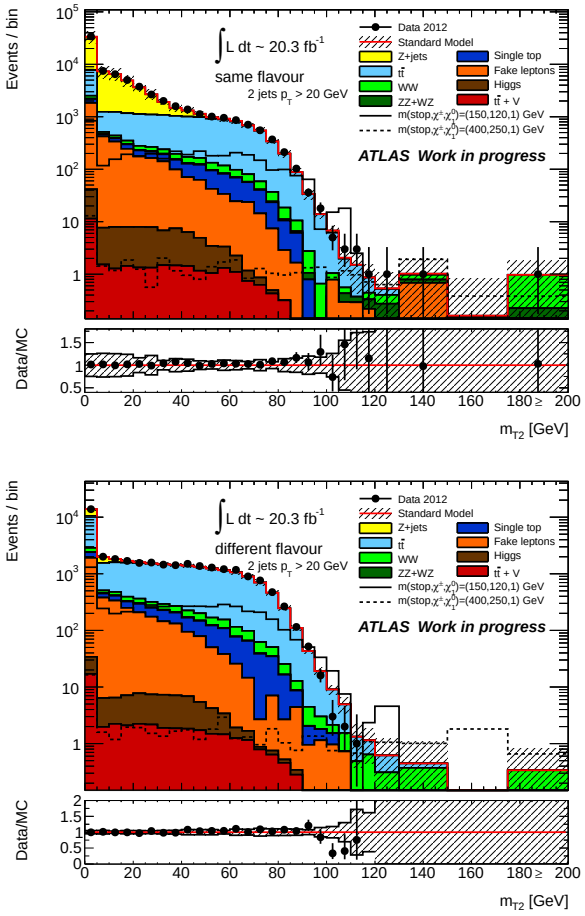

Figure 5.16: Distributions of m_{T2}^{ll} for events passing all the signal candidate selection requirements, except that on m_{T2}^{ll}, of the M110 SR, for SF (top) and DF (bottom) events. Data and predicted SM backgrounds from MC are shown, the band indicating the total uncertainty. At the bottom of the distribution, the ratio between the number of observed data events and the total MC prediction is shown. The number of events from MC simulation of the three dominant background sources ($t\bar{t}$, WZ/ZZ and WW) is normalized to data using the results of the background fit procedure described in Section 5.3.1. The expected distributions for two signal models are also shown: the full line corresponds to a model with m($\tilde{t}_1$)=150 GeV, m($\tilde{\chi}_1^{\pm}$)=120 GeV and m($\tilde{\chi}_1^0$)=1 GeV; the dashed line to a model with m($\tilde{t}_1$) = 400 GeV, m($\tilde{\chi}_1^{\pm}$) = 250 GeV and m($\tilde{\chi}_1^0$)=1 GeV.

5.6 Model dependent interpretation of results

The set of the model dependent limits required a more complicated strategy with respect to the model independent case. In fact, the four inclusive SRs described so far were designed to maximize the discovery potential of the analysis. In the absence of any excess, however, a set of statistically exclusive SRs can be defined in order to maximize the exclusion power of the analysis. Therefore, to allow a statistical combination of the SRs and maximize this potential, a set of seven statistically independent SRs is defined to cover the entire (jet selections, m_{T2}^{ll}) plane, as shown in Fig. 5.17. These SRs are labelled Sn, with n going from one to seven.

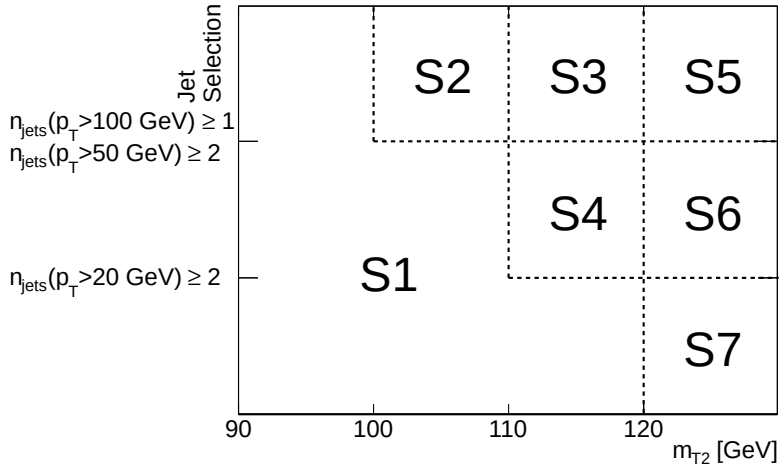

Figure 5.17: Scheme of the exclusive SRs used in the results interpretation which have been derived from the four cut and count SRs documented in the analysis.

For a single signal hypothesis, the background fit described in Section 5.3 is performed again considering signal contamination in the CRs, and the predictions of the yields in the SRs are re-evaluated. As an example, Table 5.7 shows the result of the case with a signal model with $m(\tilde{t}_1, \tilde{\chi}_1^{\pm}, \tilde{\chi}_1^0) = (300, 200, 1)$ GeV. Here, the number of events observed in each of the seven SRs used for the combination is compared to the total expected background. Individual background components are also reported. The expected and observed numbers from the seven SRs are then used to derive the $p-$value of the observation for the signal plus background hypothesis, and the fit procedure is then repeated for each hypothesis on the masses of the $\tilde{t}_1$, $\tilde{\chi}_1^{\pm}$ and $\tilde{\chi}_1^0$. Limits are finally derived in two-dimensional projections of the three-dimensional mass space, as discussed in Section 3.4.

Fig. 5.18 shows the expected (dashed blue line) and observed (solid red line) exclusion limits at 95% CL as a function of the stop and chargino masses, for a nearly massless neutralino ($m(\tilde{\chi}_1^0) = 1$ GeV). Fig. 5.19 reports the exclusion limits on the stop and neutralino masses for a chargino mass set to be twice the mass of the neutralino: $m(\tilde{\chi}_1^{\pm}) = 2 \times m(\tilde{\chi}_1^0)$. Fig. 5.20 shows the limits on the chargino and neutralino masses for a fixed 300 GeV stop and Fig. 5.21 on the stop and neutralino masses for a fixed 150 GeV chargino. The limits on the stop and neutralino masses for the three-body decay $\tilde{t}_1 \to bW\tilde{\chi}_1^0$ are illustrated in Fig. 5.22. In all plots, the coloured yellow band is the ± 1 σ variation on the expected limit and the dashed red curves are the observed

limits re-evaluated considering a $\pm 1\ \sigma$ variation on the signal theoretical uncertainties. Where possible, limits from other ATLAS SUSY searches are also drawn in the same projection, highlighting the complementarity with the results of the search described so far.

The highest constraint of this search excludes a stop mass of 550 GeV for a 400 GeV chargino and a nearly massless neutralino, considering 100% BR on the decay mode $\tilde{t}_1 \to b\tilde{\chi}_1^{\pm}$. For the three-body decay mode, a 240 GeV stop is excluded for a 100 GeV neutralino. A comparison between these results and other direct stop pair production searches which have been publicated by the ATLAS and CMS experiments is summarized in the Summary section, after this Chapter.

channel	S1	S2	S3	S4	S5	S6	S7
Observed events	250	1	2	3	0	3	15
Total bkg events	250 ± 14	2.2 ± 0.9	1.3 ± 0.4	2.8 ± 1.3	0.52 ± 0.29	3.6 ± 0.9	15 ± 4
Fitted $t\bar{t}$ events	140 ± 13	1.4 ± 0.9	0.88 ± 0.34	$1.2^{+1.3}_{-1.2}$	$0.05^{+0.12}_{-0.05}$	0.68 ± 0.33	0.90 ± 0.51
Fitted WW events	62 ± 10	0.46 ± 0.16	0.29 ± 0.15	0.98 ± 0.22	0.25 ± 0.09	1.7 ± 0.6	9.4 ± 2.5
Fitted WZ+ZZ events	7.3 ± 1.1	0.08 ± 0.05	$0.05^{+0.07}_{-0.05}$	0.13 ± 0.08	0.09 ± 0.03	0.64 ± 0.20	3.6 ± 1
Fitted signal (300,200,1)	0.00 ± 0.96	0.00 ± 0.10	0.00 ± 0.08	0.00 ± 0.18	0.00 ± 0.20	0.00 ± 0.28	0.00 ± 0.02
Exp. $t\bar{t}$ events	180 ± 30	2.9 ± 1.9	1 ± 0.4	$2.2^{+2.8}_{-2.2}$	$0.00^{+0.25}_{-0.00}$	0.55 ± 0.52	$0.61^{+0.66}_{-0.61}$
Exp. WW events	51 ± 5	0.34 ± 0.14	0.19 ± 0.16	0.77 ± 0.18	0.22 ± 0.09	1.4 ± 0.7	7.5 ± 4.2
Exp. WZ+ZZ events	8.4 ± 1	0.11 ± 0.07	$0.05^{+0.14}_{-0.05}$	0.21 ± 0.10	0.10 ± 0.06	0.72 ± 0.31	4.0 ± 2.2
Exp. $Z\gamma^* \to \ell\ell$ events	2.6 ± 1.1	$0.10^{+0.12}_{-0.10}$	$0.02^{+0.02}_{-0.02}$	$0.00^{+0.04}_{-0.00}$	0.02 ± 0.01	$0.05^{+0.09}_{-0.05}$	$0.00^{+0.01}_{-0.00}$
Exp. $t\bar{t} + V$ events	0.97 ± 0.31	0.15 ± 0.06	0.07 ± 0.03	0.14 ± 0.05	0.14 ± 0.06	0.27 ± 0.10	0.10 ± 0.06
Exp. Wt events	21 ± 6	$0.00^{+0.19}_{-0.00}$	–	–	–	–	0.35 ± 0.19
Exp. tZ events	–	–	–	–	–	–	–
Exp. Higgs events	0.31 ± 0.11	0.02 ± 0.01	–	$0.00^{+0.01}_{-0.00}$	–	0.03 ± 0.01	0.28 ± 0.09
Exp. events with fakes	12 ± 3	–	–	0.44 ± 0.38	–	0.60 ± 0.51	$0.50^{+0.59}_{-0.50}$
Exp. signal (300,200,1)	39 ± 3	4.7 ± 1.4	3.4 ± 1.5	7.8 ± 1.6	9.3 ± 2.6	11.8 ± 1.9	$1^{+1.6}_{-1}$

Table 5.7: Exclusion fit results for the S1, S2, S3, S4, S5, S6 and S7 region(s), for an integrated luminosity of 20.3 fb^{-1}, and considering a signal model with $m(\tilde{t}_1, \tilde{\chi}_1^{\pm}, \tilde{\chi}_1^0) = (300, 200, 1)$ GeV. Nominal MC expectations (normalised to MC cross-sections) are given for comparison. Estimate of events with fake leptons is evaluated with the data-driven procedure described in section 5.4. The errors shown are the statistical plus systematic uncertainties.

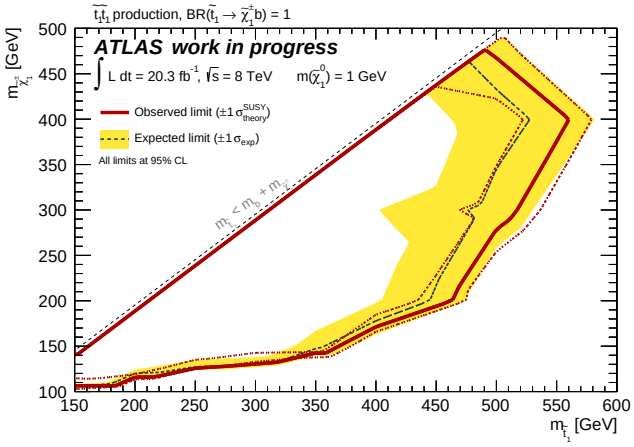

Figure 5.18: Exclusion limits at 95% CL on the masses of the stop and $\tilde{\chi}_1^{\pm}$, for a $\tilde{\chi}_1^0$ with a mass of 1 GeV and assuming BR($\tilde{t}_1 \to b\tilde{\chi}_1^{\pm}$) = 1. The dashed line and the shaded band are the expected limit and its ± 1 σ uncertainty, respectively. The thick solid line is the observed limit for the central value of the signal cross section. The dotted lines show the effect on the observed limit when varying the signal cross section by ± 1 σ of the theoretical uncertainty.

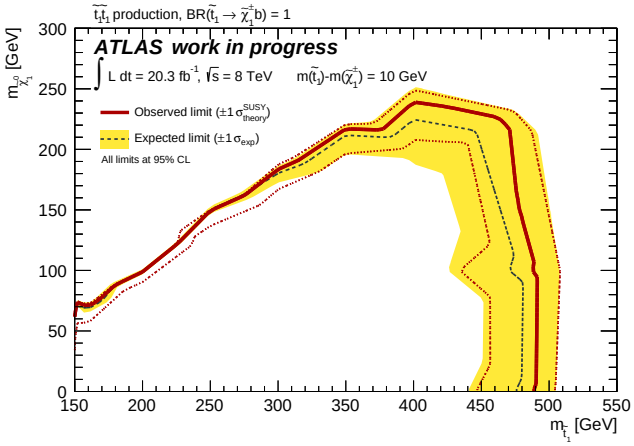

Figure 5.19: Exclusion limits at 95% CL on the masses of the stop and $\tilde{\chi}_1^0$, for a fixed $m(\tilde{t}_1) - m(\tilde{\chi}_1^{\pm}) = 10$ GeV and assuming BR($\tilde{t}_1 \to b\tilde{\chi}_1^{\pm}$) = 1. The dashed line and the shaded band are the expected limit and its ± 1 σ uncertainty, respectively. The thick solid line is the observed limit for the central value of the signal cross section. The dotted lines show the effect on the observed limit when varying the signal cross section by ± 1 σ of the theoretical uncertainty.

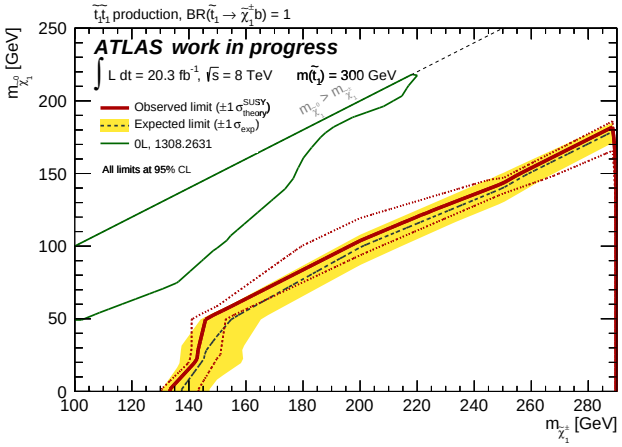

Figure 5.20: Exclusion limits at 95% CL on the masses of the chargino and neutralino, for a stop with a mass of 300 GeV and assuming BR($\tilde{t}_1 \to b\tilde{\chi}_1^{\pm}$) = 1. The dashed line and the shaded band are the expected limit and its ± 1 σ uncertainty, respectively. The thick solid line is the observed limit for the central value of the signal cross section. The dotted lines show the effect on the observed limit when varying the signal cross section by ± 1 σ of the theoretical uncertainty. The expected limit from another ATLAS SUSY search in full-hadronic final states [88] is also drawn for comparison: the two results are complementary.

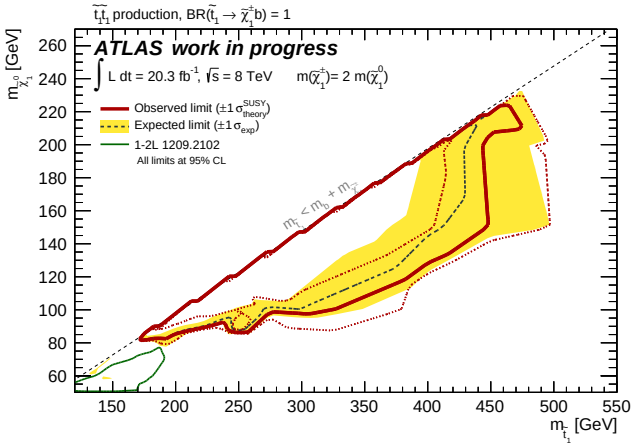

Figure 5.21: Exclusion limits at 95% CL on the masses of the stop and neutralino, for $m(\tilde{\chi}_1^{\pm}) = 2m(\tilde{\chi}_1^0)$ and assuming BR($\tilde{t}_1 \to b\tilde{\chi}_1^{\pm}$) = 1. The dashed line and the shaded band are the expected limit and its ± 1 σ uncertainty, respectively. The thick solid line is the observed limit for the central value of the signal cross section. The dotted lines show the effect on the observed limit when varying the signal cross section by ± 1 σ of the theoretical uncertainty. The expected limit from another SUSY search in the one-lepton (1L) channel [148] is also drawn for comparison: the two results are complementary.

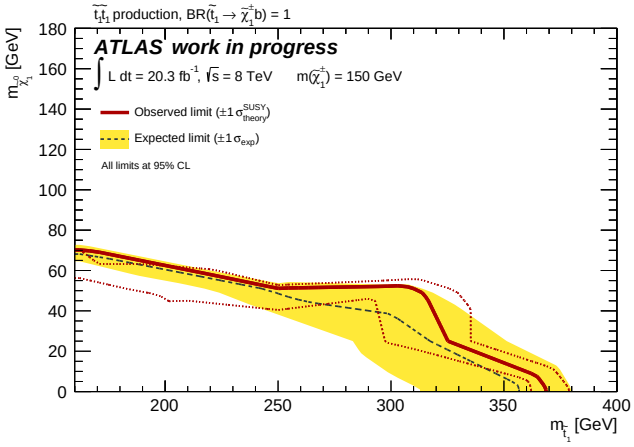

Figure 5.22: Exclusion limits at 95% CL on the masses of the stop and neutralino, for a chargino with a mass of 150 GeV and assuming BR($\tilde{t}_1 \to b\tilde{\chi}_1^{\pm}$) = 1. The dashed line and the shaded band are the expected limit and its ± 1 σ uncertainty, respectively. The thick solid line is the observed limit for the central value of the signal cross section. The dotted lines show the effect on the observed limit when varying the signal cross section by ± 1 σ of the theoretical uncertainty.

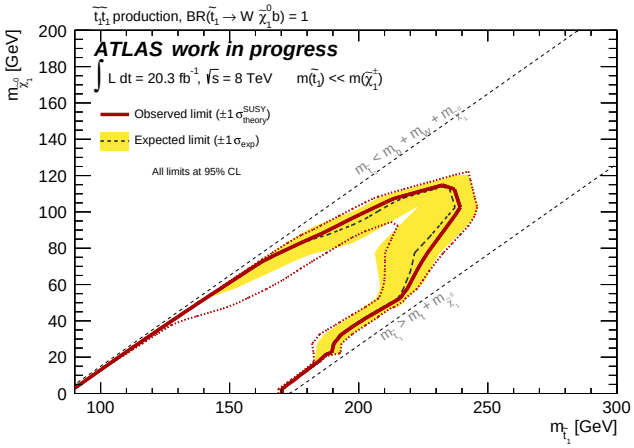

Figure 5.23: Exclusion limits at 95% CL on the masses of the stop and neutralino, assuming BR($\tilde{t}_1 \to Wb\tilde{\chi}_1^0$) = 1. The dashed line and the shaded band are the expected limit and its ± 1 σ uncertainty, respectively. The thick solid line is the observed limit for the central value of the signal cross section. The dotted lines show the effect on the observed limit when varying the signal cross section by ± 1 σ of the theoretical uncertainty.

Summary

A search for pair production of stop in final states with two leptons (e or μ) has been presented in this thesis.

The search utilizes the full $\sqrt{s} = 7$ TeV and $\sqrt{s} = 8$ TeV datasets of pp collisions recorded by the ATLAS experiment in 2011 and 2012, respectively, and is based on a cut-and-count approach which makes use of the stranverse mass of the two leptons, m_{T2}^{ll}, as a key ingredient to discriminate the SUSY signal from the main SM background sources. The two 7 TeV and 8 TeV cases have been presented separately for historical reasons.

Results obtained with the 7 TeV dataset have been interpreted in terms of a natural SUSY simplified model of pair production of stop, each decaying to a top quark and a neutralino with 100% BR: $\tilde{t}_1 \to t\tilde{\chi}_1^0$. A stop mass of 300 GeV is excluded at 95% CL for a nearly massless $\tilde{\chi}_1^0$. Results have been published on the JHEP journal [145]. At the time of publication, the search was among the first ones at the LHC seeking for a stop pair production in a two-lepton final state, and the published limits have also been, at that time, the most constraining results on the stop mass in the $\tilde{t}_1 \to t\tilde{\chi}_1^0$ decay channel.

In the 8 TeV case, the selection cuts have been revised to optimize the analysis sensitivity for other two natural SUSY simplified models: a stop pair production with each stop decaying to a $b-$quark and a chargino ($\tilde{t}_1 \to b\tilde{\chi}_1^{\pm}$), and a three-body decay of the stop to a $b-$quark, a W boson and a neutralino ($\tilde{t}_1 \to bW\tilde{\chi}_1^0$). Both decays consider a 100% BR in the final state. For the first scenario, the analysis results exclude at 95% CL stop masses between 150 GeV and 500 GeV for a nearly massless neutralino and approximately degenerate chargino and stop masses, enlarging the coverage reached by a previous search with two leptons and partial 8 TeV data, also published by the ATLAS experiment [144]. For the three-body decay scenario, stop masses up to 240 GeV are excluded in the case of $m(\tilde{\chi}_1^0) = 100$ GeV.

A preliminary version of these results has already been published as an ATLAS publication [147] and, at the time of release, it established exclusion limits on the three-body kinematic region for the first time at the LHC. The preliminary limits can be seen in Fig. 5.24, where all latest results from the searches for stop direct production in ATLAS are shown. The purple area on the right of the figure represents the preliminary limits on the three-body decay channel. They are still competitive within ATLAS, although a recent CMS search enlarged the coverage in this kinematic region up to 300 GeV for a 175 GeV neutralino [123]. On the left of the figure, the light blue area and one of the two dark blue areas represent the preliminary exclusion limits placed on the $\tilde{t}_1 \to b\tilde{\chi}_1^{\pm}$ simplified models with $m(\tilde{\chi}_1^{\pm}) = m(\tilde{t}_1) - 10$ GeV and $m(\tilde{\chi}_1^{\pm}) = 2 \times m(\tilde{\chi}_1^0)$, respectively.

The updated version of these limits, presented in this document in Section 5.6, enlarges the coverage by 5-10%, depending on the model, and is at the time of writing under approval by the ATLAS Collaboration, to be submitted to the JHEP journal.

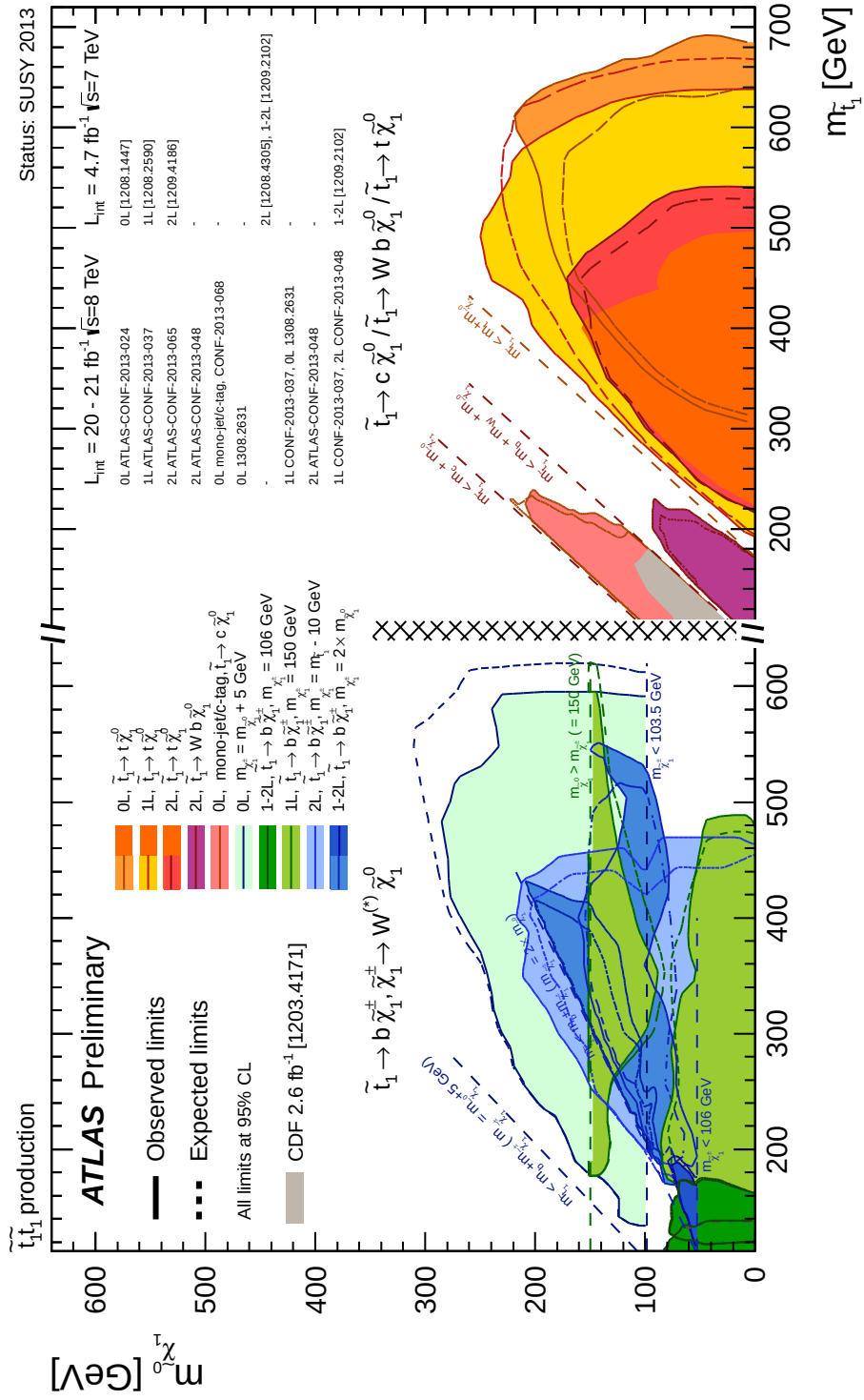

Figure 5.24: ATLAS exclusion limits at 95% CL from direct stop searches in the stop-neutralino mass plane for different decay modes and several hypotheses on the stop, chargino, neutralino masses hierarchy [92].

Bibliography

[1] L. Evans and P. Bryant, JINST **3** (2008) S08001.

[2] The ATLAS Collaboration, Phys. Lett. **B716** (2012) 1-29.

[3] The CMS Collaboration, Phys. Lett. **B716** (2012) 30-61.

[4] C. Quigg, *Gauge Theories of the Strong, Weak, and Electromagnetic Interactions*, Addison-Wesley (1983).

[5] M. Gell-Mann, Phys. Lett. **8** (1964) 214.

[6] K. Nakamura, J. Phys. **G37** (2012) 075021.

[7] S. L. Glashow, Nucl. Phys. **22** (1961) 579.

[8] S. Weinberg, Phys. Rev. Lett. **19** (1967) 1264.

[9] A. Salam, *Elementary Particle Theory*, ed. N. Svartholm, Almquist and Wiksells, Stockholm (1969).

[10] S. L. Glashow, J. Iliopoulus, and L. Maiani, Phys. Rev. **D2** (1970) 1285.

[11] P. W. Higgs, Phys. Lett. **12** (1964) 132.

[12] P. W. Higgs, Phys. Lett. **13** (1964) 508.

[13] P. W. Higgs, Phys. Rev. **145** (1966) 1156.

[14] P. A. M. Dirac, Proc. R. Soc. Lond. A 1928 **117**, doi: 10.1098/rspa.1928.0023 (1928).

[15] C. Anderson, Phys. Rev. **43** (1932) 491.

[16] J. Chadwick, Nature **129** 3252 (1932) 312.

[17] C. Anderson and S. H. Neddermeyer, Phys. Rev. **51** (1937) 884.

[18] Lattes, Occhialini, and Powell, Nature **160**, 453 (1947).

[19] C. L. Cowan, F. Reines, F. B. Harrison, H. W. Kruse, and A. D. McGuire, Science **124** 3212 (1956) 103.

[20] O. Chamberlain, E. Segre, C. Wiegand, and T. Ypsilantis, Phys. Rev. **100** (1955) 947.

[21] L. M. Lederman, M. Schwartz, and J. Steinberger, Phys. Rev. Lett. **9** (1962) 36.

[22] B. Richter, Phys. Rev. Lett. **33** (1947) 1406.

[23] S. Ting, Phys. Rev. Lett. **33** (1947) 1404.

[24] The UA1 Collaboration, Phys. Lett. B **122** (1983) 103.

[25] The UA2 Collaboration, Phys. Lett. B **122** (1983) 476.

[26] The CDF Collaboration, Phys. Rev. Lett. **74** (1995) 2626.

[27] The D0 Collaboration, Phys. Rev. Lett. **74** (1995) 2632.

[28] F. J. Hasert, Nucl. Phys. **B73** (1974) 1.

[29] The ATLAS Collaboration, JOIN **3** (2008) S08003.

[30] The CMS Collaboration, JOIN **3** (2008) S08004.

[31] The ATLAS Collaboration, ATLAS-CONF-2012-170 (2012).

[32] The CMS Collaboration, CMS-PAS-HIG-12-045 (2012).

[33] `http://www.nobelprize.org/nobel_prizes/physics/laureates/2013/press.pdf`, press release from Royal Swedish Academy of Sciences (2013).

[34] E. Witten, Nucl. Phys. **B188** (1981) 513.

[35] S. Dimopoulos and H. Georgi, Nucl. Phys. **B193** (1981) 150.

[36] L. Susskind, Phys. Reports **104** (1984) 181.

[37] H. Miyazawa, Prog. Theor. Phys. **36** (1966) 1266.

[38] P. Ramond, Phys. Rev. **D3** (1971) 2415.

[39] Y. Golfand and E. Likhtman, JETP Lett. **13** (1971) 323.

[40] A. Neveu and J. Schwarz, Nucl. Phys. **B31** (1971) 86.

[41] A. Neveu and J. Schwarz, Phys. Rev. **D4** (1971) 1109.

[42] J. Gervais and B. Sakita, Nucl. Phys. **B34** (1971), 632.

[43] D. Volkov and V. Akulov, Phys. Lett. **B46** (1973) 109.

[44] J. Wess and B. Zumino, Phys. Lett. **B49** (1974) 52.

[45] J. Wess and B. Zumino, Nucl. Phys. **B70** (1974) 1239.

[46] N. Polonsky, Lect. Notes Phys. **M68** (2001) 1.

[47] G. Bertone, D. Hooper, and J. Silk, Phys. Rept. **405** (2005) 279.

[48] J. Beringer, Phys. Rev. **D86** (2012) 010001.

[49] S. Dimopoulos and D. Sutter, Nucl. Phys. **B452** (1995) 496.

[50] J. Kneur and G. Moultaka, Phys. Rev. **D59** (1999) 015005.

[51] S. Choi, Eur. Phys. J. **C14** (2000) 535.

[52] R. Horn and C. Johnson, *Matrix Analysis*, Cambridge University Press, Cambridge, UK (1985).

[53] S. Choi, Nucl. Phys. **B778** (2007) 85.

[54] H. Dreiner, H. Haber, and S. Martin, Phys. Reports **494** (2010) 1.

[55] J. Ellis and S. Rudaz, Phys. Lett. **128B** (1983) 248.

[56] F. Browning, D. Chang, and W. Keung, Phys. Rev. **D64** (2001) 015010.

[57] A. Bartl, Phys. Lett. **B573** (2003) 153.

[58] A. Bartl, Phys. Rev. **D70** (2004) 035003.

[59] H. Nilles, Phys. Reports **110** (1984) 1.

[60] P. Nath, R. Arnowitt, and A. Chamseddine, *Applied N = 1 Supergravity*, World Scientific, Singapore (1984).

[61] M. Dine and A. Nelson, Phys. Rev. **D48** (1993) 1277.

[62] M. Dine, A. Nelson, and Y. Shirman, Phys. Rev. **D51** (1995) 1362.

[63] M. Dine, Phys. Rev. **D53** (1996) 2658.

[64] G. Giudice and R. Rattazzi, Phys. Reports **322** (1999) 419.

[65] R. Barbieri and G. Giudice, Nucl. Phys. **B305** (1988) 63.

[66] A. Djouadi, J. Kneur, and G. Moultaka, Comput. Phys. Commun. **176** (2005) 426.

[67] C. Berger, JHEP **0902** (2009) 023.

[68] N. Arkani-Hamed, hep-ph/0703088.

[69] J. Alwall, Phys. Rev. **D79** (2009) 015005.

[70] J. Alwall, P. Schuster, and N. Toro, Phys. Lett. **B702** (2011) 64.

[71] D. Alves, Nucl. Phys. **B305**, arXiv:1105.2838 [hep-ph].

[72] The CMS Collaboration, CMS-PAS-BPH-13-007 (2013).

[73] The LHCb Collaboration, LHCb-CONF-2013-012 (2013).

[74] The LEP2 SUSY Working Group and ALEPH and DELPHI and L3 and OPAL Collaboration, note LEPSUSYWG/01-03.1, `http://lepsusy.web.cern.ch/lepsusy`.

[75] The LEP2 SUSY Working Group and ALEPH and DELPHI and L3 and OPAL Collaboration, note LEPSUSYWG/02-04.1, `http://lepsusy.web.cern.ch/lepsusy`.

[76] T. Affolder, Phys. Rev. **D64** (2001) 032002.

[77] The CDF Collaboration, CDF public note 10137 (2010).

[78] V. M. Abazov, Phys. Rev. **D67** (2003) 012004.

[79] The D0 Collaboration, D0 note 6037-CONF (2010).

[80] The CDF Collaboration, Phys. Rev. Lett. **102** (2009) 121801.

[81] The D0 Collaboration, Phys. Lett. **B660** (2008) 449.

[82] The CDF Collaboration, CDF Note 10636 (2011).

[83] The ATLAS Collaboration, ATLAS-CONF-2013-089 (2013).

[84] The ATLAS Collaboration, ATLAS-CONF-2013-062 (2013).

[85] The ATLAS Collaboration, ATLAS-CONF-2013-024 (2013).

[86] The ATLAS Collaboration, ATLAS-CONF-2013-037 (2013).

[87] The ATLAS Collaboration, ATLAS-CONF-2013-065 (2013).

[88] The ATLAS Collaboration, JHEP **10** (2013) 189.

[89] The ATLAS Collaboration, ATLAS-CONF-2013-048 (2013).

[90] The ATLAS Collaboration, ATLAS-CONF-2013-035 (2013).

[91] The CMS Collaboration, `https://twiki.cern.ch/twiki/bin/view/CMSPublic/PhysicsResultsSUS`.

[92] The ATLAS Collaboration, `https://twiki.cern.ch/twiki/bin/view/AtlasPublic/SupersymmetryPublicResults`.

[93] The LEP Collaboration, CERN-EP-2001-21 (2001), arXiv:hep-ex/0103048.

[94] CERN, `http://lpc.web.cern.ch/lpc/lumiplots_2011.htm`.

[95] The LHCb Collaboration, JOIN **3** (2008) S08005.

[96] The ALICE Collaboration, JOIN **3** (2008) S08002.

[97] CERN, `http://press.web.cern.ch/press-releases/2012/12/first-lhc-protons-run-ends-new-milestone`.

[98] CERN, `http://lpc.web.cern.ch/lpc/lumiplots_2012.htm`.

[99] The ATLAS Collaboration, arXiv:0901.0512v4 [hep-ex].

[100] The ATLAS Collaboration, arXiv:1004.5293v2 [physics.ins-det] (2010).

[101] The ATLAS Collaboration, arXiv:0912.2642v4 [physics.ins-det] (2009).

[102] The ATLAS Collaboration, arXiv:1007.5423v2 [physics.ins-det] (2010).

[103] The ATLAS Collaboration, arXiv:1006.4384v2 [physics.ins-det] (2010).

[104] The ATLAS Collaboration, ATLAS-CONF-2010-060 (2010).

[105] A. Sbrizzi, ATL-LUMPROC-2010-004 (2010).

[106] P. Ruzicka, ATL-LUM-PROC-2010-001 (2010).

[107] The ATLAS Collaboration, CERN-OPEN-2008-020 (2008) 550.

[108] W. Lampl, ATL-LARG-PUB-2008-002 (2008).

[109] The ATLAS Collaboration, ATLAS-CONF-2013-088 (2013).

[110] S. Hassani, L. Chevalier, E. Lancon, J. F. Laporte, R. Nicolaidou, and A. Ouraou, Nucl. Instrum. Meth. **A** (2007) 572.

[111] T. Lagouri, IEEE Trans. Nucl. Sci. **51** (2004) 3030.

[112] M. Cacciari, G. P. Salam, and G. Soyez, JHEP **0804** (2008) 063.

[113] The ATLAS Collaboration, ATLAS-CONF-2012-043 (2012).

[114] The ATLAS Collaboration, ATLAS-CONF-2011-102 (2011).

[115] The ATLAS Collaboration, Eur. Phys. J **C72** (2012) 1844.

[116] The ATLAS Collaboration, arXiv:1101.2185 [hep-ex] (2011).

[117] The LEP2 SUSY Working Group and ALEPH and DELPHI and L3 and OPAL Collaboration, note LEPSUSYWG/04-02.1, `http://lepsusy.web.cern.ch/lepsusy`.

[118] The CDF Collaboration, Phys. Rev. Lett. **104** (2010) 251801.

[119] The D0 Collaboration, Phys. Lett. **B674** (2009) 4.

[120] The CDF Collaboration, arXiv:1203.4171 [hep-ex] (2012).

[121] The D0 Collaboration, Phys. Lett. **B665** (2008) 1.

[122] The ATLAS Collaboration, ATLAS-CONF-2013-068 (2013).

[123] The CMS Collaboration, PAS-SUS-13-004 (2013).

[124] C. G. Lester and D. J. Summers, Phys. Lett. **B463** (1999) 99.

[125] A. Barr, C. Lester, and P. Stephens, J. Phys. **G29** (2003) 2343.

[126] S. Frixione and B. R. Webber, JHEP **0206** (2002) 029.

[127] S. Frixione, E. Laenen, P. Motylinski, and B. R. Webber, JHEP **03** (2006) 092.

[128] G. Corcella, JHEP **0101** (2001) 010.

[129] J. Butterworth, J. R. Forshaw, and M. Seymour, Z.Phys. **C72** (1996) 637646.

[130] H. Lai, Phys. Rev. **D82** (2010) 074024.

[131] J. Pumplin, JHEP **0207** (2002) 012.

[132] S. Frixione, P. Nason, and C. Oleari, JHEP **0711** (2007) 070.

[133] T. Sjostrand, S. Mrenna, and P. Z. Skands, JHEP **05** (2006) 026.

[134] M. L. Mangano, M. Moretti, F. Piccinini, R. Pittau, and A. D. Polosa, JHEP **0307** (2003) 001.

[135] B. P. Kersevan and E. Richter-Was, arXiv:hep-ph/0405247.

[136] P. M. Nadolsky, Phys. Rev. 728 **D78** (2008) 013004.

[137] T. Gleisberg, JHEP **0902** (2009) 007.

[138] J. Alwall, M. Herquet, F. Maltoni, O. Mattelaer, , and T. Stelzer, JHEP **1106** (2011) 128.

[139] T. Sjostrand, S. Mrenna, and P. Z. Skands, Comput.Phys.Commun. **178** (2008) 852.

[140] The ATLAS Collaboration, Eur. Phys. J. **C70** (2010) 696/823.

[141] The GEANT4 Collaboration, S. Agostinelli, Nucl. Instrum. 698 Meth. **A506** (2003) 250303.

[142] The ATLAS Collaboration, ATL-PHYS-PUB-2010-013 (2010).

[143] M. Bahr, Eur. Phys. J. **C58** (2008) 639.

[144] The ATLAS Collaboration, ATLAS-CONF-2012-167 (2012).

[145] The ATLAS Collaboration, JHEP **1211** (2012) 094.

[146] A. L. Read, J. Phys. **G28** (2002) 2693.

[147] The ATLAS Collaboration, ATLAS-CONF-2013-048 (2013).

[148] The ATLAS Collaboration, arXiv:1209.2102 [hep-ex] (2013).